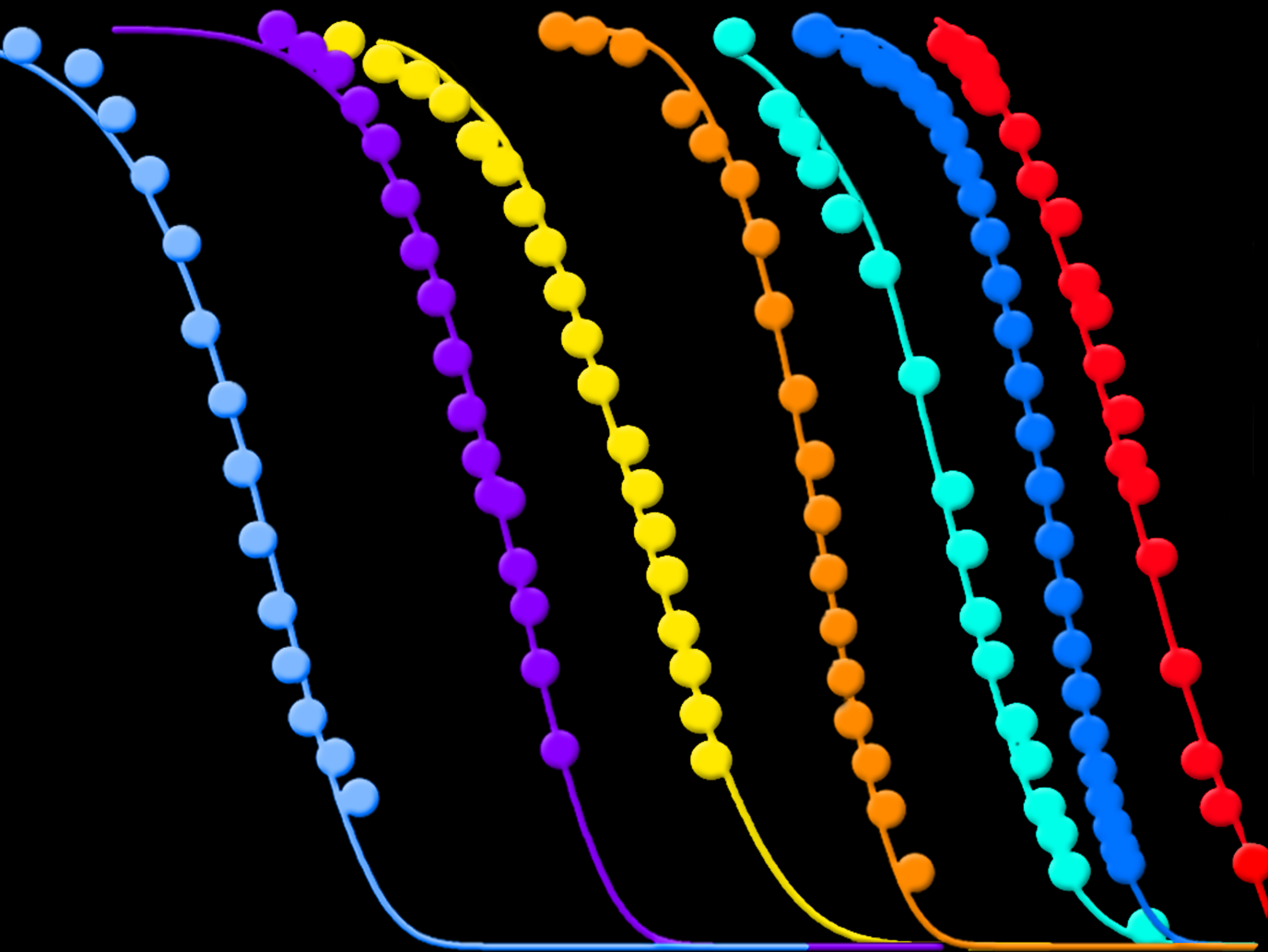# Perovskite Solar Cells
# from a Sustainability Perspective

Salvatore Valastro

# UNIVERSITÀ degli STUDI di CATANIA

**Ph.D. in Materials Science and Nanotechnology XXXV Cycle**

*Ph.D. Thesis*

# Perovskite Solar Cells
# from a Sustainability Perspective

Salvatore Valastro

UNICT Tutor:

Prof. Antonio Terrasi

CNR-IMM Tutor:

Dott.ssa Alessandra Alberti

UNIVERSITÀ
degli STUDI
di CATANIA

IMM Istituto per la
Microelettronica e
Microsistemi
Consiglio Nazionale delle Ricerche

# Contents

## Introduction

## Chapter 1: Stability of low-temperature Eu-doped CsPbI$_3$

## Chapter 2: Stability of HTL-free carbon-based PSCs

# Chapter 3: Eu-doped CsPbI$_3$ triple-mesoscopic carbon-PSCs

# Chapter 4: Sequestration of leaked Pb from PSCs by TiO$_2$ sponges

# Chapter 5: Perovskite deposition methods for clean and up-scalable manufacturing

# List of Abbreviations

| | |
|---|---|
| AFM | Atomic Force Microscopy |
| AM 1.5 | Air Mass 1.5 |
| AVA | Aminovaleric Acid |
| AVT | Average Visible Transmittance |
| BAPV | Building Applied Photovoltaics |
| BCP | Bathocuproine |
| BF | Bright Field |
| BIPV | Building Integrated Photovoltaics |
| $C_{60}$ | Fullerene |
| CAE | Constant Analyser Energy |
| CAFM | Conductive Atomic Force Microscopy |
| CAGR | Compounded Average Growth Rate |
| Capex | Capital Expenditure |
| CB | Conduction Band |
| CE | Counter Electrode |
| c-ETL | compact-ETL |
| CP | Critical Point |
| CPPB | Critical Points Parabolic Band |
| CTL | Charges Transporting Layer |
| DB | Doctor-Blading |
| DBv | Doctor-Blading vacuum curing |
| DC | Direct Current |
| DF | Dark Field |
| DFT | Density Functional Theory |
| DMDP | P, P'-di(2-ethylhexyl) methanediphosphonic acid |
| DMF | Dimethylformamide |
| DMSO | Dimethyl sulfoxide |
| DSSC | Dye Sensitized Solar Cell |
| EDX | Energy Dispersive X-ray fluorescence |
| ETL | Electrons Transporting Layer |
| ETM | Electrons Transporting Material |
| EU | European Union |
| EVA | Ethylene-Vinyl acetate |
| FA | Formamidinium |
| FF | Fill Factor |
| FS | Forward Scan |
| FTO | Fluorine-doped Tin Oxide |
| HAADF | High-Angle Annular Dark Field |

| | |
|---|---|
| HDI | Human Development Index |
| HEC | Hydroxyethyl Cellulose |
| HMB | Hexamethonium Bromide |
| HP | Hot-Pressing |
| HT | High Temperature |
| HTL | Holes Transporting Layer |
| HTM | Holes Transporting Material |
| HV | High Vacuum |
| HV-PVD | High Vacuum-Physical Vapor Deposition |
| ICP/MS | Inductively Coupled Plasma Mass Spectrometry |
| IEA | International Energy Agency |
| IEC | International Electrotechnical Commission |
| IoT | Internet of Things |
| IPA | 2-propanol |
| ISOS | International Summit on Organic PV Stability |
| ITO | Indium Tin Oxide |
| JMAK | Johnson-Mehl-Avrami-Kolmogorov |
| $J_{SC}$ | Short-Circuit current density |
| LT | Low Temperature |
| LV | Low Vacuum |
| LV-PSE | Low Vacuum-Proximity Space Effusion |
| MA | Methylammonium |
| mC-PSCs | Mesoscopic Carbon Perovskite Solar Cells |
| mp-ETL | mesoporous-ETL |
| MPP | Maximum Power Point |
| MPPT | Maximum Power Point Tracking |
| PCBM | Phenyl-C61-butyric acid methyl ester |
| PCE | Power Conversion Efficiency |
| PEAI | Phenethylammonium iodide |
| PEDOT:PSS | Poly(3,4-ethylenedioxythiophene) polystyrene sulfonate |
| PEN | Polyethylene Naphthalate |
| PET | Polyethylene Terephthalate |
| PN4N | Amine-containing polymer |
| PR-VA | Pot-Roast Vapour Annealing |
| PSC | Perovskite Solar Cell |
| PSK | Perovskite |
| PTAA | Poly[bis(4-phenyl)(2,4,6-trimethylphenyl)amine |
| PV | Photovoltaic |
| PVD | Physical Vapor Deposition |
| R&D | Research and Development |
| R2R | Roll-to-Roll |

| | |
|---|---|
| RH | Relative Humidity |
| RS | Reverse Scan |
| RT | Room Temperature |
| SE | Spectroscopic Ellipsometry |
| SG&A | Selling, and General and Administrative expenses |
| spiro-MeOTAD | 2,2',7,7'-Tetrakis[N,N-di(4-methoxyphenyl)amino]-9,9'-spirobifluorene |
| SQ limit | Shockley-Queisser limit |
| SQE | Sequestration Efficiency |
| SLG | Soda Lime Glass |
| SRH | Shockley Read Hall |
| SSC | Silicon Solar Cell |
| STEM | Scanning Transmission Electron Microscopy |
| ST-PSC | Semi-Transparent Perovskite Solar Cell |
| TBP | 4-tert-Butylpyridine |
| TCO | Transparent Conductive Oxide |
| TEM | Transmission Electron Microscopy |
| TOL | Toluene anhydrous |
| US | United States |
| UV | Ultraviolet |
| VB | Valence Band |
| $V_{OC}$ | Open-Circuit Voltage |
| XPS | X-ray Photoelectron Spectroscopy |
| XRD | X-Ray Diffraction |
| XRR | X-Ray Reflectivity |

# Introduction

## I.1.    The world's energy challenge

We need energy for all. We need energy to eat, to move, to study, to work, to light up our cities, to do every little thing including to supply the device we are using to read this PhD thesis (if you are reading the electronic copy).

The necessity of energy is proportional to the economic growth, well-being and prosperity in the world. As shown in figure 1, the energy consumption per capita is strictly related to the human development index (HDI)[1] which takes into account life expectancy, education and standard of living[2]. In addition, the increasing of world population from 7.8 billion of 2020 to the predicted 9.6 billion of 2050[3] further amplifies the need of more energy.
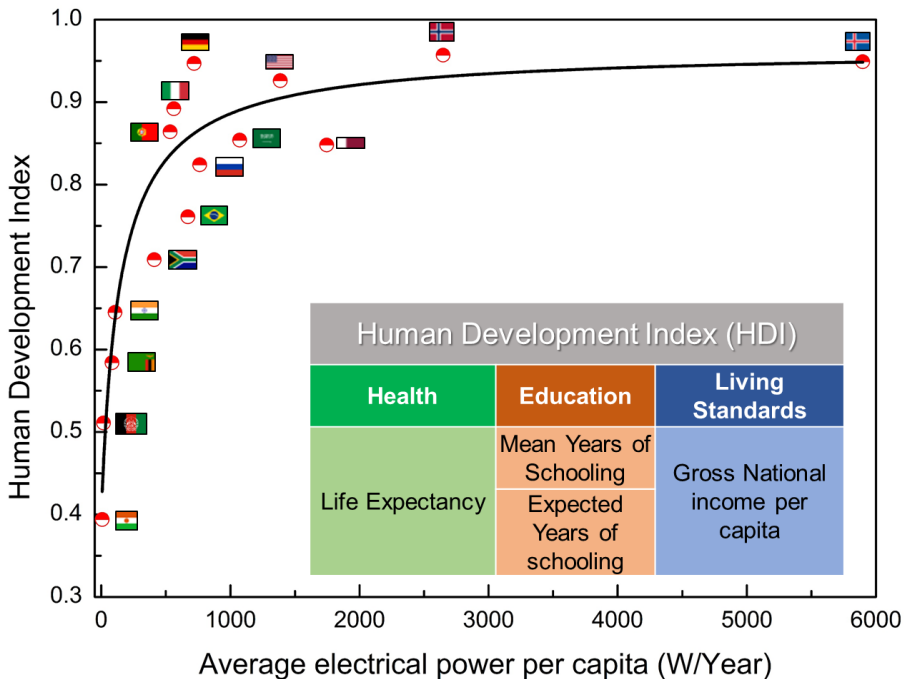


*Figure 1 Human Development Index (HDI) vs Energy consumption per capita (W/Year)[4](2021)*

In the last few years, civil society and governments have raised the awareness on the urgent change of direction towards a more sustainable world to tackle the climate change concerns, thus supporting, among the others, the actions to reduce the greenhouse gas emissions[5]. Dedicated campaigns, climate conferences, spots on TV and social networks are ongoing as initiatives to sensitize people on the necessity of

reducing our "carbon footprint" (e.g. Figure 2 E.ON footprint in Termoli beach, Italy[6]).



*Figure 2 E.ON carbon footprint in Termoli (Italy) beach (taken from [7])*

Today, energy production is responsible for more than 75% of the EU's greenhouse gas emissions. Nonetheless, it is encouraging to see from the data reported in figure 3 that the average greenhouse gas emission intensity (tons of $CO_2$/GWh) from solar photovoltaic (PV), which accounts for direct (fuel or coal burning on site) and indirect (operation and construction process) emissions, is ~100 times lower than from coal and ~50 times than from natural gas. Greenhouse gas emissions of solar PV are mostly indirect, mainly deriving from the process of construction of PV panels[8].

Special efforts are indeed largely justified to replacing coal and gas with more sustainable and innovative energy sources, as with PV. Huge funding on several research projects about renewable energy sources have indeed been made by institutions like EU in the last years. From January 2020, a total of ~100 projects on PV technologies have been launched by the EU fundings[9].
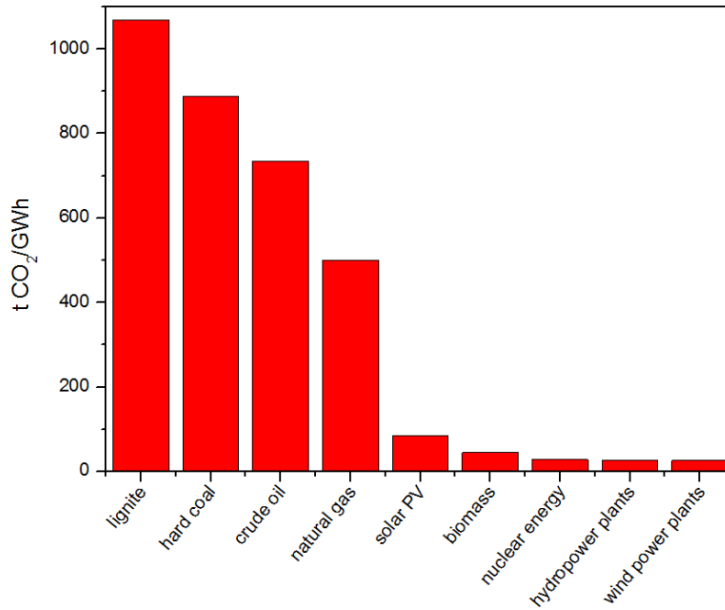
*Figure 3 Average greenhouse gas emission intensity by energy source [tons $CO_2/GWh$][10]. It considers the direct (fuel or coal burning on site) and indirect (operation and construction process) $CO_2$ emissions.*

In 2021, according to Ember's third annual Global Electricity Review[11] and the Global energy review by IEA (International Energy Agency)[12], the alternative energy sources (Wind, Solar, Hydro and Nuclear) generated 38% of the world's electricity, more than coal (36%), as shown in figure 4. In this scenario, the PV production is at around 4% of world's electricity. Europe follows a similar trend: renewables and fossil fuels accounted for a close percentage of energy production (37%), with the PV settled at 6% of electricity production[11]. To reach the European Union (EU) official objective to be climate-neutral (an economy with net-zero greenhouse gas emission) by 2050, consolidated and new sustainable technologies should synergically collaborate on different sides to accelerate the pathway to the decarbonized age.
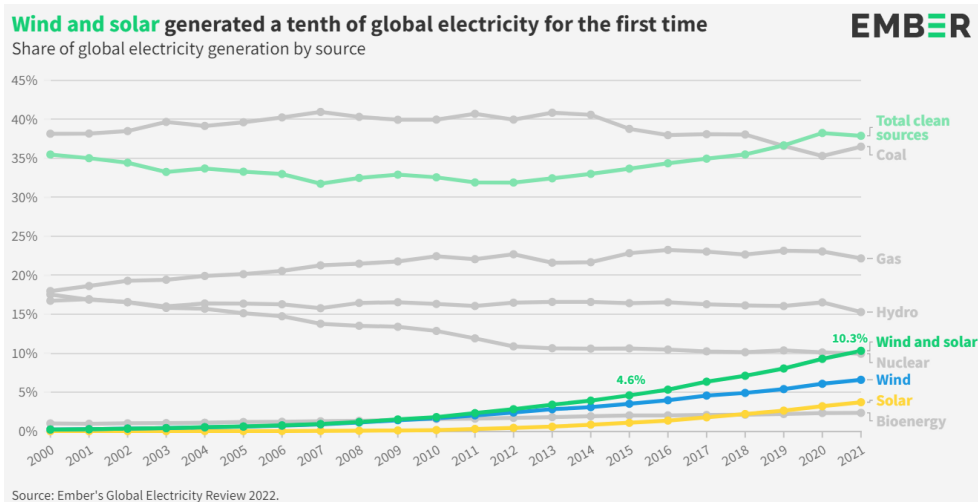
*Figure 4 Global electricity generation by source according by Ember's third annual Global Electricity Review (taken from ref. [11])*

In addition to all those environmental-societal-economic arguments, the geo-political events occurred in 2022 at the borders of Europe highlighted the importance of boosting the energetic independence from fossil fuels.[13] Among the possible choices, boosting the PV energy production is ideal to preserve ecosystem and environmental matrices (Soil, water and air). Until now, the consolidated commercial PV technologies based on Silicon (Si) have egregiously contributed to the clean energy share. But, in order to satisfy the decarbonization program of EU, a step beyond must be made in the next years to increase solar energy production. This objective can be simultaneously tackled from two different perspective: 1) increasing the photoconversion efficiency of the commercial solar technologies, 2) covering more surfaces with photovoltaic devices. The first solution is narrowed by a thermodynamic limit, the so-called Shockley-Queisser Limit (SQ limit)[14], which allows ~30% of the sunlight incident power to be converted into electricity due to the unavoidable thermal energy dissipation inside the device. The bottleneck of the second objective, that aims at increasing the overall areas covered by solar devices, resides in the rigid, heavy and opaque character of the commercial technology that limit application to rooftops and large photovoltaics plants.

The two abovementioned objectives could be simultaneously targeted by the commercialization of Perovskite Solar Cells (PSC) and panels. PSC, initiated in 2009 by Prof. Miyasaka at the Toin University of Yokohama (Japan)[15], aims not to substituting but complementing the commercial Si-based solar devices. PSCs are suitable for a wide range of different applications and profit from photoconversion efficiencies comparable to those of Si-solar cells (~26%[16]).

As a step beyond silicon, the easiness and versatile methods for photoactive perovskite production allow depositing the material on different substrates (rigid or flexible) at low-costs. Moreover, the unique and accessible characteristics of semi-transparency and bandgap tunability, by regulating material composition and thickness, make perovskites suitable for smart cities once applied on buildings (Building Integrated PV=BIPV or Building Applied PV =BAPV) and for the growing Agrivoltaics field. The lightweight of the materials allows the additional use in small-medium sized applications like portable, wearable and Internet of things (IoT) for self-powered devices, as represented in figure 5. Indoor efficiency for PSC is conveniently high (efficiency record of ~ 40%[17]) for the further benefit of IoT applications.



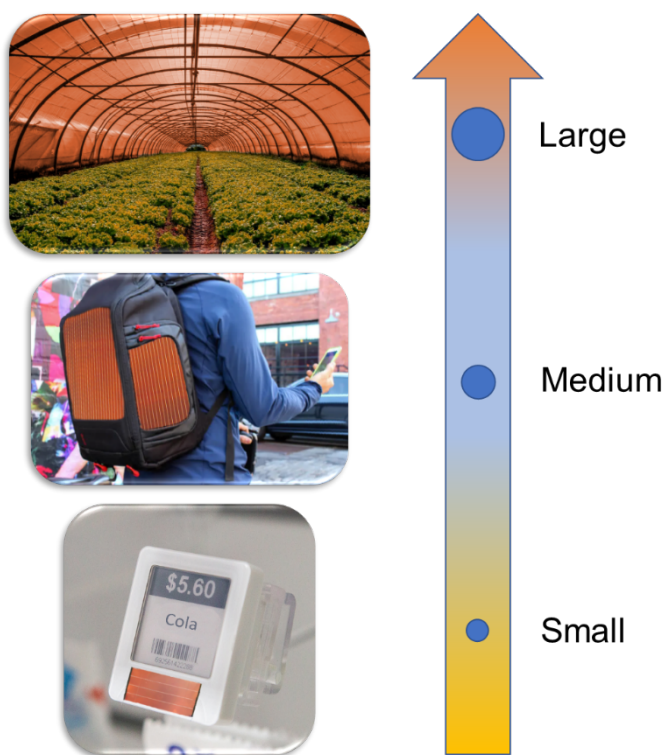*Figure 5 Small, medium and large-scale application of perovskite technologies*

In addition, it has been demonstrated that perovskite and silicon can efficiently work together since they are complementary in absorbing the solar spectrum[18,19], and this in-tandem synergy has pushed the SQ limit to ~45%[20]

For all the discussed mainstays, PSCs are near to settle a revolutionary future for the decarbonised era.

## I.2.    Working mechanism of a Perovskite Solar Cell (PSC)

The working mechanism of a PSC can be synthetically schematised as it follows: the active layer (the perovskite) absorbs photons coming from the Sun, thus generating negative (electron) and positive (hole) charged carriers which travel and are finally collected through an electric field at the anode and cathode side, respectively. The bandgap $E_g$, that is the energy jump between the Valence Band (VB) and the Conduction Band (CB) of the absorbing perovskite layer, depends on the specific perovskite composition and it is usually in the range 1.3-2.5 eV. Photons with energy less than $E_g$ are transmitted through the layer whilst photons with energy higher than $E_g$ are absorbed, eventually dissipating the extra-energy ($E_{photon}$ -$E_g$) as heat[21], and this is mostly why an efficiency limit for a solar cell exists (SQ limit). Perovskite materials for PV have a direct bandgap, whilst Silicon has an indirect bandgap of 1.12 eV, and this allows an enhancement of the absorption probability in perovskites. Consequently, photoactive perovskites exhibit a high absorption coefficient in the visible range and above, that consequently reduces the penetration depth of photons and enables the use of thin layers (a few hundreds of nanometers) in solar devices.

The generated electrical current is indeed proportional to the electrons promoted from the VB to the CB, with holes correspondingly left in the VB. The Wannier–Mott electron-hole pair (excitons) generated after photon absorption is represented in Figure 6a. Experimentally, reliable values of the exciton binding energy in photoactive perovskites spread in the range of 10-15 meV, with indeed a consensus that electrons and holes, once formed, are free to move in the crystal already at room temperature to be separately collected at the two heterojunction sides of a PSC.

Perovskites are ionic crystals. It has been well described[22] that at low temperatures the photoactive perovskites behave similarly to standard semiconductor crystals, whilst increasing temperatures causes an increase of the dielectric screening that lowers the exciton binding energy. As a drawback, the formation of large polarons due to the large electron-phonon (El-Ph) coupling occurs and partially accounts for the relatively low mobility of carriers in perovskites (20-100 ($cm^2$/Vs))[23]. At the same time, the El-Ph coupling explains how increasing the dynamic disorder (e.g. by increasing temperature) beneficially quenches photoluminescence and extends the charge recombination lifetime or equivalently increases the mean free path (~1-150 μm in films[24] vs. bulk materials[25]) of the carriers (figure 6b)[26].
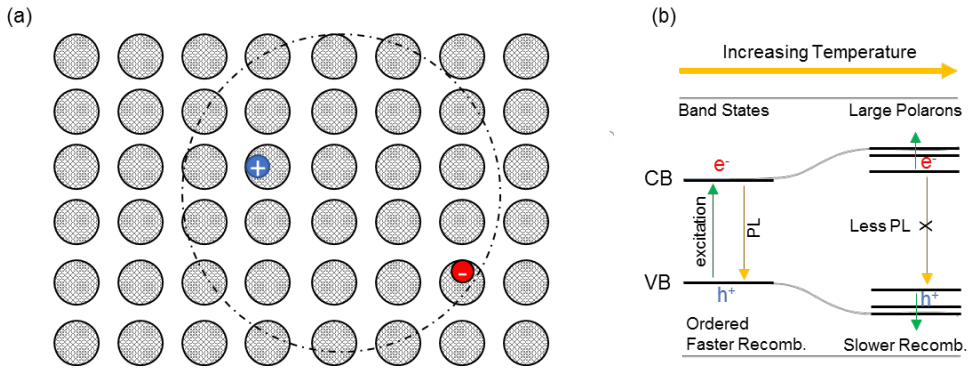
*Figure 6 a) representation of a Wannier -Mott exciton. b) Band-edge states are the lowest energy states occupied by carriers in halide perovskites at low temperature. Dynamic disorder at elevated temperatures localizes charge carriers, leading to large-polaron formation. This enhances electron-phonon coupling, that inhibits charge recombination and indeed helps quenching the photoluminescence.*

Features related to the ionic character of the perovskite lattice are the formation of phonon modes at relatively low-energy (outside the usual harmonic approximation) and the low elastic constants, making photoactive perovskites, diversely from silicon, quasi-liquid materials with a dynamic lattice disorder[27,28,29]. This property bears two advantages: the self-healing capability (in the bulk and, under certain conditions, at the surface/interfaces); a high defect tolerance.

Perovskite Solar Cells are usually treated as p-i-n or n-i-p junctions, wherein the perovskite layer is assumed to be intrinsic. The p-type and n-type materials at the boundaries of the perovskite layer are designed to extract/transport holes and electrons, respectively. They are commonly called holes transporting materials or layers (HTM or HTL) and electrons transporting materials or layers (ETM or ETL). The materials used in the PSCs architecture will be described in the next sections. In a PSC at V=0 in dark conditions, no current is generated ($J_D$=0) since the Fermi Level is uniform across the device architecture. Under illumination, a photocurrent is measured ($J_{ph}$). This current is made of photo-generated electrons (holes) injected into the CB (VB) of the ETL (HTL) by the electric field through the space charge region of the heterojunction (inset of Figure 7). The photogenerated current density measured at V=0 is called short-circuit current density ($J_{SC}$). It is proportional to the density of absorbed photons; it depends on the charge recombination probability and on the selectivity of the contacts. Typical values for $J_{sc}$ in PSCs are in the range 15-25 mA/cm$^2$.

At a specific applied positive voltage, $J_D$ starts flowing and progressively increasing in the opposite direction of $J_{ph}$, until the value of $J_D$ is equal to $J_{ph}$. Consequently, the total current flowing in the solar cell is equal to zero ($J_D$=-$J_{ph}$

→$J_{tot}$=0) at a value of the voltage that is called open-circuit voltage ($V_{oc}$). It is proportional to the $E_g$ value, and thus $V_{oc}$ in PSCs is >1 V (in silicon solar cells (SSCs) $V_{OC}$ is ~0.7 V). Typical J-V curves of a PSC in dark and under illumination are represented in figure 7.
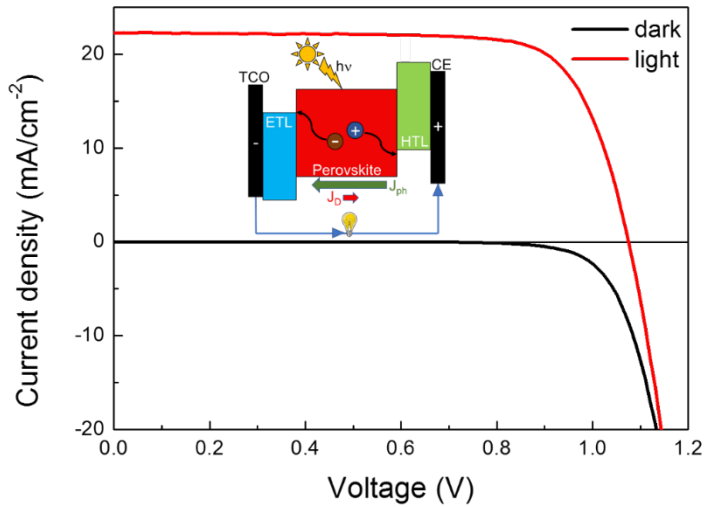


*Figure 7 Typical J-V curve and working mechanism of a PSC in dark and under illumination.*

## I.3. Crystallography and properties of photoactive perovskites

Perovskites indicates a class of material having formula $ABX_3$, where $A^+$ and $B^{2+}$ are monovalent and bivalent cations, respectively, whereas $X^-$ is a monovalent anion. B and X atoms are settled in a cubic array of corner sharing $[BX_6]^{4-}$ octahedra while A cations are located inside the empty cavities that are formed between adjacent octahedra (Figure 8). The perovskite crystal is quasi-soft (often defined quasi-liquid) compared to other materials used for PV such as Silicon in which, instead, the atoms are tightly linked by covalent bonding. Differently, the perovskite lattice has an ionic character, and the weak B-X bond makes easy phase transitions, doping and lattice engineering at low temperatures. In the perovskite lattice, the B cation and the X anion are inorganic elements like Pb or Sn (for B site) and I or Br (for X site). In hybrid perovskites, the A cation is an organic compound like Methylammonium ($MA^+$) or Formamidinium ($FA^+$) that form $MAPbI_3$ and $FAPbI_3$[30,31] perovskites, respectively. In all-inorganic perovskites, the A cation is instead an inorganic element like $Cs^+$ ($CsPbI_3$). More than one cation or anion can be simultaneously used in the same perovskite composition forming the so-called mixed perovskites (multi-cation, multi-anion) like $FA_{0.95}MA_{0.05}PbBr_{0.15}I_{2.85}$[32].
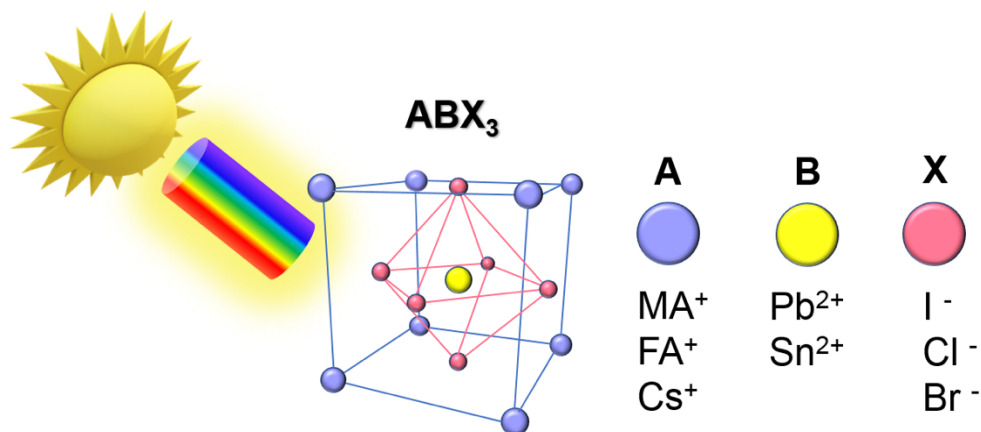


*Figure 8 Perovskite 3D crystal structure. B and X atoms are settled in a cubic array of corner sharing $[BX_6]^{4-}$ octahedra while A cations are located inside the empty cavities that are formed between adjacent octahedra*

Notwithstanding the idealized cubic $ABX_3$ structure, perovskite systems often optimize atomic distances and angles through the titling of the $BX_6$ octahedra[33]. This leads to either orthorhombic or tetragonal symmetries with a lower ground state energy and a strong prevalence at reduced temperatures, where entropic effects are not substantial.

The lattice can be, to a certain extent, predicted by considering two empiric factors: the Goldschmidt tolerance factor (t) and the octahedral factor ($\mu$). The tolerance factor defines if the A cation can fit into the cuboctahedral site formed in the corner-sharing $[BX_6]^{4-}$ octahedra while the octahedral factor considers the relationship between the radius of the octahedral hole ($r_{hole}$) within the six closely packed X ions and the B cation.[34] The Goldschmidt tolerance factor[35,36] allows to evaluate the stability and the distortion of a crystal structure being defined as follows:

$$t = \frac{r_A + r_X}{\sqrt{2}(r_B + r_X)}$$

where r is the ionic radius of the A, B or X atomic species. For t=1 a cubic structure is expected, while t$\neq$1 indicates distorted lattice. It was experimentally observed that for 0.8<t<1, stable perovskite crystals can be formed at thermodynamic conditions, otherwise the perovskite structure usually collapses to other non-perovskite phases.

The octahedral factor is defined by the following formula:

$$\mu = \frac{r_B}{r_X}$$

For halide perovskites, the octahedral factor varies in the range 0.44 < $\mu$ < 0.90[37,38].

The combination of t and $\mu$ provides a good indication about the tendency of a certain compound to form a perovskitic phase at RT.

As a matter of fact, in a recent paper[39] Sun et al. investigated the quantitative relationship between perovskite stability and t-μ values. As shown in figure 9a, the decomposition energies ($\Delta H_D$) obtained from first-principles density functional theory (DFT) calculations allows to identify stable ($\Delta H_D > 0$) and unstable ($\Delta H_D < 0$) t-μ regions for the various perovskite phases.
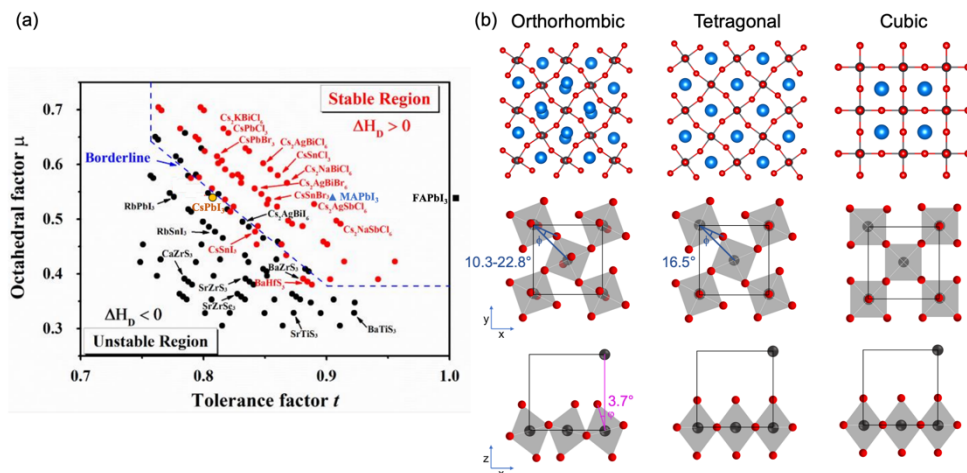


*Figure 9 (a) The (t, μ) map for 138 perovskite compounds perovskite. Red and black dot indicate a stable (ΔH_D>0) and unstable (ΔH_D<0) perovskite composition, respectively. (b) The crystal structures of the orthorhombic, tetragonal, and cubic phases of CsPbI₃. Schematic representations in the bottom panel show the angle which characterize the in-plane (ϕ) and out-of-plane (φ) octahedral tilting. The ϕ and φ values are taken from ref.[40]. The cyan, grey and red sphere represent Cs, Pb and I, respectively.*

The different perovskite composition corresponds to specific structural, optical (e.g. absorption and photoluminescence) and electrical (e.g. resistivity, photoconductivity and mobility) characteristics. At RT under certain environmental conditions, $MAPbI_3$ exists as a perovskitic tetragonal phase[41], while $CsPbI_3$ and $FAPbI_3$ have orthorhombic and cubic phase, respectively. The different perovskite structures are shown in figure 9b.

Changing composition allows tuning the bandgap values, as shown in figure 10 [42]. Among the hybrid perovskites, the bandgap value of $MAPbI_3$ is in the range 1.5-1.6 eV (1.4-1.5 eV in $FAPbI_3$) while that of $CsPbI_3$ is blue-shifted in the range 1.7-1.8 eV. In mixed perovskites (multi-cation and multi-anion such as FA-MA-Pb-Br-I) the bandgap can be tuned by varying the amount of each species resulting in distributed bandgap values in the range 1.5-2.5 eV (green dots in figure 10). Cs and Br have the effect of increasing $E_g$ with the decrease of PCE as a drawback (Figure 10).
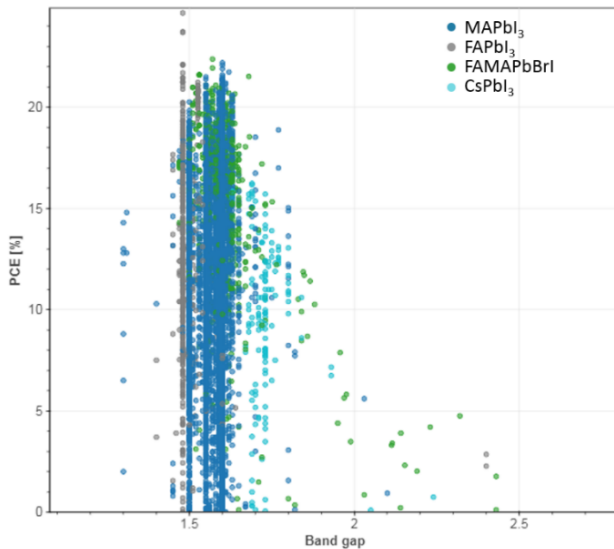
*Figure 10 Efficiency vs bandgap values for MAPbI₃, FAPbI₃, CsPbI₃ and mixed cation-anion FA-MA-Pb-Br-I perovskites. The graph has been generated from the perovskite database project in ref [43].*

Independently from composition, hereafter we summarise the unique characteristics[44] of the photoactive perovskites:

1) high absorption in the visible range[45] with respect Si PV; 2) low trap density[46] and defects tolerance, meaning that perovskites are less inclined to form intragap defects which lead to non-radiative recombination and consequently to severe loss of efficiency; 3) tuneable and direct bandgap[47,48], which allows the use of thinner films (hundreds of nm) in PSCs with respect to thicker films (tens of μm) used in Si-solar cells;4) carrier diffusion length of several tens of microns: this parameter depends on film crystallinity and morphology. [49,50]

At the same time, perovskites have issues that have been laying under the spotlight since their first applications and constantly addressed by the ongoing literature. They are listed hereinafter: 1) the formation of dynamic points defects[51,52,53], 2) the ionic migration under voltage applied[54] ; 3) the easy inlet of species from other boundary layers in the solar cell architecture[55], 4) the high sensitivity to external environmental agents (water, oxygen, or other guest atoms) and light[56,57,58,59] 5) the polymorphic transition towards non-photoactive phases[60] at temperature close to the operation range.

In addition to the abovementioned issues which are related to the material itself, a huge concern is represented by the interfaces between perovskite and the charge transporting layers which can impact on efficiency and stability of the solar cells[61,62].

## I.4.    Trending composition of photoactive perovskites

The first application of perovskites in solar cells was made by Kojima and Miyasaka[15] that applied MAPbI$_3$ in place of the dye in a dye sensitized solar cell architecture (DSSC) architecture. The Perovskite was infiltrated through a mesoporous TiO$_2$ scaffold working as ETL, achieving an efficiency of 3.8%.

In the subsequent years, following the pioneering experiment of Miyasaka and coworkers, the most investigated perovskite composition was predominantly MAPbI$_3$. Shortly after, MAPbI$_3$ was used in two key-experiments: the first one, in 2012, conducted by Kim and co-workers[63], shows the first solid state architecture using Spiro-OMeTAD (2,2',7,7'-Tetrakis[N,Ndi(4-methoxyphenyl)amino]-9,9'-spirobiuorene) as hole transporting layer achieving an efficiency of 9.7%; the second one, in 2013, conducted by Snaith[64] who fabricated the first planar perovskite solar cell without the use of mesoporous materials and with evaporated MAPbI$_3$, shows the efficiency record of 15.4%. As shown in figure 11, MAPbI$_3$ retained the record until 2016. It remains the most studied perovskite in the literature till now.

It was quite immediately clear that MAPbI$_3$ suffers from a poor structural stability over time that is still hindering long-lasting applications. The instability is mainly linked to the MA$^+$ organic cations and to the process of proton exchange between MA$^+$ and I$^-$ which is catalysed by environmental molecules like water (H$_2$O). This process leads to the formation of volatile species (CH$_3$NH$_2$ and HI) and to solid PbI$_2$ as degradation by-products[65,66].
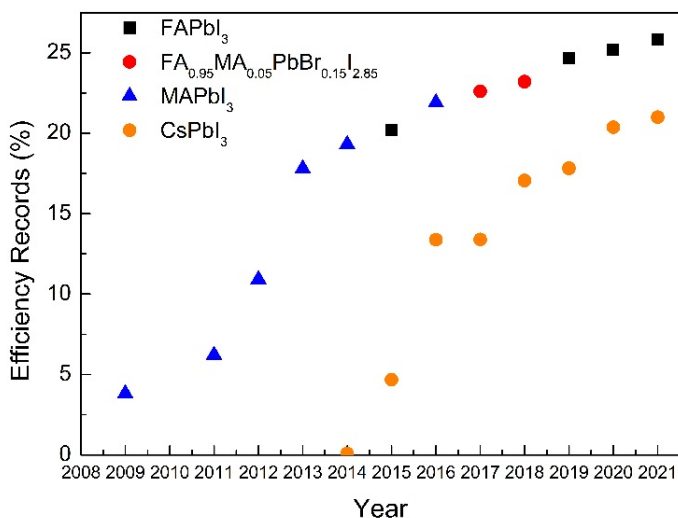


*Figure 11 Efficiency records over the year for PSCs with MAPbI$_3$, FAPbI$_3$, CsPbI$_3$ and mixed cation-anion FA-MA-Pb-Br-I*

Different strategies based on lattice engineering were proposed to improve the stability of perovskites by substituting $MA^+$ with other cations like $FA^+$ (organic), $Cs^+$ (inorganic) or by mixing many of them.

$FAPbI_3$ allows achieving a better stability with respect to $MAPbI_3$ due to the larger ionic radius of $FA^+$ with respect $MA^+$ (higher tolerance factor), different molecular symmetry of $FA^+$ with respect to $MA^+$ (and consequently different charge distribution[67]) which lead to a reduced tendency to form and release volatile species[68]. $FAPbI_3$ can exist at RT in two different phases, namely the photoactive cubic black phase ($\alpha$-phase) and the undesired (non-photoactive) yellow non-perovskite hexagonal phase ($\delta$-phase). Unfortunately, the $\alpha$-phase of $FAPbI_3$ is not stable at RT and it can easily transform at RT in the $\delta$-phase[69].

Recently, all-inorganic Cs-based perovskites (e.g. $CsPbI_3$) have received considerable attention because of their superior thermal stability[70,71,72,73] and thanks to a bandgap value ($\approx$1.73 eV) optimal for Si/PSK monolithic tandem solar cells[74,75,76]. In addition, the presence of the inorganic cation ($Cs^+$) guarantees mass preservation during operation due to the lack of volatile organic species (e.g. $MA^+$). This is strictly required for sustainable recycle/reuse of materials and devices.

The efficiency of $CsPbI_3$-based solar cells has rapidly increased over the time, from 0.09%[77] in 2014 to the actual record of 21%[78], as shown in Figure 11. As a drawback, the black photoactive phase of $CsPbI_3$ is meta-stable at RT and it spontaneously converts to the non-photoactive yellow $\delta$-phase, hindering its application.

The use of multi-cations (double or triple) and multi-anions in the same lattice has been experimented in the last years in order to attempt to increase the robustness of lattice against degradation and to improve efficiency. As a result, mixed perovskites (FA-MA-Pb-Br-I) achieved the efficiency record in 2017[79] and 2018[80]. Currently, mixed perovskites are still extensively studied. The main concern on them is the photoinduced phase separation, specifically the halogen anions segregation into bromide and iodide-rich domains, which penalises the performances of the solar cells[81,82,83,84]. Phase separation and segregation are detrimental for the long-term durability of the devices and indeed a well-motivated revival on the consolidated and most studied single-cation compounds like $MAPbI_3$, $FAPbI_3$ and $CsPbI_3$ is ongoing.

This focused effort is confirmed by the fact that all the efficiency records in the last three years have been achieved by PSCs using $FAPbI_3$ as active layer.

In brief, although ideal perovskites do not exist since each of them poses issues to be solved, every composition has specific characteristics to exploit which make it unique. Diversification is reasonably a pathway to follow for focused application in different fields.

## I.5.    Evolution of PSC architectures

PSC architectures can be listed as: n-i-p, if the layer deposited on the glass/TCO substrate is the ETL; p-i-n (or also called inverted) if the first layer is the HTL; mesoporous n-i-p integrates a mesoporous ETL (usually $TiO_2$) on the compact-ETL (c-ETL); carbon-based HTL-free, if the HTL is replaced with a carbon electrode. In all of them, perovskite is sandwiched between ETL and HTL (or carbon in HTL-free), with TCO (fluorine-doped tin oxide -FTO- and indium tin oxide -ITO-) and a top metallic electrode (e.g. Au, Ag and Al) which work as contacts. The schematic of the mentioned PSC architectures is shown in Figure 12.
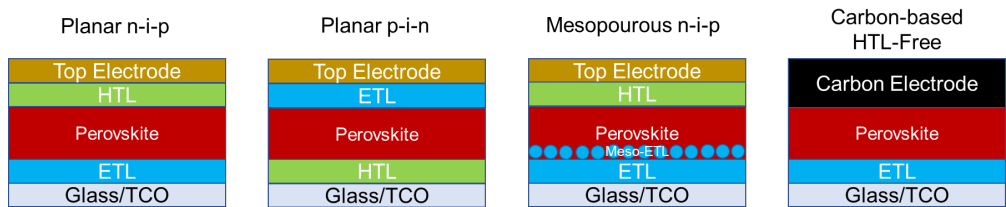


*Figure 12 n-i-p, p-i-n, mesoporous n-i-p and carbon-based HTL-free PSC architectures*.

Figure 13 represents the interplay of the different architectures to achieve efficiency records and how n-i-p devices have retained the photoconversion efficiency record since 2009. We additionally observe in Table A1, which shows the device architecture of the n-i-p devices efficiency record over the year, that common traits are the presence of a bilayer c-$TiO_2$/mp-$TiO_2$ as ETL and the use of Spiro-MeOTAD as HTL. For p-i-n devices, the architecture which achieved the best efficiency uses organic layers for both kind of transporting layers, specifically PTAA as HTL and PCBM as ETL (Table A2).
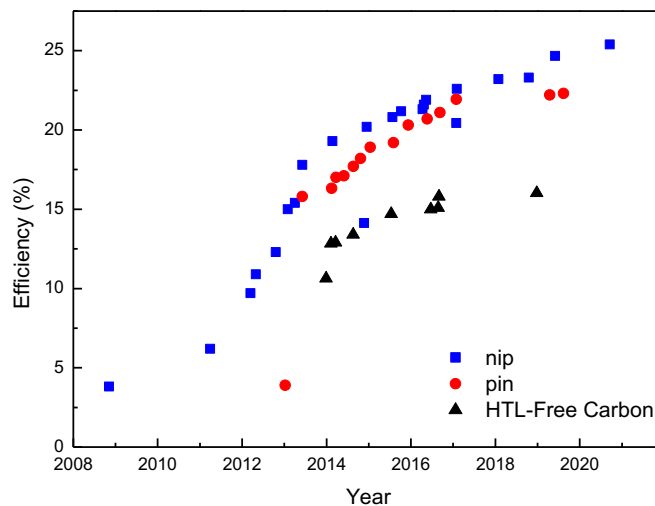


*Figure 13 Comparison of efficiency records over the year for n-i-p (mesoporous and planar), p-i-n and carbon-based HTL-free PSCs.*

Most of the organic layers used in PSC architectures are sensitive to environmental conditions such as water in atmosphere[85,86]. In addition, the thermal degradation of those layers causes the formation of voids which eases the entrance of water into perovskite layer[87,88].

A special focus has been dedicated to Spiro-OMeTAD, which is the most used HTL in PSC architectures. It is usually doped with additives like bis(trifluoromethane)sulfonimide lithium salt (LiTFSI) to improve the transport of charges[89]. But it is not fully stable[90]. Moreover, it has been observed that chemical modifications occurring at the PSK/spiro-OMeTAD interface represent main sources for the drop of PSCs performances[91], with the intrinsic degradation of the perovskite layer often playing a minor role. This highlights the pivotal impact of interfaces in the stability and electrical performances in PSCs. Spiro-OMeTAD is also expensive, ~620 €/g (the price of a commercial carbon paste is ~18 €/g[92]).

Other issues are related to the presence of the metallic layers (e.g. Au, Ag, Al) at the top electrode whose atoms are seen to diffuse into the perovskite layer during operation producing deep trap states and/or degrading the perovskite layer[93.94].

To tackle all those issues, different strategies have been reported like passivation interlayers between ETL/PSK and HTL-PSK[95], perovskite surface functionalizations[96,97]. The removal of both HTL layer and Au electrode, replacing them with more stable, hydrophobic and hugely less expensive carbon electrodes[98] (carbon-based HTL-free PSCs) is a sustainable solution to improve the stability and decrease the costs. Despite the absence of a selective HTL, carbon-based HTL-free PSCs have reached an efficiency record of 16.03% in 2019 (Figure 13 and Table A3).

Along with the stability issues, up-scaling the technology from small-area to large area devices (from lab to fab) with acceptable efficiency losses is a challenge to be faced through affordable and reproducible processes[99]. In this respect, it is noteworthy to underline that all the efficiency records values reported in the Appendix at the end of this chapter are obtained for small-active area devices (0.04-0.30 cm$^2$) and for devices fabricated through solution processing methods (e.g. spin-coating). For chemically produced PSCs, it is very hard to obtain large area cracks-free and pinholes-free perovskites. This leads to huge electrical performance losses in large-active area device (>1 cm$^2$) with respect small-area devices[100]. Figure 14 and Table 1 show how the efficiency record decreases by increasing the active area of PSC, from 25.8% for an active area of 0.1 cm$^2$, to 11.39% for 70 cm$^2$. To obtain high efficiency large-area devices, perovskite layer needs to be deposited in a uniform and reproducible manner, at high crystallographic quality. In-vacuum physical deposition methods work to that purpose.
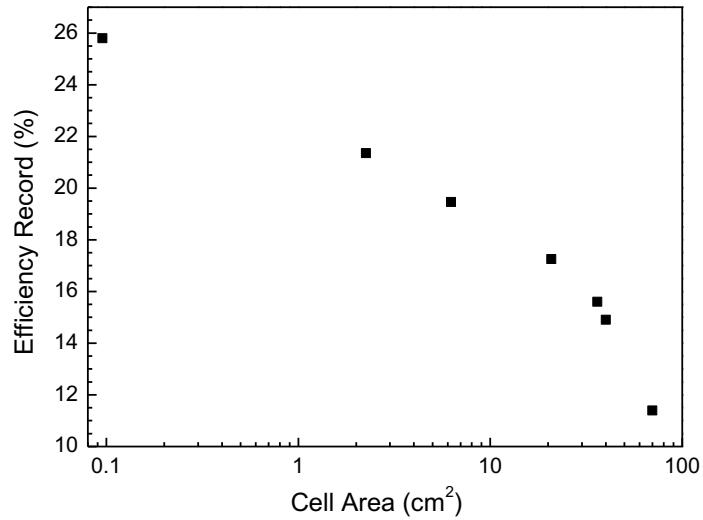
*Figure 14 Efficiency record (%) vs Cell active area (cm². The data have been extracted from Perovskite database project[43].*

| Cell active area (cm²) | Perovskite composition | PCE (%) | Ref. |
|---|---|---|---|
| 0.0955 | FAPbI$_3$ | 25.8 | [101] |
| 2.25 | Cs-MA-FA-Pb-I-Br | 21.35 | [102] |
| 6.25 | Cs-MA-FA-Pb-I-Br | 19.46 | [103] |
| 20.78 | Cs-MA-FA-Pb-I-Br | 17.25 | [104] |
| 36.1 | MAPbI$_3$ | 15.6 | [105] |
| 40 | MAPbI$_3$ | 14.9 | [106] |
| 70 | MAPbI$_3$ | 11.39 | [107] |

*Table 1 Values of Efficiency record (%) vs Cell active area (cm²)*

## I.6.    Motivations of thesis: PSCs from a sustainability perspective

Many architectures and perovskite compositions have been investigated over the years, each having specific pros and cons. The photo-conversion efficiency value is pivotal but not univocal parameter to be considered in order to evaluate a PSC architecture. From a complementary perspective, materials and architectures must fit sustainable criteria. Sustainability is a broad concept related to economic, environmental and social aspects. It moves from the awareness that resources are limited and precious, thus they must be conservatively and carefully used with a long-term vision.

Applied to PSCs production, the sustainability must account for

- durability: the performances of PSCs should be stable for a time long enough    to fulfil the market uptake rules and to avoid increasing of technological        wastes.

- circular economy: focused recycling procedures for the materials contained   in PSCs or reuse of entire devices are strictly required.

- environmental protection: solvents and related wastes for PSC production must   be   drastically   reduced[108,109,110]. Pb leakage   from damaged PSCs        demands reliable remedies.

- cost and up-scalability: the production cost of PSCs must be appetible for PV companies in terms of equipment, processes and materials. In addition,    affordable and up-scalable processes are mandatory to enable high         production   throughput   and   commercialization   of   the perovskite technology.
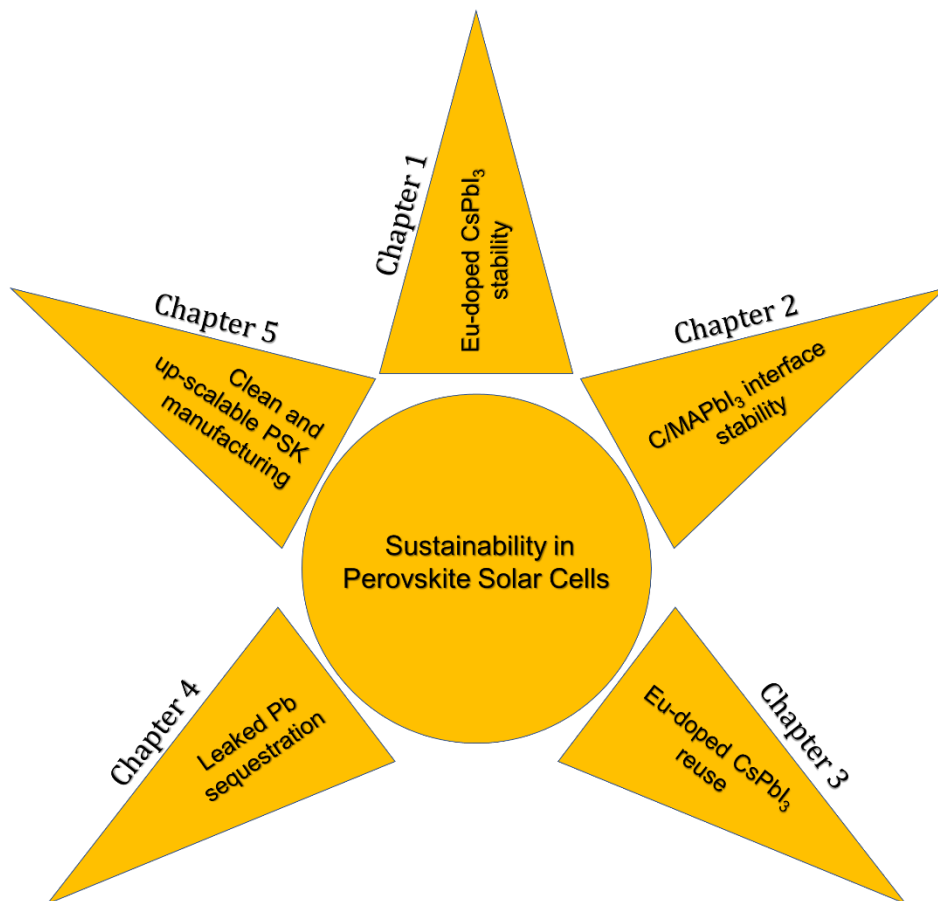
*Figure 14 Schematic of the thesis chapters.*

In the chapters of my Ph.D thesis, those aspects will be faced from possible perspectives. As sketched in Figure 14, by reading the thesis you can specifically find:

- In chapter 1, strategies to improve the stability of $CsPbI_3$ formed at low-temperature are illustrated;
- In chapter 2, two different approaches are presented to preserve the carbon/$MAPbI_3$ interface in HTL-free PSCs and, consequently, to improve performances stability;
- In chapter 3, the integration of recyclable $CsPbI_3$ perovskite in Triple-Mesoscopic Carbon-based Solar Cells is described;
- In chapter 4, a sputtered $TiO_2$ sponge for leaked Pb sequestration in Perovskite Solar Cells is investigated;
- In chapter 5, an economic analysis of up-scalable in-vacuum physical deposition methods for affordable perovskite device manufacturing is presented.

## Appendix

The appendix of this chapter contains the tables of the efficiency records over the years for n-i-p, p-i-n and carbon-based HTL-free architecture.

| Author | Publication date | Cell architecture | Perovskite composition | PCE (%) | Reference |
|---|---|---|---|---|---|
| Min et al. | 20/10/2021 | SLG \| FTO \| Cl-bonded $SnO_2$ \| Perovskite \| Spiro-MeOTAD \| Au | $FAPbI_3$ | 25.8 | [101] |
| Yoo et al. | 24/02/2021 | SLG \| FTO \| $SnO_2$ \| Perovskite \| Spiro-MeOTAD \| Au | $FAPbI_3$ | 25.4 | [111] |
| Min et al. | 08/11/2019 | SLG \| FTO \| $TiO_2$-c \| $TiO_2$-mp \| Perovskite \| Spiro-MeOTAD \| Au | $FAPbI_3$ | 24.66 | [112] |
| Jung et al. | 27/03/2019 | SLG \| FTO \| $TiO_2$-c \| $TiO_2$-mp \| Perovskite \| P3HT \| Au | $FA_{0.95}MA_{0.05}PbBr_{0.15}I_{2.85}$ \| $(HTAB)_{0.03}FA_{0.95}MA_{0.05}Pb Br_{0.15}I_{2.85}$ | 23.3 | [113] |
| Jeon et al. | 06/07/2018 | SLG \| FTO \| $TiO_2$-c \| $TiO_2$-mp \| Perovskite \| DM \| Au | $FA_{0.95}MA_{0.05}PbBr_{0.15}I_{2.85}$ | 23.2 | [114] |
| Yang et al. | 12/07/2017 | SLG \| FTO \| $TiO_2$-c \| $TiO_2$-mp \| Perovskite \| PTAA \| Au | $FA_{0.95}MA_{0.05}PbBr_{0.15}I_{2.85}$ | 22.6 | [115] |
| He et al. | 07/07/2017 | SLG \| FTO \| $TiO_2$-c \| Perovskite \| PTAA \| Ag | $FA_{0.85}MA_{0.15}PbBr_{0.45}I_{2.55}$ | 20.43 | [116] |
| Di Giacomo et al. | 19/10/2016 | SLG \| ITO \| $TiO_2$-c \| $TiO_2$-mp \| Perovskite \| Spiro-MeOTAD \| Au | $MAPbI_3$ | 21.9 | [117] |

| | | | | | |
|---|---|---|---|---|---|
| Saliba et al. | 30/09/2016 | SLG \| FTO \| $TiO_2$-c \| $TiO_2$-mp \| Perovskite \| Spiro-MeOTAD \| Au | $Cs_{0.05}FA_{0.79}MA_{0.16}PbBr_{0.51}I_{2.49}$ | 21.6 | [118] |
| Bi et al. | 19/09/2016 | SLG \| FTO \| $TiO_2$-c \| $TiO_2$-mp \| Perovskite \| Spiro-MeOTAD \| Au | $FA_{0.85}MA_{0.15}PbBr_{0.45}I_{2.55}$ | 21.3 | [119] |
| Saliba et al. | 16/03/2016 | SLG \| FTO \| $TiO_2$-c \| $TiO_2$-mp \| Perovskite \| Spiro-MeOTAD \| Au | $Cs_{0.05}FA_{0.79}MA_{0.16}PbBr_{0.51}I_{2.49}$ | 21.17 | [120] |
| Bi et al. | 02/01/2016 | SLG \| FTO \| $TiO_2$-c \| $TiO_2$-mp \| Perovskite \| Spiro-MeOTAD \| Au | $FA_{0.85}MA_{0.15}PbBr_{0.45}I_{2.45}$ | 20.8 | [121] |
| Yang et al. | 22/05/2015 | SLG \| FTO \| $TiO_2$-c \| $TiO_2$-mp \| Perovskite \| PTAA \| Au | $FAPbI_3$ | 20.2 | [122] |
| Peng et al. | 30/04/2015 | SLG \| FTO \| $TiO_2$-c \| $TiO_2$-mp \| Perovskite \| Spiro-MeOTAD \| Au | $MAPbI_3$ | 14.13 | [123] |
| Zhou et al. | 31/07/2014 | SLG \| ITO \| PEIE \| $TiO_2$-c \| Perovskite \| Spiro-MeOTAD \| Au | $MAPbI_3$ | 19.3 | [124] |
| Docampo et al. | 12/11/2013 | SLG \| FTO \| $TiO_2$-c \| Perovskite \| Spiro-MeOTAD \| Ag | $MAPbI_3$ | 17.8 | [125] |
| Liu et al. | 10/09/2013 | SLG \| FTO \| $TiO_2$-c \| Perovskite \| Spiro-MeOTAD \| Ag | $MAPbI_3$ | 15.4 | [126] |
| Burschka et al. | 09/07/2013 | SLG \| FTO \| $TiO_2$-c \| TiO2-mp \| Perovskite \| Spiro-MeOTAD \| Au | $MAPbI_3$ | 15 | [127] |

| Ball et al. | 28/03/2013 | SLG \| FTO \| TiO$_2$-c \| Al$_2$O$_3$-mp \| Perovskite \| Spiro-MeOTAD \| Ag | MAPbI$_3$ | 12.3 | [128] |
| Lee et al. | 06/10/2012 | SLG \| FTO \| TiO$_2$-c \| Al$_2$O$_3$-mp \| Perovskite \| Spiro-MeOTAD \| Au | MAPbI$_3$ | 10.9 | [129] |
| Kim et al. | 21/08/2012 | SLG \| FTO \| TiO$_2$-c \| TiO$_2$-mp \| Perovskite \| Spiro-MeOTAD \| Au | MAPbI$_3$ | 9.7 | [130] |
| Im et al. | 07/09/2011 | SLG \| FTO \| TiO$_2$-c \| TiO$_2$-mp \| Perovskite \| Ethyl acetate; I$_2$; LiI; TBP; Urea \| Pt \| FTO | MAPbI$_3$ | 6.2 | [131] |

*Table A1 n-i-p device efficiency records over the years*

| Author | Publication date | Cell architecture | Perovskite composition | PCE (%) | Reference |
|---|---|---|---|---|---|
| Degani et al. | 01/12/2021 | SLG \| ITO \| PTAA \|PEAI\| Perovskite \| PEAI\| PCBM-60 \| BCP \| Ag | Cs$_{0.1}$FA$_{0.9}$PbI$_{2.9}$Br$_{0.1}$ | 23.7 | [132] |
| Zheng et al. | 20/01/2020 | SLG \| ITO \| PTAA \| Perovskite \| C$_{60}$ \| BCP \| Cu | Cs$_{0.05}$FA$_{0.88}$MA$_{0.07}$PbBr$_{0.24}$I$_{2.76}$ | 23 | [133] |
| Lin et al. | 23/09/2019 | SLG \| ITO \| PEDOT:PSS \| Perovskite \| C$_{60}$ \| BCP \| Cu | Cs$_{0.05}$FA$_{0.09}$MA$_{0.05}$PbBr$_{0.15}$I$_{2.85}$ | 22.2 | [134] |
| He et al. | 07/07/2017 | SLG \| ITO \| PTAA \| Perovskite \| PCBM-60 \| BCP \| Ag | FA$_{0.85}$MA$_{0.15}$PbBr$_{0.45}$I$_{2.55}$ | 19.52 | [135] |

| | | | | | |
|---|---|---|---|---|---|
| Bai et al. | 16/02/2017 | SLG \| FTO \| NiO-c \| Perovskite \| PCBM-60 \| PN4N \| Ag | MAPbI$_3$ | 18.47 | [136] |
| Zhao et al. | 28/10/2016 | SLG \| ITO \| PTAA \| Perovskite \| C$_{60}$ \| BCP \| Cu | MAPbI$_3$ | 20.7 | [137] |
| Wang et al. | 17/05/2016 | PET \| ITO \| PTAA \| Perovskite \| Polystyrene \| C$_{60}$ \| BCP \| Al | MAPbI$_3$ | 20.3 | [138] |
| Shao et al. | 11/01/2016 | SLG \| ITO \| PTAA \| Perovskite \| PCBM-60 \| C$_{60}$ \| BCP \| Al | MAPbI$_3$ | 19.4 | [139] |
| Dong et al. | 23/06/2015 | SLG \| ITO \| PTAA \| Perovskite \| PCBM-60 \| C$_{60}$ \| BCP \| Al | MAPbI$_3$ | 18.9 | [140] |
| Heo et al. | 01/04/2015 | SLG \| ITO \| PEDOT:PSS \| Perovskite \| PCBM-60 \| Au | MAPbI$_3$ | 18.2 | [141] |
| Nie et al. | 29/01/2015 | SLG \| FTO \| PEDOT:PSS \| Perovskite \| PCBM-60 \| Al | MAPbI$_3$ | 17.7 | [142] |
| You et al. | 08/11/2014 | SLG \| ITO \| PEDOT:PSS \| Perovskite \| PCBM-60 \| PFN \| Al | MAPbI$_3$ | 17.1 | [143] |
| Chiang et al. | 25/07/2014 | SLG \| ITO \| PEDOT:PSS \| Perovskite \| PCBM-70 \| Ca \| Al | MAPbI$_3$ | 16.31 | [144] |
| Docampo et al. | 12/11/2013 | SLG \| FTO \| PEDOT:PSS \| Perovskite \| PCBM-60 \| TiO$_2$ \| Al | MAPbI$_3$ | 15.8 | [145] |

| | | SLG \| ITO \| PEDOT:PSS \| Perovskite \| PCBM-60 \| BCP \| Al | | | |
|---|---|---|---|---|---|
| Jeng et al. | 18/06/2013 | SLG \| ITO \| PEDOT:PSS \| Perovskite \| PCBM-60 \| BCP \| Al | $MAPbI_3$ | 3.9 | [146] |

*Table A2 p-i-n device efficiency records over the years*

| Author | Publication date | Cell architecture | Perovskite composition | PCE (%) | Reference |
|---|---|---|---|---|---|
| Zhou et al. | 06/03/2019 | SLG \| ITO \| HMB-doped $C_{60}$ \| Perovskite \| Carbon | $MAPbI_3$ | 16.03 | [147] |
| Zhang et al. | 07/02/2017 | SLG \| FTO \| $TiO_2$-c \| $TiO_2$-mp \| $Al_2O_3$-mp \| Perovskite \| Carbon | $MAPbI_3$ | 15.8 | [148] |
| Cai et al. | 31/01/2017 | SLG \| FTO \| ZnO-c \| Perovskite \| Carbon | $MAPbI_3$ | 15.1 | [149] |
| Tsai et al. | 28/11/2016 | SLG \| FTO \| $TiO_2$-c \| $TiO_2$-mp \| $Al_2O_3$-mp \| Perovskite \| Carbon | $MAPbI_3$ | 15 | [150] |
| Li et al. | 22/12/2015 | SLG \| FTO \| $TiO_2$-c \| $TiO_2$-mp \| $Al_2O_3$-mp \| Perovskite \| Carbon | $MAPbI_3$ | 14.7 | [151] |
| Yang et al. | 26/01/2015 | SLG \| FTO \| $TiO_2$-c \| $TiO_2$-mp \| $ZrO_2$-mp \| Perovskite \| Carbon | $MAPbI_3$ | 13.41 | [152] |
| Hu et al. | 26/08/2014 | SLG \| FTO \| $TiO_2$-c \| $TiO_2$-mp \| $ZrO_2$-mp \| Perovskite \| Carbon | $FA_{0.6}MA_{0.4}PbI_3$ | 12.9 | [153] |

| Mei et al. | 17/07/2014 | SLG \| FTO \| TiO$_2$-c \| TiO$_2$-mp \| ZrO$_2$-mp \| Perovskite \| Carbon | MAPbI$_3$ | 12.84 | [154] |
|---|---|---|---|---|---|
| Rong et al. | 06/06/2014 | SLG \| FTO \| TiO$_2$-c \| TiO$_2$-mp \| ZrO$_2$-mp \| Perovskite \| Carbon | MAPbI$_3$ | 10.64 | [155] |

*Table A3 Carbon-based HTL-free devices efficiency records over the years*

# References

[1] I. Šlaus and G. Jacobs. *Sustainability* 2011, 3, 97-154

[2] https://hdr.undp.org/en/content/human-development-index-hdi (last access: 10/06/22)

[3] https://www.bbc.co.uk/bitesize/guides/zpmmmp3/revision/1 (last access: 05/05/22)

[4] B. E. Dale and R. G. On. *Biotechnol. Prog.*, 2012, 28(4), 893–898.

[5] https://www.euro.who.int/en/health-topics/environment-and-health/Climate change/activities/raising-awareness-on-climate-change-and-health (last access: 05/05/22)

[6] https://www.repubblica.it/green-and-blue/2022/05/04/news/impronta_carbonio_eon_installazione_termoli-348098315/ (last access: 07/06/22)

[7] https://www.vaielettrico.it/ultimatum-bis-a-silk-faw-si-o-no-entro-il-25-luglio/(last access: 04/06/22)

[8] M. Pehl et al. *Nat Energy* 2017, 2, 939–945

[9] https://cordis.europa.eu/ (last access:10/06/2022)

[10] P. Potyrańska. Opportunities and threats for the introduction of nuclear power in Poland, 2020

[11] https://ember-climate.org/insights/research/global-electricity-review-2022/(last access:10/06/2022)

[12] https://www.iea.org/reports/global-energy-review-2021 (last access:10/06/2022)

[13] https://www.theweek.co.uk/news/world-news/russia/956614/which-countries-most-reliant-on-russian-gas (last access:10/06/2022)

[14] S. Ruhle. *Solar Energy* 2016, 130, 139–147

[15] A. Kojima et al. *J. Am. Chem. Soc.* 2009, 131, 6050–6051

[16] https://www.nrel.gov/pv/cell-efficiency.html (last access: 06/07/2022)

[17] C. Dong et al. *Adv. Funct. Mater.* 2021, 31, 2011242

[18] T. Leijtens et al. *Nat. Energy* 2018, 3, 828

[19] Q. Wali et al. *Renew. Sustain. Energy Rev.* 2018, 84, 89

[20] M.H. Futscher *ACS Energy Lett.* 2016, 1, 4, 863–868

[21] N. Savage. Solar cells that make use of wasted light. Nature 2021 (https://www.nature.com/articles/d41586-021-01673-w)

[22] M. Baranowski et al. *Adv. En. Mater.* 2020, 10, 1903659

[23] L.M. Herz et al. *ACS Energy Lett.* 2017, 2, 1539−1548

[24] J. Lim et al. *Energy Environ. Sci.* 2019, 12, 169-176

[25] Q. Dong et al. *Science* 2015, 347, 6225

[26] K.T. Munson *Chem*. 2018, 4, 2826–2843

[27] D.R. Ceratti et al. *Adv. Mat.* 2018, 30, 1706273

[28] D.R. Ceratti et al. *Mater. Horiz.* 2021, 8, 1570-1586

[29] I. Deretzis et al. *J. Phys. Chem. Lett.* 2018, 9, 11, 3000–3007

[30] H. Chen et al. *Small Struct.* 2021, 2, 2000130

[31] A.K. Jena et al. *Chem. Rev.* 2019, 119, 5, 3036–3103

[32] N.J. Jeon et al. *Nat Energy* 2018, 3, 682–689

[33] A. Alberti et al. *Rivista del Nuovo Cimento* 2019, 42, 7

[34] J.Y. Kim et al. *Chem. Rev.* 2020, 120, 15, 7867–7918

[35] V. M. Goldschmidt. *Naturwissenschaften* 1926, 14, 477–485

[36]        https://jaramillo.mit.edu/modified-goldschmidt-tolerance-factor-calculator-abx3-compounds (last access: 06/07/22)

[37] F. Ünlü et al. *APL Mater.* 2020, 8, 070901

[38] C. Li et al. *Acta Crystallogr., Sect. B: Struct. Sci.* 2008, 64, 702

[39] Q. Sun et al. *J. Am. Chem. Soc.* 2017, 139, 42, 14905–14908

[40] A. Marronnier et al. *ACS Nano* 2018, 12, 4, 3477–3486

[41] S. Singh et a. *J. Phys. Chem. Lett.* 2016, 7, 15, 3014–3021

[42] T.J. Jacobsson et al. *Nat Energy* 2022, 7, 107–115

[43] https://www.perovskitedatabase.com/home (last access:15/07/22)

[44] S.K. Sahoo et al. Chapter 1 - Introduction: Why Perovskite and Perovskite Solar Cells, Perovskite Photovoltaics, Academic Press, 2018, Pages 1-24,

[45] L. Yue et al. *Solar Energy* 2016, 124, 143–152

[46] D. Shi et al. *Science* 2015, 347, 519-522

[47] D. Ju et al. *Chem. Mater.* 2018, 30, 5, 1556–1565

[48] S. Gholipour and M. Saliba. Characterization Techniques for Perovskite Solar Cell Materials, Micro and Nano Technologies, 2020, Pages 1-22

[49] Z. Yang et al. *Nat Commun* 2019, 10, 4498

[50] C. Liang et al. *Nano Energy* 2019, 59, 721–729

[51] Y. Yu et al. *Solar Energy* 2020, 209, 408-414,

[52] B. P. Finkenauer et al. *ACS Appl. Mater. Interfaces* 2022, 14, 21, 24073–24088

[53] D. Cahen et al. *Acc. Chem. Res.* 2017, 50, 3, 573–576

[54] H. Zai et al. *Journal of Energy Chemistry* 2021, 63, 528–549

[55] S. Shao and M.A. Loi. *Adv. Mater. Interfaces* 2020, 7, 1901469

[56] A. Alberti et al. *Journal Phys. Chem. C* 2017, 121, 13577-13585

[57] G. Mannino et al. *Journal Phys. Chem. C*, 2017, 121, 7703-7710

[58] G. Niu et al. *J. Mater. Chem. A* 2014, 2 (3), 705-710

[59] N. Aristidou et al. *Angew. Chem. Int. Ed.* 2015, 54, 8208-8212

[60] B. Wang et al. *J. Am. Chem. Soc.* 2019, 141, 37, 14501–14504

[61] A. Fakharuddin et al. *Advanced Energy Materials* 2017, 7, 22, 1700623

[62] P. Schulz et al. *Chem. Rev.* 2019, 119, 5, 3349–3417

[63] H. S. Kim et al. *Scientific Reports* 2012, 2, 591.

[64] M. Liu et al. *Nature* 2013, 501, 395-398.

[65] Y. Lu et al. *Eur. J. Chem.* 2020 27, 3729-3736

[66] E.J. Juarez-Perez et al. *ACS Appl. Mater. Interfaces* 2019, 11, 13, 12586–12593

[67] A. Binek et al. *J. Phys. Chem. Lett.* 2015, 6, 1249–1253.

[68] E. Smecca et al. *Phys. Chem. Chem. Phys.* 2016, 18, 13413-13422

[69] R. Hu et al. *J. Mater. Chem. A* 2020, 8, 8058-8064

[70] Z. Li et al. *Nano Energy* 2020, 71, 104634.

[71] D. Liu et al. *Small Struct.* 2021, 2, 2000089

[72] H. Yao et al. *Mater. Chem. Front.* 2021, 5, 1221-1235

[73] J. Shi et al. *Energy Environ. Mater.* 2019, 2, 73–78

[74] A. J. Bett et al. *Energy Proc.* 2017, 124, 567.

[75] T. Leijtens et al. *Nat Energy* 2018, 3, 828.

[76] Y. Wang et al. *Science* 2019, 365, 591.

[77] H. Choi et al. *Nano Energy* 2014, 7, 80–85

[78] S. Tan et al. *Angew. Chem. Int. Ed*. 2022, 61, 23, e202201300

[79] W.S. Yang et al. *Science* 2017, 356, 1376-1379

[80] N.J. Jeon et al. *Nature Energy* 2018, 3, 682–689

[81] X. Wang et al. *Nat. Comm.* 2019, 10, Article number: 695

[82] E.T. Hoke et al. *Chem. Sci.* 2014, 6, 613–617

[83] C.G. Bischak et al. *Nano. Lett.* 2017, 17, 1028–1033

[84] S.J. Yoon et al. *ACS Energy Lett.* 2016, 1, 290–296

[85] J. H. Kim et al. *Adv. Mater.* 2015, 27, 695–701

[86] J. You et al. *Nat. Nanotechnol.* 2016, 11, 75–81

[87] E. Kasparavicius et al. *ACS Appl. Energy Mater.* 2021, 4, 12, 13696–13705

[88] G. Li et al. *Crystals* 2022, 12, 290

[89] Y. Yue, et al. *Adv. Mater.* 2016, 28, 10738–10743.

[90] G.-W. Kim et al. *ACS Appl. Mater. Interfaces* 2017, 9, 27720–27726

[91] A.K. Jena et al. *J. Mater. Chem. A* 2018, 6, 2219-2230

[92] https://shop.solaronix.com/ (last access: 18/07/22)

[93] C. C. Boyd et al. *ACS Energy Lett.* 2018, 3, 1772–1778.

[94] S. Svanstrom et al. *ACS Appl. Mater. Interfaces* 2020, 12, 7212–7221.

[95] B.Yang et al. *ACS Energy Letters* 2020, 5 (10), 3159-3167

[96] J. Qiu et al. *J. Mater. Chem. A* 2022, 10, 1821-1830

[97] E. Aktas et al. *Energy Environ. Sci.* 2021, 14, 3976

[98] D Bogachuk et al. *Energy Environ. Sci.* 2020, 13, 3880-3916

[99] J. Yan et al. *Sustainable Energy Fuels* 2022, 6, 243-266

[100] Y.Chen et al. *RSC Adv.* 2018, 8, 10489-10508

[101] H. Min et al. *Nature* 2021, 598, 444–450

[102] J. Song et al. *Sol. RRL* 2020, 4, 1900558

[103] A. Manekkathodi et al. *J. Mater. Chem. A* 2019,7, 26020-26028

[104] T. Bu et al. *Electrochimica Acta* 2019, 306, 635-642

[105] E. Bi et al. *Joule* 2019, 3 (11), 2748-2760

[106] J.I. Uribe et al. *ACS Appl. Energy Mater.* 2018, 1, 3, 1047–1052

[107] A. Bashir et al. *Nanoscale* 2018, 10, 2341-2350

[108] C.J. Clarke et al. *Chem. Rev.* 2018, 118, 747–800

[109] A. Albini and S. Protti. Paradigms in Green Chemistry and Technology. SpringerBriefs in Molecular Science. 2016. Springer, Cham.

[110] J.D. Chea. *Ind. Eng. Chem. Res.* 2020, 59, 5931–5944

[111] J.J. Yoo et al. *Nature* 2021, 590, 587–593

[112] H. Min et al. *Science* 2019, 366, 749-753

[113] E.H. Jung et al. *Nature* 2019, 567, 511–515

[114] N.J. Jeon et al. *Nat Energy* 2018, 3, 682–689

[115] W.S. Yang et al. *Science* 2017, 356, 376-1379

[116] M. He et al. *Nat. Comm.*2017, 8, Article number: 16045

[117] F. Di Giacomo et al. *Nano Energy* 2016, 30, 460-469

[118] M. Saliba et al. *Science* 2016, 354, 206-209

[119] D. Bi et al. *Nat. Energy* 2016, 1, 16142

[120] M. Saliba et al. *Energy Environ. Sci.* 2016,9, 1989-1997

[121] D. Bi et al. *Sci. Adv.* 2016, 2 (1)

[122] W.S. Yang et al. *Science* 2015, 348, 6240
[123] Y. Peng et al. *J. Mater. Chem. A* 2015, 3, 12436-12442
[124] H. Zhou et al. *Science* 2014, 345, 6196
[125] P. Docampo et al. *Nat. Commun.* 2019, 4, 2761
[126] M. Liu et al. *Nature* 2013, 501, 395–398
[127] J. Burschka et al. Nature 2013, 499, 316–319
[128] J.M. Ball et al. *Environ. Sci.* 2013, 6, 1739-1743
[129] M.M. Lee et al. *Science* 2012, 338, 643-647
[130] H.S. Kim et al. *Sci Rep* 2012, 2, 591
[131] J.H. Im et al. *Nanoscale* 2011, 3, 4088
[132] M. Degani et al. *Science Advances* 2021, 7, 49
[133] X. Zheng et al. *Nat Energy* 2020, 5, 131–140
[134] R. Lin et al. *Nat Energy* 2019, 4, 864–873
[135] M. He et al. *Nat Commun.* 2017, 8, 16045
[136] Y. Bai et al. *Nano Energy* 2017, 34, 58-68
[137] J. Zhao et al. *Energy Environ. Sci.* 2016, 9, 3650-3656
[138] Q. Wang et al. *Adv. Mat.* 2016, 28, 6734-6739
[139] Y. Shao et al. *Nat Energy* 2016, 1, 15001
[140] Q. Dong et al. *Energy Environ. Sci.* 2015, 8, 2464-2470
[141] J.H. Heo et al. *Energy Environ. Sci.* 2015, 8, 1602-1608
[142] W. Nie et al. *Science* 2015, 347, 522-525
[143] J. You et al. *Appl. Phys. Lett.* 2014, 105, 183902
[144] C.H. Chiang et al. *J. Mater. Chem. A* 2014, 2, 15897-15903
[145] P. Docampo et al. *Nat Commun.* 2013, 4, 2761.
[146] J.Y. Jeng et al. *Adv. Mater.* 2013, 25, 3727-3732.
[147] J. Zhou et al. *J. Mater. Chem. A* 2019, 7, 7710-7716.
[148] H. Zhang et al. *Adv. Mat.* 2017, 29, 1606608
[149] L. Cai et al. *J. Semicond.* 2017, 38, 014006
[150] C.M. Tsai et al. *J. Mater. Chem. A* 2017, 5, 739-747
[151] H. Li et al. *Nanoscale* 2016, 8, 6379-85
[152] Y. Yang et al. *J. Mater. Chem. A* 2015, 3, 9103-9107
[153] M. Hu et al. *J. Mater. Chem. A* 2014, 2, 17115-17121
[154] A. Mei et al. *Science* 2014, 345, 295-298.
[155] Y. Rong et al. *J. Phys. Chem. Lett.* 2014, 5, 12, 2160–2164

# Chapter 1: Stability of low temperature Eu-doped CsPbI₃

*The main challenge on CsPbI₃ resides in avoiding the transition from the photoactive black to the non-photoactive yellow phases. In this chapter, sustainability concerns new strategies 1) to form the photoactive CsPbI₃ black phase at low temperature and 2) to stabilize that phase at room temperature. To achieve this, a deep understanding of the mechanisms governing the phase transformation is required.*

*The data shown in this chapter were published in Advanced Energy and Sustainability Research (Alberti et al. 2021, 2, 2100091), Journal of Physics: Materials (Valastro et al. 2021, 4, 034011) and Solar RRL (Valastro et al. 2022, 6, 2200008).*

## 1.1    Low-temperature CsPbI₃: applications and challenges

Besides the most studied hybrid organic/inorganic perovskites (methylammonium lead iodide (MAPbI₃),[1] formamidinium lead iodide (FAPbI₃) and methylammonium (MA)-formamidinium (FA) mixed perovskite), the all-inorganic Cs-based perovskites[2] like CsPbI₃ have been receiving much attention in the last year owing to the mass preservation during operation. This occurs mostly because CsPbI₃ has a superior endurance against the formation of volatile species. Furthermore, CsPbI₃ perovskites are promising candidates for Si/PSK monolithic tandem solar cells due to the well-fitting value of energy gap ($E_{gap}$~1.73 eV).[3,4,5,6] Currently, two-terminal monolithic perovskite-on-silicon tandem cells represent the most promising innovative photovoltaic architecture for a near-term large-scale commercialization [7,8]. This technology allows reaching high efficiencies (the current record is 31.3% [9]) coupling a perovskite solar cell at relatively wide bandgap (top cell) with a silicon solar cell (bottom cell) which absorb in different and complementary regions of the solar spectrum. For this application, that is attracting interest and public/private investments, the use of low-temperature processes is mandatory. In monolithic tandem devices, in fact, the perovskite solar cell is deposited directly on the silicon cell and low-temperature processes (< 200°C) are indeed needed in order to avoid damaging underlying layers [3]. For this reason, forming photoactive CsPbI₃ black phases at low temperature is a main objective and the stabilization of CsPbI₃ black phases at room temperature is a main technological challenge.

## 1.2   Eu-doped CsPbI$_3$ phases: structural and optical characterization

The CsPbI$_3$ can take four crystallographic phases: cubic (α), tetragonal (β) and two orthorhombic (γ and δ). The α, β and γ phases have a perovskite structure with photovoltaic behaviour: they are better known as "black phases". The α-phase is stable at 325-350 °C.

The γ-phase[10, 11] can be formed through two different routes: 1) at low temperature (LT)[12] (~100 °C) by using additives.[13, 14, 15, 16, 17, 18,19] or 2) at high temperature (HT) (325-350 °C) by quenching the α-phase at RT[20,21,22,23] for CsPbI$_3$, with and without additives. As a drawback, the black γ-phase ($E_{gap}$ = 1.73 eV) is meta-stable at RT and indeed it spontaneously turns into the orthorhombic δ-phase well-known as "yellow phase": it is non-photoactive ($E_{gap}$ = 2.9 eV)[24,25,26] and indeed unusable for photovoltaic applications.

The HT procedure is technologically convenient since allows the black phase recovery by reconverting the yellow δ-phase to the black γ-phase with a simple annealing procedure; nonetheless, it is unapplicable in monolithic tandem solar cells and the LT route must be preferred with the use of additives.

Among the possible additives like hydroiodic acid (HI)[27,28,29], organic ligands [30, 31, 32,33] or elemental doping [34,35,36, 37,38,39] that enable the LT-black phase formation, it has been recently discussed [40], through a study at the atomistic scale, how a small addition of Europium[41] (Eu/Pb=5%) in the form of EuCl$_3$ (hereafter CsPbI$_3$:EuCl$_3$) or EuI$_2$ (hereafter CsPbI$_3$:EuI$_2$) in the precursor solution promotes the formation of a stable black γ-phase at 80 °C (LT- γ black) lasting for months at RT and N$_2$ environment (see following paragraph for further details). In the sample without Eu, a mixture of γ and δ phase is formed at 60 °C and it is unstable, thus converting to yellow after few hours at RT and N$_2$ environment. The schematic of the CsPbI$_3$ thin films (~80 nm) preparation by spin-coating method is represented in figure 1.1a and explained in the Methods section.

Figures 1.1c-d display the absorption coefficient as a function of the photon energy in CsPbI$_3$ samples with and without Eu, respectively. The absorption coefficient has been calculated from the real (ε$_1$) and imaginary (ε$_2$) parts of the dielectric function, obtained from Spectroscopic Ellipsometry (SE), using the formula [42]:

$$\alpha = \frac{2E}{c\hbar}\sqrt{\frac{\sqrt{\varepsilon_1^2+\varepsilon_2^2}-\varepsilon_1}{2}} \qquad \text{Eq. 1.1}$$

where E is the photon energy, c is the speed of light in vacuum and $\hbar$ is the reduced Planck constant.

The samples prepared with Europium start absorbing at the gap region with an abrupt tail, without any trace of yellow phase. By contrast, the profile of the absorption coefficient in pure CsPbI$_3$ is characterized by the presence of the featured peak of the yellow phase bandgap at 2.92 eV along with that of black phase, indicating a mixture of γ and δ phase, and by a large sub-bandgap feature in the range of 1-1.7 eV. This feature is attributed to the presence of intrinsic defects states in the material.[43]
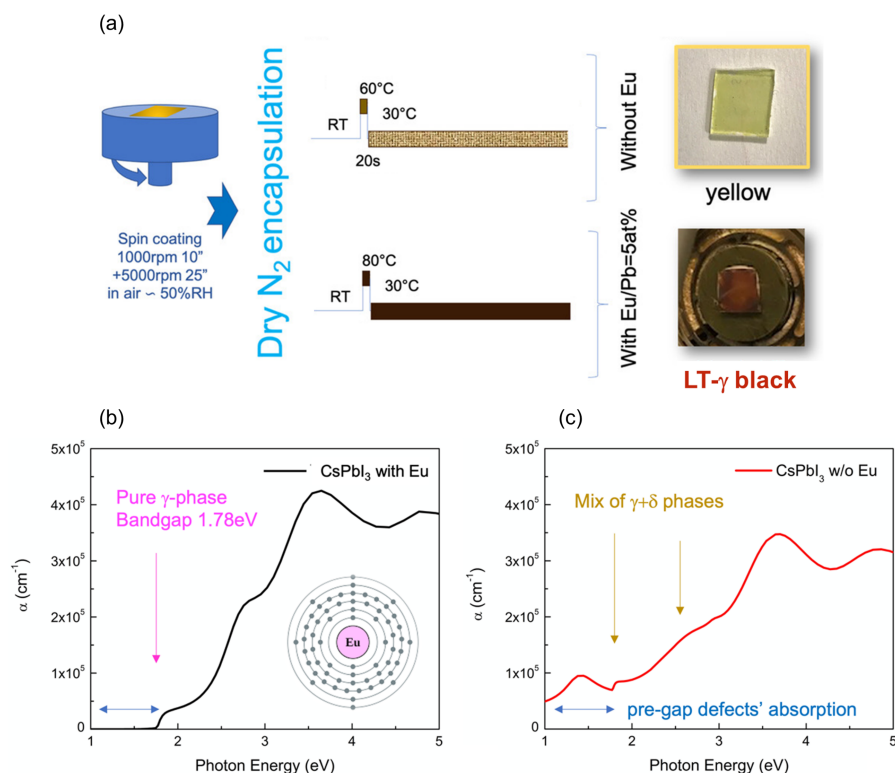


*Figure 1.1 a) Spin coating under air condition. Quenching procedures (0.5–1 °C s$^{-1}$) under dry N$_2$: without Eu precursor in the solution, 60 °C is the temperature to be used, and the resulting material has a dark-yellow colour; with Eu precursor in the spin-coated solution, the formation temperature is raised to 80 °C and the resulting film has a black colour. In this second case, the sample is long lasting for days. Absorption coefficient measured by Spectroscopic Ellipsometry in γ -CsPbI$_3$ with (b) and without Eu (c) incorporation, respectively. Note that pre-gap absorption and the smooth tail in (c). (Ref.[40]. Creative Commons License CC BY 4.0[44])*

Europium has a multiple role: 1) promoting the formation of the γ -phase through its ionic coordination with I$^-$ via octahedral bonding in synergy with Pb; this increases the nucleation rate of the γ-phase; 2) locally compensating charge deficiencies that likely arise from the different kinetics of atoms during reactions;

iodine-coordinated Eu atoms can indeed occupy interstitial positions to balance the lack of Cs atoms in the neighbourhood; 3) promoting the accumulation of exceeding and/or slower atoms in a compliant amorphous self-material that envelops the γ-phase into small-size grains of 5-20 nm (snowplow effect) [45,46,47] as shown in transmission electron microscopy image in figure 1.2a, with a convenient surface to volume ratio.
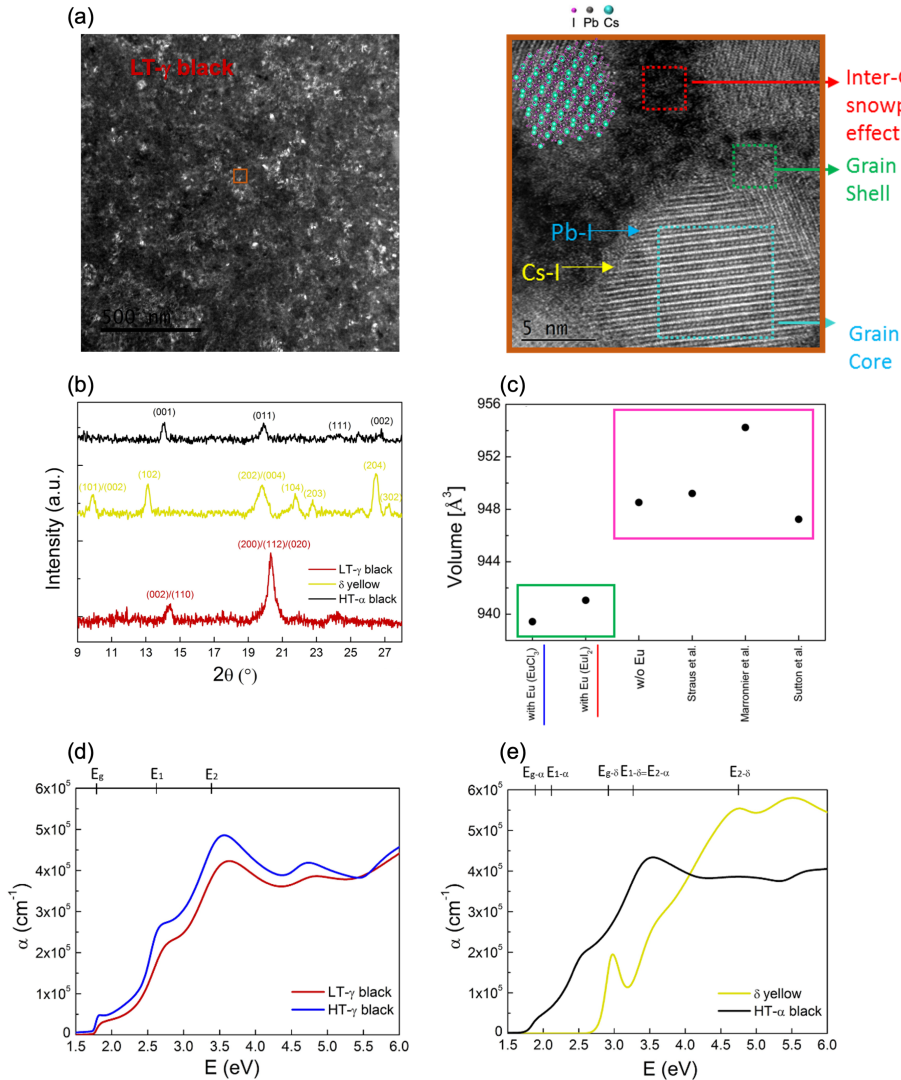


*Figure 1.2 (a) TEM image of the LT γ-phase film and HAADF-STEM image of small grains in the γ-phase framed by a gluing matrix of self-material. (b) XRD patterns and characteristic peaks with their Miller indexes of LT-γ black, δ yellow and HT-α black. (c) Cell unit volume measured for CsPbI$_3$:EuCl$_3$, CsPbI3:EuI$_2$, and CsPbI$_3$ samples prepared at low temperature. Absorption coefficient (α$_{cm-1}$) as a function of the photon energy (E$_{eV}$) for (d) LT γ-black and HT γ-black phases; (e) δ-yellow and HT α-black phases. (Refs.[40,48,49]. Creative Commons License CC BY 4.0 [44])*

The thermal annealing at 325 °C triggers the phase transition into HT-α black phase. When the HT-α black is slowly cooled from 325 °C to RT, the yellow δ-phase is formed[27] while, applying a fast quenching, an orthorhombic γ black phase (HT- γ black) is obtained. In this last case, the black phase is kinetically frozen thanks to the strain induced in the CsPbI$_3$ thin film [27,50]. In figure 1.2b, we show the X-ray diffraction patterns of the LT- γ black, HT-α black and yellow δ-phase along with the characteristic Miller indexes. LT- γ black is featured by the overlap of two peaks in the 2θ range 13.4-14.8°, that have been ascribed to (002) and (110) planes of the black γ-phase. The volumes of the unit cell for the films with the addition of EuCl$_3$ and EuI$_2$ were found to be very similar (~939-942 Å$^3$), which were significantly lower than those of our samples prepared without the addition of Eu and of black γ-phases formed by quenching the black cubic α-phase from high temperature (~350 °C), as reported in the literature (e. g. Marronnier et al.[51] Straus et al.[52], Sutton et al.[27]) (Figure 1.2c). The optical properties of CsPbI$_3$ doped with Eu have been investigated through SE measurements. The real (ε$_1$) and imaginary (ε$_2$) parts of the dielectric function extracted from SE measurements are shown in figure A1.1. The two black orthorhombic phases (HT and LT) have a very similar shape in terms of peaks and valleys in the absorption coefficient α (cm$^{-1}$) (Figure 1.2d). The absorption coefficient of the HT-α black phase compared to that of the non-photoactive δ yellow phase are drastically different as depicted in Figure 1.2e.

For a deeper understanding of the optical behaviour of the different phases of the film with a univocal criterion, we extracted the critical points (CPs) that are associated to specific optical transitions into the material. This approach, initially used by Cardona and co-workers [53,54] for semiconductors, has been recently extended to perovskites. We have recently used the same formalism to quantitatively and thoroughly describe degradation of perovskites and temperature evolution of inter-band transitions in bulk perovskites [55,56].

We have built up a Kramers-Kronig consistent optical model to fit experimental ellipsometry data and extract $\varepsilon(\omega)$ spectra. The real (ε$_1$) and complex (ε$_2$) part of the dielectric function of the material mirror the electronic band structure. By fitting simultaneously, the second derivatives of the real part ε$_1$ and the complex part ε$_2$ [53,54], the critical points (CPs) of the joint density of states, which represent the inter-band allowed transitions, are usually extracted. The overall fitting function is the sum of several functions, one for each CP, described by the equation [57]:

$$\frac{\partial^2 \varepsilon}{\partial \omega^2} = n(n-1)Ae^{i\Phi}(\omega - E + i\Gamma)^{(n-2)} \quad for \ n{\neq}0 \quad \text{Eq. 1.2}$$

where A (eV), Φ, E (eV), Γ(eV) and n are the amplitude, phase, energy position, broadening and the dimensionality of the CP. In general, the exponent n is -

½ for one dimensional, 0 for two dimensional or ½ for three dimensional critical points. When describing excitonic optical transitions typical of perovskite materials n=-1, as reported in refs [58,59].

Although one can see that the spectra are characterised by 5 CPs, going from the energy gap ($E_g$) to higher energy (above 5eV), the black-yellow-black phase transition can be effectively described by focusing on three of CPs, specifically the Energy gap ($E_g$), the second critical point ($E_1$) and the third critical point value ($E_2$). When the LT- γ black phase moves to the δ-yellow phase, the CP energy positions sharply increase, attesting the huge difference in the two crystallographic structures and the corresponding electronic structures. In particular, the bandgap value increases from the value typical of the $CsPbI_3$ black phase (1.78 eV) to that of the yellow phase (2.93 eV). The values of energy positions of each CP are reported in Table 1.1. At 325 °C, a sudden change of the CP energy occurs. In particular, all the CP energies move coherently to lower energies, attesting the formation of the α-black phase. This HT-α black phase, however, is not identical to the LT γ -black phase, as attested by the CP energy position reported in Table 1.1. As previously reported, if the sample is cooled down slowly (2.5 °C/min), a δ-yellow phase is formed at the end of the path (30°C). The only option to change the final state is to cool down the sample as quickly as possible (>100 °C/min). As a result, the phase formed after this fast quenching (HT-γ phase) has similar inter-band transition energies as the ones of the LT-γ phase (Table 1.1).

| | LT-γ black | δ Yellow | HT-α black | HT-γ black |
|---|---|---|---|---|
| $E_g$ (eV) | 1.781±0.001 | 2.932±0.001 | 1.897±0.001 | 1.779±0.001 |
| $E_1$ (eV) | 2.628±0.003 | 3.268±0.003 | 2.125±0.002 | 2.565±0.003 |
| $E_2$ (eV) | 3.43±0.03 | 4.68±0.01 | 3.27±0.02 | 3.39±0.02 |

*Table 1.1 Values of $E_g$, $E_1$ and $E_2$ critical points for LT- γ black at 30 °C, δ-yellow phase at 100 °C, HT-α black at 325 °C and HT γ-black phases as extracted from the critical point analysis.*

In the next paragraph, the stability of the $CsPbI_3$:$EuCl_3$ and $CsPbI_3$:$EuI_2$ black LT- γ phase and the mechanism of their transformation into the yellow δ-phase is investigated through thermal stability tests in the temperature range 60-100 °C.

## 1.3    Low-temperature Eu-doped CsPbI$_3$: thermal stability test on the γ-phase

To counteract the transformation trend from black γ- to yellow δ-phase, a deep understanding of the mechanisms governing the phase transformation is required. For this reason, we investigate the durability and the transformation path of the black LT γ-phase towards the yellow δ-phase. Stability tests are performed on both CsPbI$_3$:EuCl$_3$ and CsPbI$_3$:EuI$_2$ samples in a dry N$_2$ environment at five different temperatures of ageing (60-70-80-90-100 °C) by monitoring in real-time the evolution of the optical behaviour through in-situ isothermal Spectroscopic Ellipsometry measurements. A single SE measurement at a given temperature takes 25 minutes and the analyses are conducted consecutively until the transformation to yellow δ-phase is ended over hours or days. Figure A1.2 shows the real (ε$_1$) and (b) imaginary (ε$_2$) part of the dielectric function for initial black γ–phase of CsPbI$_3$:EuCl$_3$ and CsPbI$_3$:EuI$_2$

In Figure 1.3a-b, we show the real (ε$_1$) and imaginary (ε$_2$) parts of the dielectric function measured at 90 °C. For both the materials, we noticed a behaviour consisting of the decrease of dielectric function intensity around E$_{g\text{-black}}$ and the corresponding increase around E$_{g\text{-yellow}}$. According to DFT simulations, this phase transformation from a perovskite orthorhombic black γ-phase (Figure 1.3c) to a non-perovskite orthorhombic yellow δ-phase (Figure 1.3d) implies a rearrangement of the lattice structure with a significant mass displacement that involves several species including Cs, the biggest atom in the system.

In Table 1.2 we provide energies (E) and amplitudes (A) extracted from CP analysis for black γ-phase and yellow δ-phase of both materials whereas the complete set of fitting parameters is given in Table A1.1-1.4 of the Appendix.

| | *CsPbI$_3$:EuCl$_3$* | | *CsPbI$_3$:EuI$_2$* | |
|---|---|---|---|---|
| | Black γ-phase | Yellow δ-phase | Black γ-phase | Yellow δ-phase |
| *E$_g$ [eV]* | 1.79 | 2.93 | 1.79 | 2.92 |
| *A$_{Eg}$ [eV]* | 0.84 | 4.96 | 0.81 | 4.02 |

*Table 1.2 Energy and Amplitude fit parameters of all CPs of CsPbI$_3$:EuCl$_3$ and CsPbI$_3$:EuI$_2$*

In the methods section and appendix, we discuss in detail the optical model used to fit the experimental data Ψ and Δ during the three different stages of transformation, specifically at the beginning when the film lies in the black γ-phase (Figure A1.3), during the coexistence of black γ-phase and yellow δ-phase (Figure A1.4) and at the end as the phase transformation to yellow δ-phase is completed (Figure A1.5).
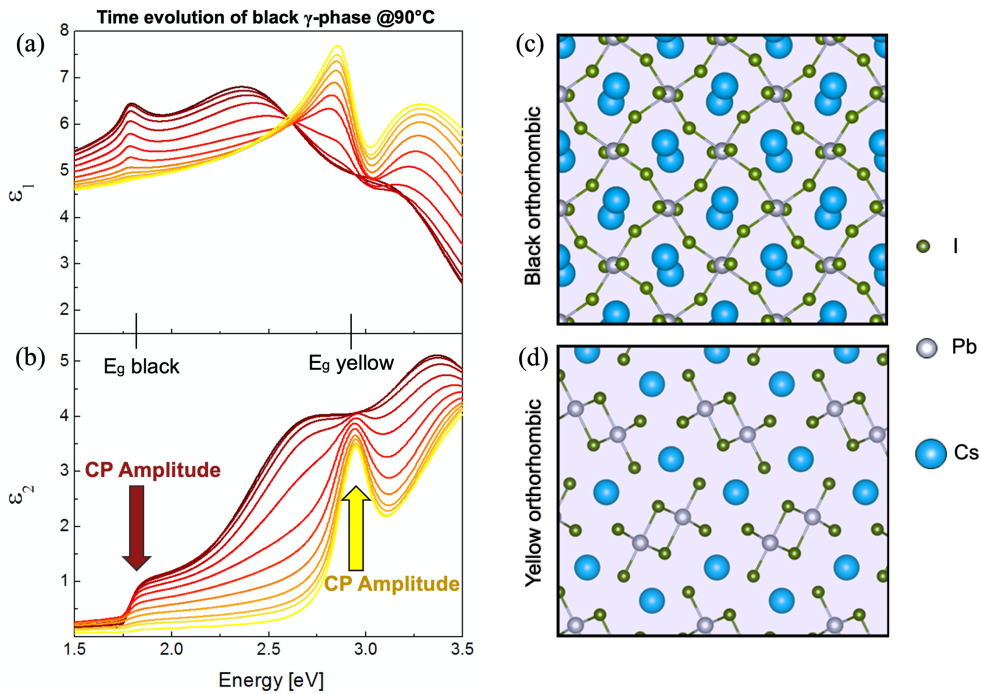


*Figure 1.3. Evolution at 90 °C of ε₁ (a) and ε₂ (b) functions during the phase transformation from black γ-phase to yellow δ-phase. (c) Black γ-phase structure based on DFT calculations projected on the (001) plane. (d) Yellow δ-phase structure based on DFT calculations projected on the (010) plane. (Ref. [48]. Creative Commons License CC BY 4.0[44])*

Among all the existing CPs, the most diagnostic are those at the energy bandgap[60,61] of black γ-phase and yellow δ-phase ($Eg_{black} = 1.78$ eV and $Eg_{yellow} = 2.92$ eV at RT[62]). In particular, we have monitored the $Eg_{black}$ over the annealing time at a fixed temperature to have a preliminary and qualitative estimate of the phase transformation time scale.

We observed that the energy gap of the black γ-phase progressively undergoes a blueshift during the phase transformation with a sudden increase in the last transformation steps when the black γ-phase vanishes and the yellow δ-phase dominates, as shown in Figure 1.4a-b for both CsPbI$_3$:EuCl$_3$ and CsPbI$_3$:EuI$_2$ samples. We note that a shift of only 2.5% from 1.78 eV to 1.825 eV testifies the irreversible degradation of the sample. The phenomenon has been observed at any temperature, i. e. 60-100 °C, at different time scales. We speculate that the increase of the energy gap value is linked to a structural stretching of the residual black γ-phase embedded in the yellow δ-phase occurring in the last stages of phase transformation.[63]
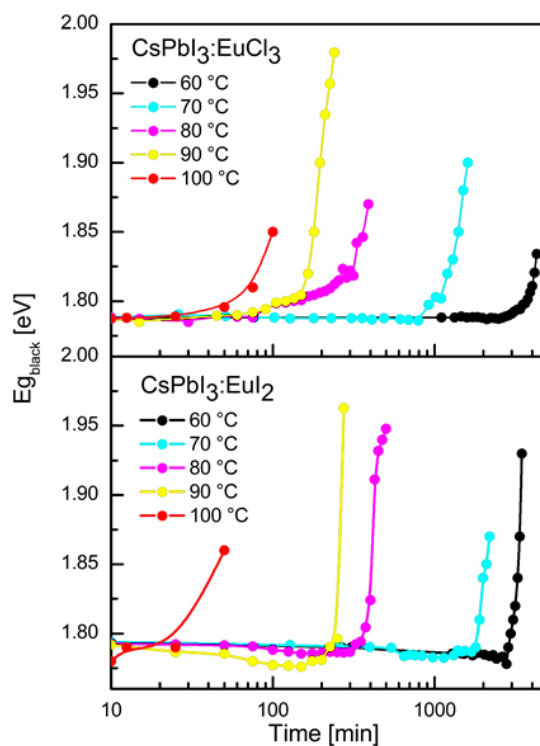


*Figure 1.4 Trend of the E$_g$ values measured in the black γ-phase at different temperatures of ageing for (a) CsPb$_3$I:EuCl$_3$ and (b) CsPbI$_3$:EuI$_2$. (Ref. [48]. Creative Commons License CC BY 4.0[44])*

We implemented an analytical approach to quantify the amount of γ to δ phase change at different temperatures. The two phases on the same sample at the beginning (γ-phase) and the end (δ-phase) of the transformation are shown in figure 1.5a. We used the amplitude A (see Eqs. 1.3 and 1.4) of the CP at the energy gap (A$_{Eg}$) of both phases, namely A$_{Eg-b}$ and A$_{Eg-y}$, as diagnostic parameters. This approach allowed obtaining a comprehensive description of the perovskite degradation process, based on the phase trade-off.

For easier comparison, the amplitude data over time have been respectively normalized to the initial amplitude value of the CP at energy bandgap of black $\gamma$-phase ($A_{Eg-b}$) at t = 0 min, when the material exists in the black $\gamma$-phase, and to the final value of $A_{Eg-y}$ when the transformation to yellow $\delta$-phase is completed.

In Figure 1.5b-c, we show a representative case of $A_{Eg}$ normalized amplitude curves for $CsPbI_3$:$EuCl_3$ taken at 60 °C (see also Figure A1.6 and Figure A1.7 for all temperatures and both $CsPbI_3$:$EuCl_3$ and $CsPbI_3$:$EuI_2$ layers). It is worthy to note that the specular trend of the two curves that reflects the complementary exchanging amount of each phase during the transformation from black $\gamma$-phase to yellow $\delta$-phase, behaving as two sides of the same coin: the growth of yellow $\delta$-phase occurs with the consumption of the black $\gamma$-phase in the film.
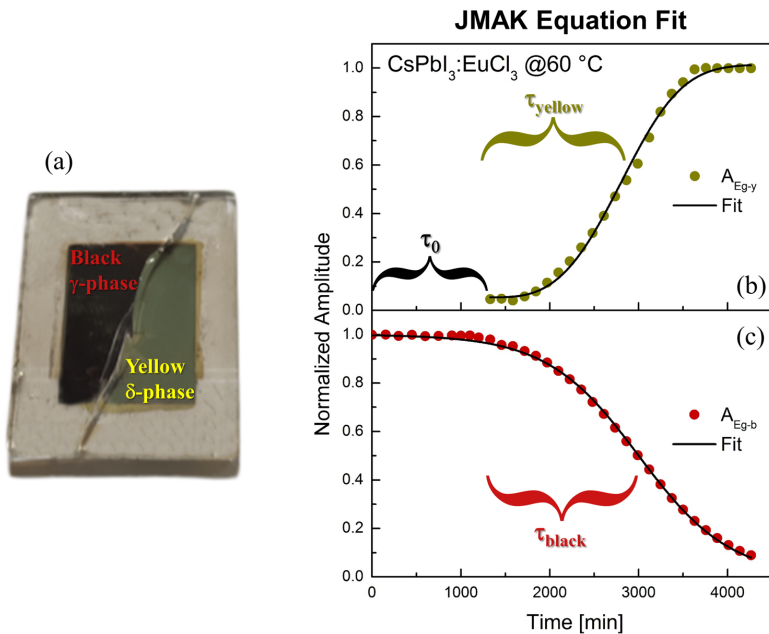


*Figure 1.5 (a) Pictures of the black $\gamma$-phase and yellow $\delta$-phase in a CsPbI$_3$:EuCl$_3$ sample (two phases of the same coin). Trend over time of the normalized amplitude of the CP at Eg (A$_{Eg}$) for (b) yellow $\delta$-phase (A$_{Eg-y}$) and (c) black $\gamma$-phase (A$_{Eg-b}$) of CsPbI$_3$:EuCl$_3$ at T = 60 °C fitted by the JMAK equation (see text). The incubation time $\tau_0$ and the characteristic times for the black $\gamma$-phase $\tau_{black}$ and for the yellow $\delta$-phase $\tau_{yellow}$ are indicated. (Ref. [48]. Creative Commons License CC BY 4.0[44])*

The sigmoidal shape of the curves (Figure 1.5b-c) is typical behaviour of solid-state phase transformation, characterized by nucleation and growth processes, which are described by the well-known Johnson-Mehl-Avrami-Kolmogorov (JMAK) equations.[64,65,66,67,68] The JMAK model is largely used to quantify thermodynamic and kinetic parameters of crystallization at a constant temperature[69] and it has been

recently applied to CsPbIBr$_2$, as reported in Ref. [70]. Both curves in Figure 1.5 were accordingly fitted by the following JMAK equations:

$$A_{Eg-y}(t) = 1 - e^{-\left(\frac{t-\tau_0}{\tau}\right)^n} \qquad \text{Eq. 1.3}$$

$$A_{Eg-b}(t) = 1 - \left(1 - e^{-\left(\frac{t-\tau_0}{\tau}\right)^n}\right) \qquad \text{Eq. 1.4}$$

The parameter $\tau_0$ is the incubation time which accounts for the initial stage of nucleation and growth of the first over-critical nuclei of the yellow $\delta$-phase. This incubation represents from one side the time needed, in the modelling of optical data, to use an additional oscillator that takes into account the CP at Eg$_{yellow}$ and on the other side it coincides with the time needed for the amplitude of the oscillator at Eg$_{black}$ begins to decrease (Figure 1.5b-c). In addition to this parameter, $\tau_{black}$ and $\tau_{yellow}$ can be extracted (with JMAK equation) as the characteristic times at which, after $\tau_0$, the amplitude reaches the value of $1 - \frac{1}{e}$ (~0.63) and $\frac{1}{e}$ (~0.37) of its maximum, respectively.[71] Finally, n is the Avrami exponent which mirrors the growth mechanism of the nuclei as discussed below. The most reliable fitting procedure has been obtained by fixing $\tau_0$ as extracted by the experimental data (see Figure 1.5b-c) and using the Avrami exponent n and $\tau$ as fitting parameters; a further refinement is done by leaving $\tau_0$ participating to fit for $\chi$-square minimization.

The values of incubation time $\tau_0$ and characteristic time $\tau$ for both black $\gamma$-phase and yellow $\delta$-phases at each temperature have been separately extracted and represented as a function of the reciprocal temperature of annealing in a semilogarithmic plot in Figure 1.6. Each of the parameters, i.e. $\tau_0$ and $\tau$, was fitted with the Arrhenius equation[72]:

$$B = B_0 e^{-\frac{E_a}{k_B T}} \qquad \text{Eq. 1.5}$$

where B$_0$, E$_a$, k$_B$, T represent the pre-exponential factor, the activation energy, the Boltzmann constant, and the absolute temperature. With this equation, we fit separately the temperature dependence of characteristic times of the Avrami equation (i.e. $\tau_0$, $\tau_{black}$ and $\tau_{yellow}$). A plot of the lnB versus 1/k$_B$T is linear with a slope equal to Ea and y-intercept equal to lnB$_0$. In this way, the values of activation energy and the natural logarithm of a pre-exponential factor related to $\tau_0$ (Ea$_{\tau0}$ and ln(B$_0$)$_{\tau0}$) and $\tau$ (Ea$_\tau$ and ln(B$_0$)$_\tau$) are extracted, as reported in Table 1.3. We observe that the activation energy and the ln of pre-exponential factor related to the incubation time $\tau_0$ are slightly higher than those related to the characteristic time $\tau$ for both CsPbI$_3$:EuCl$_3$ and CsPbI$_3$:EuI$_2$. This aspect will be clarified by what follows. Comparing the two kinds of samples, the values of both Ea$_{\tau0}$ and Ea$_\tau$ for CsPbI$_3$:EuCl$_3$ are higher than those for CsPbI$_3$:EuI$_2$ (1.50 vs 1.19 eV and 1.15 vs 0.95 eV), indicating a higher activation

energy needed for the black γ-phase to yellow δ-phase transformation (degradation process) in CsPbI$_3$:EuCl$_3$. In contrast, the values of $\ln(B_0)_{\tau0}$ and $\ln(B_0)_\tau$ have an opposite trend (-34.13 vs -44.94 and -25.63 vs -32.65), with CsPbI$_3$:EuI$_2$ having higher values than CsPbI$_3$:EuCl$_3$. We argue that these values of the pre-exponential factor are due to a low entropic contribution, which implies that the CsPbI$_3$:EuI$_2$ lattice is characterized by a lower frequency of events which contribute to phase transformation to yellow δ-phase with respect to CsPbI$_3$:EuCl$_3$. The combination of activation energy and pre-exponential factor values explains the behaviour of CsPbI$_3$:EuCl$_3$ compared to CsPbI$_3$:EuI$_2$: for T > 60 °C the CsPbI$_3$:EuI$_2$ the black γ-phase film shows better stability than CsPbI$_3$:EuCl$_3$, but for T < 60 °C the black γ-phase of CsPbI$_3$:EuCl$_3$ lasts longer than those of CsPbI$_3$:EuI$_2$. In the latter (EuCl$_3$), the projected durability of the material at 30 °C in dry N$_2$ environment is ~250 days at room temperature. As a further comment, we found it noteworthy that the extracted values of Ea$_\tau$ and $\ln(B_0)_\tau$ calculated by fitting the amplitude data of two different critical points (black γ-phase and yellow δ-phases CPs) are very similar, as two sides of the same coin. This convergence reinforces our conclusions.
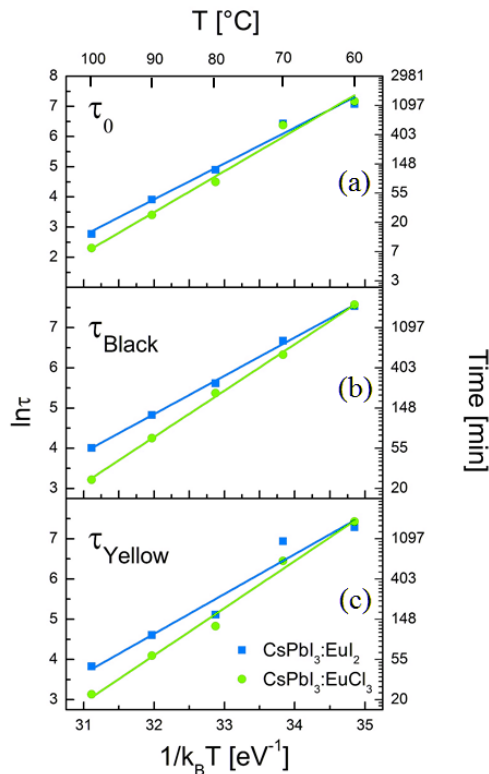


*Figure 1.6 Arrhenius plots of the lnτ versus 1/k$_B$T referred to the incubation time τ$_0$ (a) and characteristic times of the Eg$_{black}$ decrease (τ$_{Black}$) (b) and the Eg$_{yellow}$ growth (τ$_{Yellow}$) (c) for CsPbI$_3$:EuCl$_3$ and CsPbI$_3$:EuI$_2$. (Ref. [48]. Creative Commons License CC BY 4.0[44])*

| | $Ea_\tau$ [eV] | $Ea_{\tau 0}$ [eV] | $ln(B_0)_\tau$ | $ln(B_0)_{\tau 0}$ |
|---|---|---|---|---|
| CsPbI$_3$:EuI$_2$ Yellow δ-phase | 0.98±0.12 | 1.19±0.08 | -25.48±4.72 | -34.13±2.70 |
| CsPbI$_3$:EuCl$_3$ Yellow δ-phase | 1.17±0.07 | 1.50±0.12 | -33.45±2.37 | -44.94±4.06 |
| CsPbI$_3$:EuI$_2$ Black γ-phase | 0.95±0.02 | 1.19±0.08 | -25.63±0.67 | -34.13±2.70 |
| CsPbI$_3$:EuCl$_3$ Black γ-phase | 1.15±0.02 | 1.50±0.12 | -32.6±0.73 | -44.94±4.06 |

*Table 1.3 Values of the activation energy ($E_a$) and the natural logarithm of pre-exponential factor $ln(B_0)$ extracted from fitting with Arrhenius equation the incubation time $\tau_0$ and characteristic times $\tau$ of the CP at the CP at Eg-yellow growth ($\tau_{Yellow}$) and Eg-black decrease ($\tau_{Black}$) versus $1/k_B T$*

In addition to the characteristic times, we calculated the Avrami exponent n by fitting the amplitudes $A_{Eg-y}$ and $A_{Eg-b}$ (see Figure 1.5). Since, for each material, there is not a trend with temperature, all n values for the five temperatures are graphed in boxplots in Figure 1.7a. We observe that the Avrami exponent for CsPbI$_3$:EuI$_2$ lies in the range of 1.2-1.8 with a mean value 1.5, whilst the values measured for CsPbI$_3$:EuCl$_3$ lies in the range of 1.8-2.4 with a mean value 2.
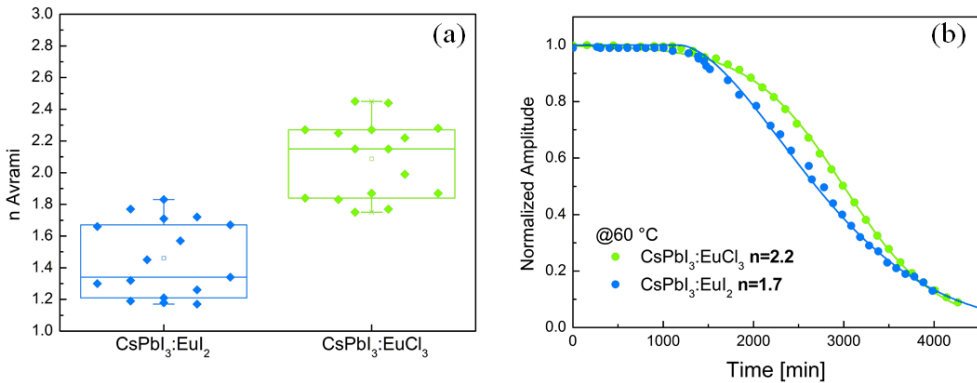


*Figure 1.7 (a) Boxplots of Avrami exponent (n) obtained by fitting with JMAK equation (see text). (b) Normalized amplitude of $A_{Eg}$ vs time for both CsPbI$_3$:EuCl$_3$ and CsPbI$_3$:EuI$_2$ at T = 60 °C. The different slope of the two curves reflects the different value of n. (Ref. [48]. Creative Commons License CC BY 4.0[44])*

The difference of the Avrami exponent for the two kinds of samples is immediately visualized by observing the slope variations in the amplitude $A_{Eg}$ vs time

curves at the ageing temperature of 60 °C (Figure 1.7b). In this representative case, n = 1.7 for $CsPbI_3$:$EuI_2$ and n = 2.2 for $CsPbI_3$:$EuCl_3$. In both samples, a bidimensional phase transformation is disclosed on the basis of the n values with the activation energy listed in Table 1.3. The little systematically higher n values measured in the case of using $EuCl_3$ accounts for a generally slightly steeper transformation tail.

In order to go deeper into the phase transformation, we have performed TEM analyses with associated electron diffraction analyses for phase identification. We monitored in-situ at a fixed temperature the complete transformation from the black γ-phase to yellow δ-phase. In Figure 1.8 we show the analyses performed on $CsPbI_3$:$EuCl_3$, as a representative sample. The protocol used for this investigation is the following: the perovskite solution is deposited directly on a carbon-coated Cu grid and spin-coated as reported in the Methods section; it is annealed on a hot plate in the ambient environment for 1 min 30% RH and loaded immediately into the vacuum chamber of the microscope; for each step, the temperature of the sample is ramped up to 80 °C and maintained stable for 25 minutes. We have observed that the electron beam can accelerate the degradation process by increasing nucleation rate and growth during heating thus leading to erroneous interpretation about the phase transformation, as shown in Figure A1.8. For this reason, we defined the following free-of-artifact protocol: medium electron dose ~50 e-/$Å^2$s [73]; after each acquisition, we have stopped the beam irradiation on the sample and waited for a fixed time interval before acquiring a second frame on a fresh area (thus being evolved just as an effect of the applied temperature and not under electron beam irradiation). To decrease the statistical error, we have analysed six different areas of the sample for every single annealing step.

Figure 1.8a shows the representative plane-view bright-field TEM image of the as-prepared black γ-phase at RT which is characterized by large aggregates (1-3 μm) composed of small grains (5-20 nm). The dark field image in Figure 1.8b, acquired in the same area of Figure 1.8a, shows a uniform distribution of bright and dark spots that are the small grains of the black γ-phase. Darkfield images taken on specific diffraction features of the yellow δ-phase allow us to easily identify the yellow δ-phase grains nucleated within the black γ-phase. They are characterized by a large size and uniform contrast.

During the first annealing step at 80 °C, there is no evidence of yellow δ-phase nucleation. After an incubation time $τ_0$ (~100 min), which is fully consistent with that obtained by SE measurements, the first evidence of yellow δ-phase grains, indicated by yellow circles in Figure 1.8c, is found (80-150 nm diameter) homogeneously appearing through the area. After further 50 minutes at 80 °C, the sample appears as shown in Figure 1.8d. We observe that the grains are increased in density (nucleation still occurring) and size in the range of 80-400 nm.

The area of the film outside the nucleated yellow grains is still the initial black γ-phase, as confirmed by the selected area diffraction in Figure 1.8e. This diffraction pattern, characterized by rings typical of the fine-grained structures, is univocally attributed to orthorhombic γ-phase. On the contrary, the pattern of the yellow δ-phase grain (Figure 1.8e) composed of ordered isolated diffraction spots, highlights the single-crystal nature of the yellow δ-phase domains. The presence of small nuclei of the yellow δ-phase after $\tau_0$+50 mins suggests that the nucleation phenomena continue to arise during the phase transformation, and this agrees with a similar value of the extracted activation energies related to $\tau$ and $\tau_0$ (Ea$_\tau$ and Ea$_{\tau0}$) for CsPbI$_3$:EuCl$_3$ sample (1.15 eV vs 1.50 eV). The value of nucleation rate has been extracted from the TEM images and it is equal to ~0.09 nuclei/min at 80 °C. This value is used as a constant in the simulation of the yellow δ-phase nucleation and growth performed using the "Fast Marching" method[74]. As relevant modification with respect to the conventional approach, which starts from an initial fixed profile (see e. g. Ref.[75]), successive nucleation of yellow phase seeds is implemented in the non-transformed space region reinitializing the Fast-Marching algorithm at each new nucleation event. The value of growth speed has been used as a parameter to fit the experimental data of SE measurements and a value of 3.2 nm/min has been found. The graphical representation of the simulation of the yellow grain nucleation and growth after $\tau_0$+50 mins is displayed in figure 1.8g (see Figure A1.9 for the complete representation). The results of the simulation in terms of yellow δ-phase amount over time combined with the SE experimental data are shown in Figure 1.8h.
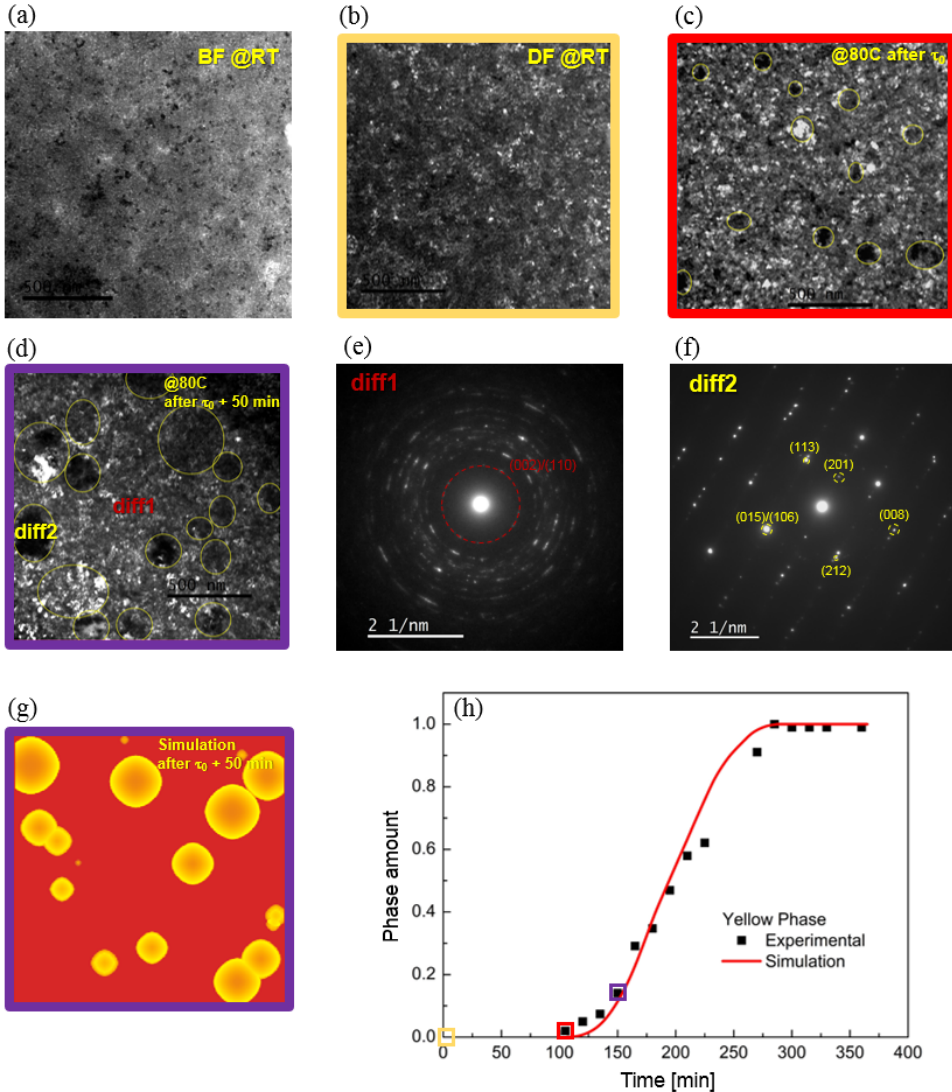
*Figure 1.8 (a) TEM image of the as-prepared black γ-phase at RT in bright field (BF) and (b) dark field (DF) mode. (c) TEM image of the sample after thermal cycle at 80 °C for a period equals to incubation time $\tau_0$ (~100 min) and (d) for a period equals to $\tau_0$ + 50 min. The yellow grains are indicated with yellow circles. (e)-(f) Selected area diffraction with the labelled Miller indexes acquired in the region indexed as "diff" (black γ-phase) and "diff2" (yellow δ-phase) in Figure 1.8d. (g) Graphical representation of the yellow grains nucleation and growth obtained by "Fast Marching" simulation after $\tau_0$+50 mins. (h) Experimental and simulated values of yellow δ-phase normalized amplitude over time. (Ref. [48]. Creative Commons License CC BY 4.0[44])*

To summarize, we found that the durability of CsPbI$_3$ with Eu, especially using EuCl$_3$, is extended hugely above what occurs without Eu, i.e. ~250 days vs. a few hours at room temperature. The use of EuI$_2$ is instead more convenient to extend durability for operation temperature above 60 °C.

Our key-of-understanding and the launched analytical method can be freely applied to any kind of perovskite material and thickness during thermal or environmental stress tests to evaluate any kind of additive, interlayer, overlayer, molecules for stabilization purposes or for comparative preparation methodologies.

Lastly, our findings bear a technological impact in defining a viable strategy to form and stabilize the yellow γ-phase in a way fully compatible with the flow-chart of tandem devices, and for that this theme deserves further special attention. Beyond the efficiency value itself (Figure A1.10) that could be further improved with focused systematic studies to identify more convenient device architectures, we would like to point out the importance of the trade-off between low-temperature processes and durability perspectives.

We believe that, once the black γ-phase is formed at LT and stabilization strategies are consolidated, CsPbI$_3$ can be a better option than other perovskites to enter a large market share.

## Methods

*Perovskite Film Fabrication*: A mix solution of 1 M PbI$_2$ (Tokyo Chemical Industry) and 1 M CsI (Tokyo Chemical Industry) was prepared by mixing them in a mixed solvent of DMF and DMSO (3:1 v/v). EuCl$_3$ (Sigma-Aldrich) and EuI$_2$ (Sigma-Aldrich) solutions of 0.1 M concentration were made in a mixed solvent of DMF and DMSO (3:1 v/v). The solutions were stirred at room temperature for 1 h. Then, 1 ml of the PbI$_2$/CsI solution was mixed respectively with 0.5 ml of the EuCl$_3$ solution for CsPbI$_3$:EuCl$_3$ samples and with 0.5 ml of the EuI$_2$ solution for CsPbI$_3$:EuI$_2$ samples to reach the desired stoichiometry and then stirred for 1 h. The perovskite films were deposited by spin-coating the precursor solutions in ambient environment (RH~30%) on glass substrate in two steps: 1000 rpm for 10 s followed by 5000 rpm for 25 s. Then the CsPbI$_3$:EuCl$_3$ and CsPbI$_3$:EuI$_2$ films were annealed respectively at 80 °C and 90 °C inside of the N$_2$ filled chamber of the ellipsometer for 1 min and then quenched at RT to form black γ-phase (thickness ~80 nm). The use of a different formation temperature serves to level the transformation times and indeed the kinetic of formation. The two families of samples, characterized by XRD, have similar black γ-phase lattice structure at room temperature.

*X-Ray Diffraction*: XRD patterns were collected using a D8Discoved (Bruker AXS) diffractometer equipped with a high-precision goniometer (0.0001 Å), a thin film attachment (long soller slits), and a Cu Kα source (instrumental broadening 0.07°). The acquisition time corresponded to the use of a step size of 0.01° and acquisition time 1 s per step.

*Spectroscopic Ellipsometry*: We used a V-VASE, J A Woollam spectroscopic ellipsometry equipped with an autoretarder for optical characterization. Ellipsometric data have been collected at different angles below and above the Brewster angle of the glass substrate, over a wide range of wavelengths 245-1240 nm (1-5 eV) with step of 10 nm or less (5 nm) depending on the curve steepness. The optical model is a three-layer model that considers the optical constants of the glass substrate, the perovskite layer and the surface layer needed to simulate the layer roughness. Within the effective model approximation this last layer is assumed to be made 50% of the upper layer (air) and 50% of the lower layer (perovskite). The presence of a transparent substrate has been properly considered including the possibility that part of the light hits the back surface of the glass slide. We build a Kramers-Kronig consistent optical model based on multiple Critical Points Parabolic Band (CPPB) oscillators to fit experimental data ($\Psi$ and $\Delta$) and determine the real and imaginary part of the dielectric function. Measurements have been collected using a slightly over pressurized $N_2$ filled chamber in order to prevent perovskite degradation in air. The cell setup allowed to vary the temperature in the range 30-100 °C with an Instec MK100 heater/cooler system with an accuracy of 0.1 °C. Although it is known that $CsPbI_3$ is orthorhombic and therefore it presents an optical anisotropy along the three axes, this property has not been considered since the sample is a randomly oriented polycrystalline layer.

*Transmission Electron Microscopy:* TEM analyses were done in plan-view using a JEOL JEM 2010F microscope operating at 200 kV. Carbon coated Cu grids placed on a glass substrate were subjected to solution dispersion, spin coating and annealing following the same procedure described above. After black phase formation the grids were mounted on a Gatan heating holder and inserted in the TEM column in a couple of minutes, avoiding the prolonged contact with air. During in-situ annealing the temperature was ramped up from 25 °C to 80 °C in 2 minutes, and it was maintained stable for 20 minutes. In order to avoid effects on the phase change speed caused by the electron beam irradiation during the annealing steps (figure A1.8), they were conducted with the electron beam valve closed. At the end of the annealing step, the sample was cooled to room temperature before opening the e-beam shutter. Bright and dark field images of the same area were acquired in six fresh (not irradiated) regions of the sample, in order to more precisely recognize the yellow phase grains formed inside the fine-grained poly-crystalline black phase. The grains circled in the dark field images used in the text were identified using the combination of the two twin images of the same area. A new region was selected at every annealing step, in order to avoid artefacts related to electron irradiation. The grains number for each step was extracted by adding the grains of all the six images.

# Appendix

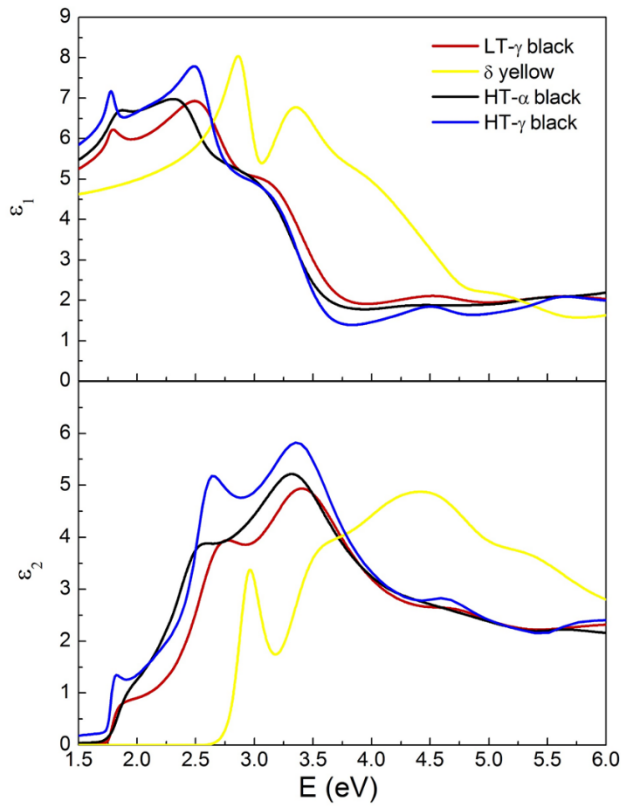The appendix of this chapter contains supplementary figures, tables and equations.



*Figure A1.1 Real and imaginary part of the dielectric function of the three black phases (LT-γ black, HT-α black and HT-γ black) and the yellow phase (δ yellow) (Ref. [48]. Creative Commons License CC BY 4.0[44])*
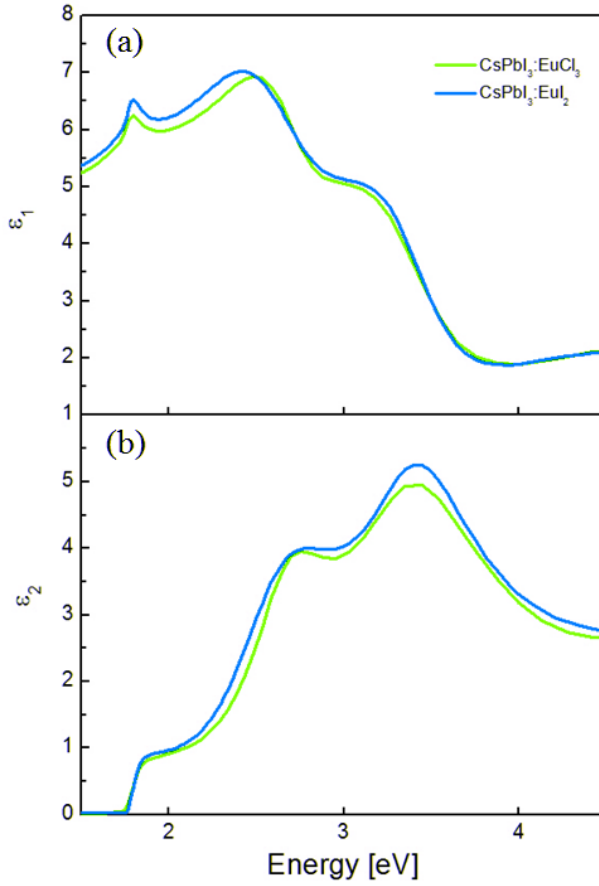
*Figure A1.2 (a) Real (ε₁) and (b) imaginary (ε₂) part of the dielectric function for initial black γ–phase of CsPbI₃:EuCl₃ and CsPbI₃:EuI₂ (Ref. [48]. Creative Commons License CC BY 4.0⁴⁴)*

|  | CsPbI₃:EuCl₃ black γ-phase | | | |
|---|---|---|---|---|
|  | $E_g$ | $E_1$ | $E_2$ | $E_3$ |
| E (eV) | 1.79 | 2.57 | 3.36 | 4.33 |
| A (eV) | 0.84 | 3.41 | 3.77 | 1.10 |
| Γ (eV) | 0.08 | 0.53 | 0.63 | 0.77 |
| Φ (rad) | -45.87 | 2.31 | 16.53 | -80.49 |

*Table A1.1 Critical point energy (E), broadening (Γ), amplitude (A), and phase (Φ) as extracted from fitting of Eq. 1.2 in the main text for the CsPbI₃:EuCl₃ black γ-phase.*

*CsPbI$_3$:EuCl$_3$ yellow δ-phase*

|  | E$_g$ | E$_1$ | E$_2$ |
|---|---|---|---|
| *E (eV)* | 2.93 | 3.19 | 4.21 |
| *A (eV)* | 4.96 | 3.74 | 5.13 |
| *Γ (eV)* | 0.15 | 0.31 | 1.74 |
| *Φ (rad)* | 17.22 | -93.96 | 31.04 |

*Table A1.2 Critical point energy (E), broadening (Γ), amplitude (A), and phase (Φ) as extracted from fitting of Eq. 1.2 in the main text for the CsPbI$_3$:EuCl$_3$ yellow δ-phase.*

*CsPbI$_3$:EuI$_2$ black γ-phase*

|  | E$_g$ | E$_1$ | E$_2$ | E$_3$ |
|---|---|---|---|---|
| *E (eV)* | 1.79 | 2.56 | 3.36 | 4.16 |
| *A (eV)* | 0.81 | 3.32 | 4.22 | 1.63 |
| *Γ (eV)* | 0.09 | 0.53 | 0.68 | 1.29 |
| *Φ (rad)* | -47.12 | 4.79 | 18.76 | -101.76 |

*Table A1.3 Critical point energy (E), broadening (Γ), amplitude (A), and phase (Φ) as extracted from fitting of Eq. 1.2 in the main text for the CsPbI$_3$:EuI$_2$ black γ-phase.*

*CsPbI$_3$:EuI$_2$ yellow δ-phase*

|  | E$_g$ | E$_1$ | E$_2$ |
|---|---|---|---|
| *E (eV)* | 2.92 | 3.32 | 4.12 |
| *A (eV)* | 4.02 | 2.84 | 3.67 |
| *Γ (eV)* | 0.11 | 0.30 | 1.19 |
| *Φ (rad)* | 15.38 | -42.15 | 7.01 |

*Table A1.4 Critical point energy (E), broadening (Γ), amplitude (A), and phase (Φ) as extracted from fitting of Eq. 1.2 in the main text for the CsPbI$_3$:EuI$_2$ yellow δ-phase.*
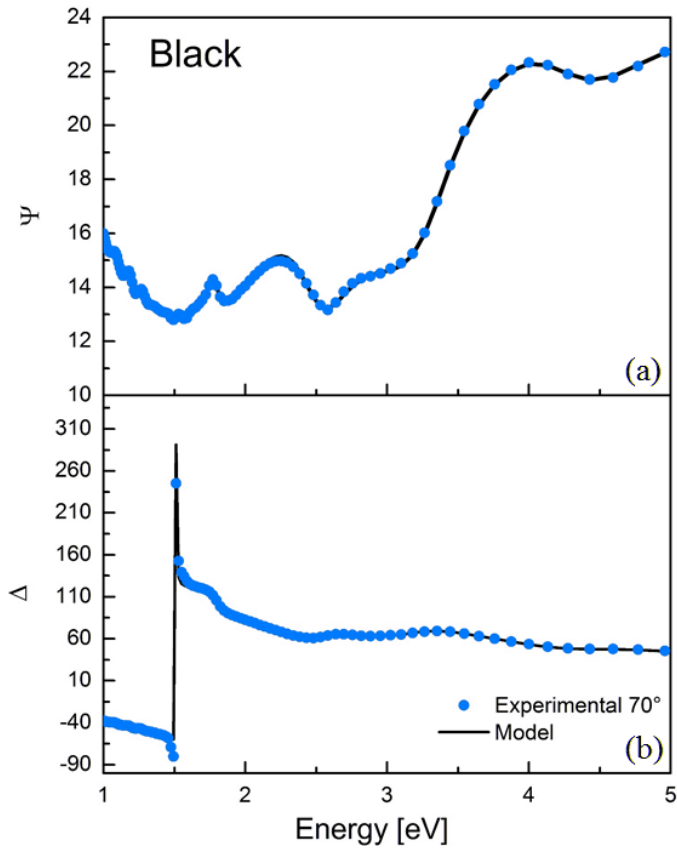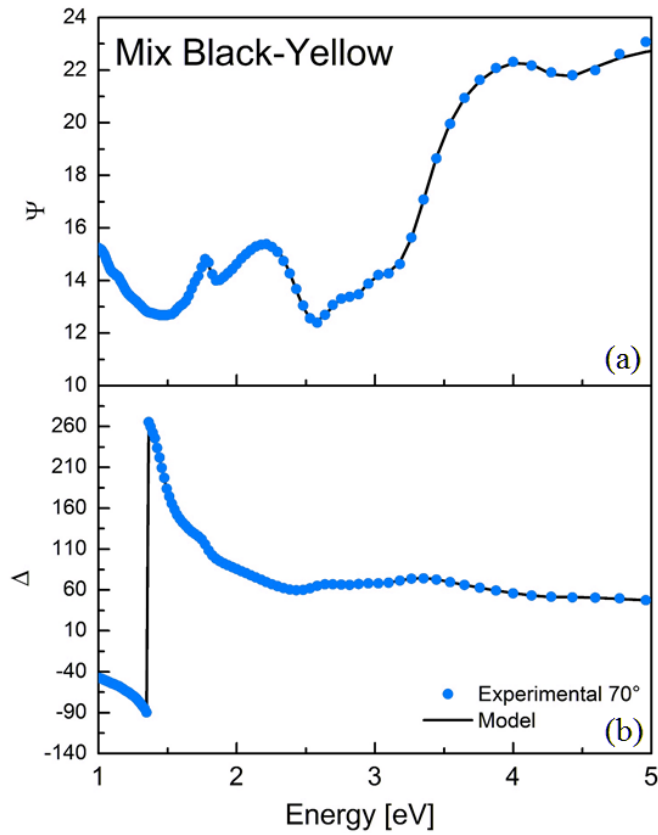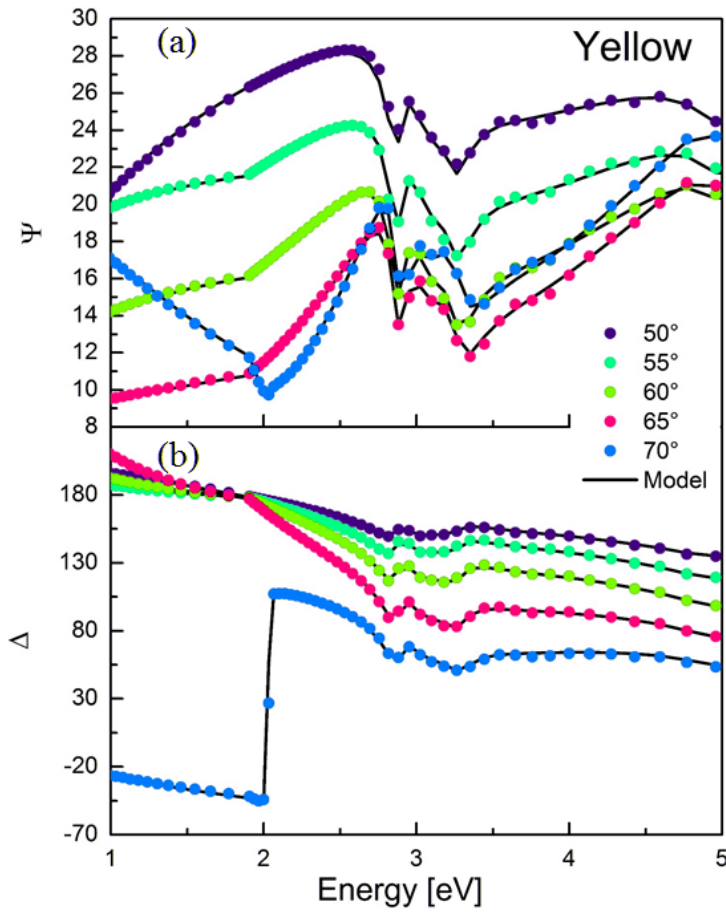
*Figure A1.3 Experimental Ψ (a) and Δ (b) (red dots) and optical model based on multiple Critical Points Parabolic Band (CPPB) oscillators (black line) at the beginning of the experiment when the film is totally black. The measurements have been collected using an over pressurized $N_2$ filled chamber which prevents the degradation of perovskite. (Ref. [48]. Creative Commons License CC BY 4.0[44])*

*Figure A1.4 Experimental Ψ (a) and Δ (b) (red dots) and optical model based on multiple Critical Points Parabolic Band (CPPB) oscillators (black line) during the transition from black to yellow phase. (Ref. [48]. Creative Commons License CC BY 4.0[44])*

*Figure A1.5 Experimental Ψ (a) and Δ (b) (red dots) and optical model based on multiple Critical Points Parabolic Band (CPPB) oscillators (black line) taken when the phase transition ends, and the film is totally yellow. (Ref. [48]. Creative Commons License CC BY 4.0[44])*
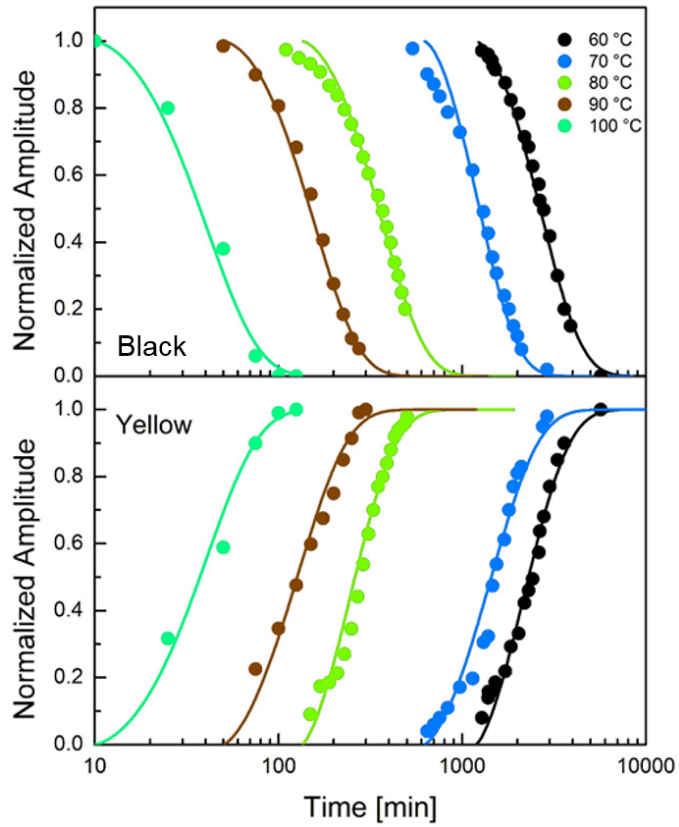
*Figure A1.6 Trend over time of the normalized amplitude at $E_g$ CP black (a) and $E_g$ CP yellow (b) for CsPbI$_3$:EuI$_2$ samples at five different temperatures of ageing (60-70-80-90-100 °C). (Ref. [48]. Creative Commons License CC BY 4.0[44])*
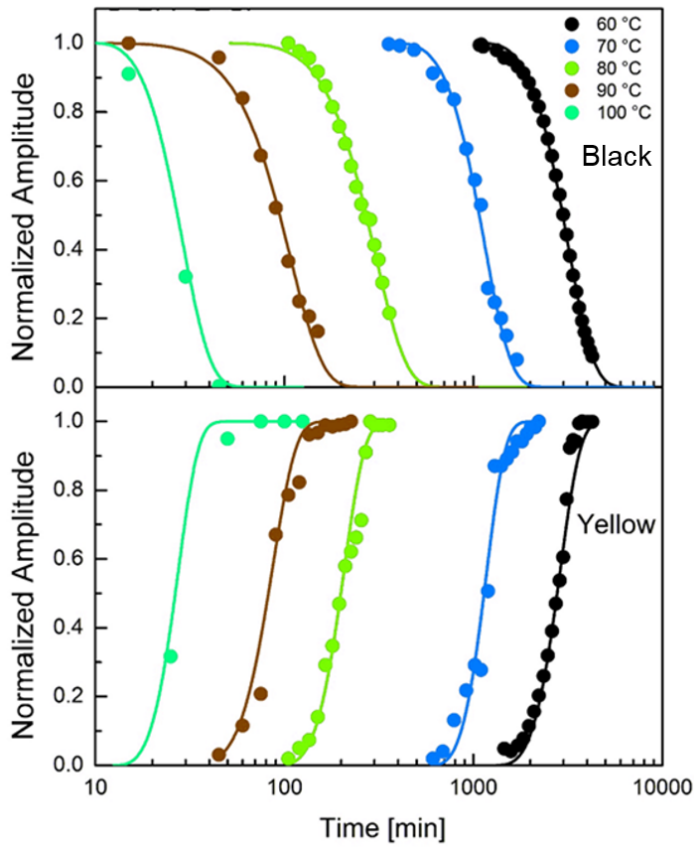
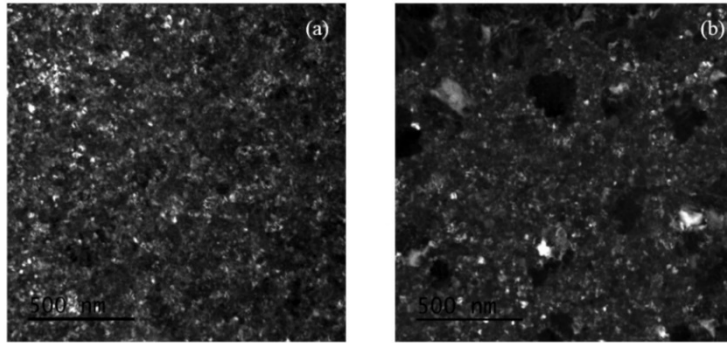*Figure A1.7 Trend over time of the normalized amplitude at $E_g$ CP black (a) and $E_g$ CP yellow (b) for $CsPbI_3$:$EuCl_3$ samples at five different temperatures of ageing (60-70-80-90-100 °C). (Ref. [48]. Creative Commons License CC BY 4.0[44])*

*Figure A1.8 Two different regions of a γ-phase sample after 75 min annealing at 80 °C: (a) not irradiated by the electron beam and (b) irradiated by the electron beam for reference acquisition before annealing. Additional nucleation and growth of the δ-phase is induced by the e-beam irradiation and indeed a proper protocol must be applied by analysing fresh areas after each in-situ annealing (see detailed description in the main paper). (Ref. [48]. Creative Commons License CC BY 4.0[44]).*
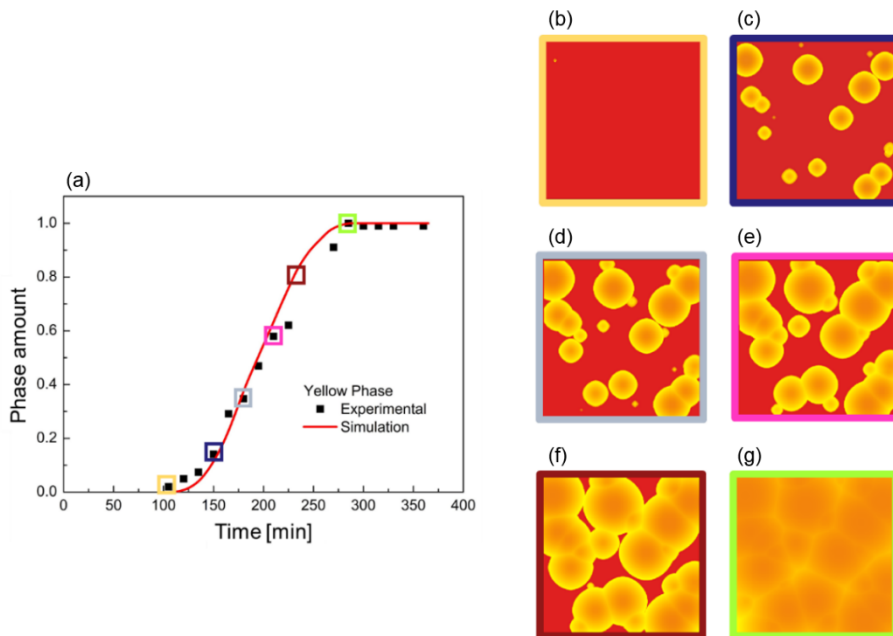


*Figure A1.9 (a) Simulation by Fast Marching method of the yellow grain nucleation and growth at the expenses black phase in terms of the percentage of yellow phase amount in the film (red line) combined with SE experimental values (black square). (b)-(c)-(d)-(e)-(f)-(g) Graphical representation of the yellow grains nucleation and growth obtained by "Fast Marching" simulation at different time of phase transition corresponding to the coloured square in (a). The red background represents the γ-phase while the yellow grains are in the δ– phase. (Ref. [48]. Creative Commons License CC BY 4.0[44]).*

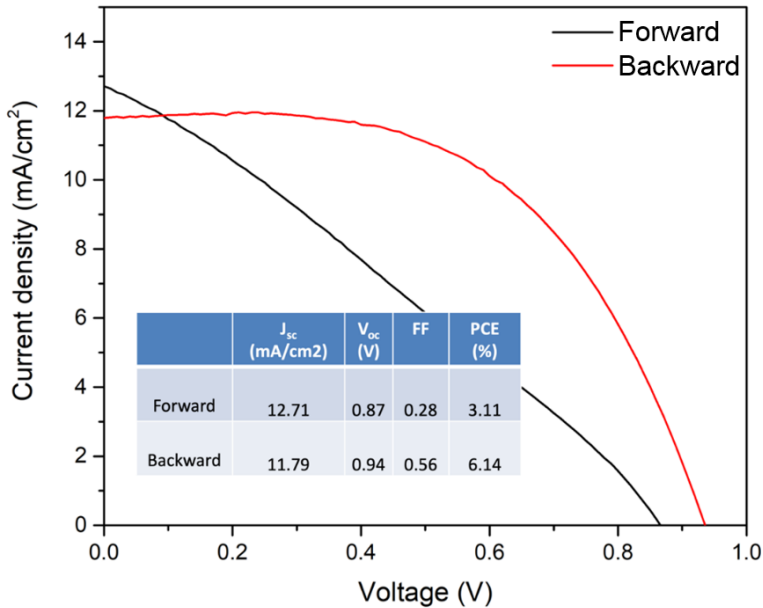| | $J_{sc}$ (mA/cm2) | $V_{oc}$ (V) | FF | PCE (%) |
|---|---|---|---|---|
| Forward | 12.71 | 0.87 | 0.28 | 3.11 |
| Backward | 11.79 | 0.94 | 0.56 | 6.14 |

*Figure A1.10 Representative J-V Curve in a solar cell architecture made of FTO/TiO2/PSK/spiro-OMeTAD/Au with γ-CsPbI₃:EuCl₃ prepared at 80 °C. (Ref. [48]. Creative Commons License CC BY 4.0[44])*

| | $J_{SC}$ (mA/cm²) | $V_{OC}$ (V) | FF | PCE (%) |
|---|---|---|---|---|
| CsPbI₃:EuCl₃ | 11.79 | 0.94 | 0.56 | 6.14 |
| CsPbI₃:EuI₂ | 8.76 | 0.93 | 0.54 | 4.40 |

*Table A1.5 Photovoltaic parameters extracted from reverse scan of the representative solar cells using CsPbI₃:EuCl₃ and CsPbI₃:EuI₂ as active layer (architecture made of FTO/TiO2/PSK/spiro-OMeTAD/Au).*

# References

[1] E. Smecca et al. *J. Mater. Chem. A* 2021, 9, 16456-16469

[2] Z. Li et al. *Nano Energy* 2020, 71, 104634

[3] A. J. Bett et al. *Energy Proc.* 2017, 124, 567

[4] T. Leijtens et al. *Nat Energy* 2018, 3, 828

[5] Q. Wali et al. *Renew. Sustain. Energy Rev.* 2018, 84, 89

[6] Y. Wang et al. *Science* 2019, 365, 591

[7] T. Leijtens et al. *Nat. Energy* 2018, 3, 828

[8] Q. Wali *Renew. Sust. Energ. Rev.* 2018, 84, 89

[9] https://www.nrel.gov/pv/cell-efficiency.html (last access: 20/07/2022)

[10] B. Zhao et al. *J. Am. Chem. Soc.* 2018, 140, 11716

[11] Q. Ye et al. *Sci. China Chem.* 2019, 62, 7

[12] P. Becker et al. *Adv. Energy Mater.* **2019**, 9, 1900555

[13] R. J. Sutton, et al. *ACS Energy Lett.* 2018, 3, 1787

[14] Y. Fu et al. *Chem. Mater.* 2017, 29, 8385

[15] T. Zhang et al. *Sci Adv* 2017, 3, 1700841

[16] Q. Wang et al. *Joule* 2017, 1, 371

[17] Y. Guo et al. *Sol. RRL* 2020, 4, 2000380

[18] F. Haque et al. *ACS Omega* 2018, 3, 11937

[19] T. Wu et al. *Adv.Mater.* 2019, 31, 1900605

[20] P. Wang et al. *Nat. Commun.* 2018, 9, 2225

[21] B. Li et al. *Nat. Commun.* 2018, 9, 1076

[22] Z. Li et al. *Chem. Mater.* 2016, 28, 284

[23] R. J. Sutton et al. *Adv. Energy Mater.* 2016, 6, 1502458

[24] Y. Fu et al. *Chem. Mater.* 2017, 29, 8385

[25] A. K. Jena et al. *Chem. Rev.* 2019, 119, 3036

[26] J. A. Steele et al. *Science* 2019, 365, 679

[27] R.J. Sutton et al. *ACS Energy Lett.* 2018, 3,1787

[28] P. Luo *J Phys Chem Lett* 2016, 7, 3603

[29] Y. Wang et al. *J Am Chem Soc* 2018, 140, 12345

[30] T. Zhang et al. *Sci. Adv.* 2017, 3, 1700841

[31] Q. Wang et al. *Joule* 2017, 1, 371

[32] C.Yi C et al. *Nat Commun* 2020, 11, 4736

[33] Y. Zhang et al. *Organic Electronics* 2020, 87, 105940

[34] F. Yang et al. *Angew Chem Int Ed* 2018, 57, 12745

[35] Y. Hu et al. *ACS Energy Lett* 2017, 2, 2219

[36] J. Zhang et al. *Mater. Res. Express* 2019, 6, 105529

[37] C.F.J. Lau et al. *ACS Energy Lett 2017,* 2, 2319

[38] Murugadoss G, Thangamuthu R, Kumar M R, Ravishankar R 2019 *Micro & Nano Letters* **14** 1385

[39] H. Zhao et al. *Adv. Funct. Mater.* 2019, 29, 1808986

[40] A. Alberti et al. *Adv. Energy Sustainability Res.* 2021, 2, 2100091

[41] A.K. Jena et al. *Chem. Mater.* 2018, 30, 66684

[42] M. Fox *Optical Properties of Solids* 2010 (Oxford University Press, Great Clarendon Street, Oxford OX2 6DP)

[43] B. Subedi et al. *Sol. Energy Mater Sol. Cells* 2018, 188, 228

[44] https://creativecommons.org/licenses/by/4.0/

[45] A. Swarnkar et al. *Science* 2016, 354, 92

[46] K.M. Sim et al. *Laser Photonics Rev* 2018, 12 1700209

[47] W. Xiang et al. *Joule* 2019, 3, 205

[48] S. Valastro et al. *J. Phys. Mater.* 2021, 4, 034011

[49] S. Valastro et al. *Solar RRL* 2022, 6, 2200008

[50] J.A. Steele et al. *Science* 2019, 365, 679

[51] A. Marronnier et al. *ACS Nano* 2018, 12, 3477

[52] D. B. Straus et al. *J. Am. Chem. Soc.* 2019, *29*, 11435

[53] M. Cardona. Solid State Physics: Advances in Research and Applications. Modulation spectroscopy. Supplement 11, 1969 (New York: Academic)

[54] M. Cardona and P. Yu. Fundamentals of semiconductors, Physics and materials properties 2010 (Springer-Verlag)

[55] A. Alberti et al. *Adv. Energy Mater.* 2019, 9, 1803450

[56] I. Deretzis et al. *J. Phys. Chem. Lett*. 2018, 9, 3000

[57] P. Lautenschlager et al. *Phys. Rev. B* 1987, 35, 9174

[58] U. Fano. *Phys. Rev.* 1961, 124, 1866

[59] Y. Jiang et al. *Appl. Phys.Lett.* 2016, 108, 061905.

[60] G. Mannino et al. *J. Phys. Chem. Lett.* 2020, 11, 2490

[61] G. Mannino et al. *J. Phys. Chem. C* 2021, 125, 4938

62 Z. Yao et al. *J. Mater. Chem. A* 2021, 9, 11124

[63] G. Mannino et al. *J. Phys. Chem.* C 2017, 121, 7703

[64] M. Avrami *J. Chem. Phys* 1939, 7, 1103

[65] M. *Avrami J. Chem. Phys* 1940, 8, 212

[66] M. *Avrami J. Chem. Phys* 1941, 9, 177

[67] M. M. Moghadam et al. *Scr. Mater.* 2016, 124, 164

[68] E. L. Pang et al. *J. Appl. Phys.*2015, 117, 175304

[69] A. Alberti et al. *Appl. Phys. Lett.* 2007, 90, 053507

[70] C. G. Bischak et al. *Matter* 2020, 3, 534

[71] K. Suchan et al. *J. Mater. Chem. A* 2020, 8,10439

[72] B. Wang et al. *Sci Rep* 2015, 5, 10557

[73] A. Alberti et al. *Nat. Commun.* 2019, 10, 2196

[74] J. A. Sethian et al. *Geophysics* 1999, 64, 516

[75] G. Garozzo et al. *Comp. Mat. Sci.* 2002, 24, 246

# Chapter 2: Stability of HTL-free carbon-based PSCs

*In this chapter, sustainability is viewed from the perspective of new approaches to improve performances and stability of HTL-free carbon-based PSCs, specifically preserving the carbon/perovskite interface. HTL-free carbon-based PSCs are intrinsically sustainable in avoiding organic hole transporting layers that are chemically produced and are costly.*

*The data shown in this chapter were published in Frontiers in Chemistry (Valastro et al. 2020, 8, 200) and Energies (Valastro et al. 2020, 13 (15), 3953).*

## 2.1    HTL-free carbon-based PSCs: potentialities and issues

Device engineering has a crucial part in the reliability and integrability of the PSC technologies. For that, device engineering deserves special consideration. In direct architecture (TCO/ETL/perovskite/HTL/CE), researchers focus particular attention on the choice of the HTL and of the CE, playing a pivotal role in the performances and stability of the devices. Specifically, the interfacial degradation, occurring at the CE/HTL and the HTL/perovskite interface, is the main reason for the decrease in PSC efficiency over time, while degradation of the core of the perovskite layer is found to have a minor effect [1]. As a matter of fact, most of the efficient and highly expensive organic HTMs (e.g. Spiro-OMeTAD) are operationally unstable and are inclined to mediate migration of halide and metal ions of noble metal counter-electrodes which are conventionally used (e.g. Au, Ag and Al) [2,3,4.] Among the non-conventional proposed architectures, hole-transporting-layer-free Carbon-based PSCs (HTL-Free C-PSCs) are highly competitive due to their superior long-term stability and low cost [5,6,7,8] that compensate the lack of carrier selectivity with respect to the application of a Hole Transporting Material.

Carbon-based top contacts for HTL-Free PSCs are realized using carbon pastes (mix of graphite flakes, carbon black, curing resin and solvent) deposited directly on the perovskite layer by different methods: doctor-blading, ink-jet printing, hot press transfer etc. [9,10]. These methods are up-scalable and low-cost, thus providing a feasible industrially appealing solution for large area devices. Furthermore, the structural stability and the hydrophobic character of the carbon electrode, preserving the underneath perovskite from the environmental humidity, make it a promising back-contact for commercialization of PSCs. Recently, to improve the efficiency of HTL-free devices, various p-type doping approaches have been investigated in C-electrodes to regulate the Fermi-level of the carbon electrode and to make it more

selective for holes extraction[6]. A different strategy, ideated by Zhou et al.[11], consists of substituting the state-of-art ETL used in HTL-free carbon based devices, namely $TiO_2$, with solution processed hexamethonium bromide (HMB)-doped $C_{60}$ reaching a power conversion efficiency (PCE) of over 16%, the highest value in literature for this architecture of devices. In 2019, in the context of up-scalable approaches, Barichello et al. [12] designed a fully printable HTL-free C-PSC using a home-made mesoporous alumina ($Al_2O_3$) ink, achieving a maximum efficiency of 9.13% and reaching 10.66% with a water treatment of substrate before perovskite deposition. More recently, it has been predicted by theoretical calculations that an efficiency as high as 19.72%[13] can be achieved for HTL-free carbon-based PSCs by embedding $Ag/SiO_2$ plasmonic nanoparticles in the proximity of the perovskite-compact $TiO_2$ interface. However, the optimization of the carbon deposition method for PSCs with a long durability has been rarely explored in the literature.

In order to improve long-term stability of the electrical performance in PSCs, the perovskite interface with the carbon electrode must be preserved from degradation [14,15,16,17,18.] As a matter of fact, PSCs with carbon contacts deposited by the doctor-blading (DB) method and successive annealing show a deterioration path of the electrical performance during time, primarily due to a solvent-mediated interaction of the C-electrode with the perovskite surface[19].

In this chapter, we explore two different strategies to achieve the preservation of C/PSK interface: 1) a solvent-free carbon deposition method based on hot-pressing a free-standing dried C-Al foil directly on the perovskite layer (HP-PSC), 2) a vacuum-curing treatment on the device with carbon electrode deposited by doctor blading method (DBv-PSC).

## 2.2 Carbon/MAPbI₃ interface preservation: a solvent-free method

Herein, we evaluate the durability over months of HTL-free carbon-based PSCs, with carbon layer fabricated on MAPbI₃ layers with solvent-free hot-press transfer method compared to conventional doctor-blading method, by analysing the evolution of the photovoltaic parameters in devices. The hot-press-transfer is done at 100 °C and at a pressure of 0.1 MPa, a compromise with respect to what already explored in the literature[19,20]. The procedure fabrication is explained in detail in the Methods section. This systematic investigation has highlighted a viable approach to avoid the deleterious action over time of the solvent present in commercially available C-based pastes. The two methods used to fabricate carbon electrodes by doctor-blading and hot-pressing on twin MAPbI₃/TiO₂/FTO samples are shown in Figures 2.1a-b, respectively. Composition inside and outside the contact regions was unfolded by X-ray Diffraction that probed the layered structure of the entire device architecture (Figures 2.1c-d). During the analysis, the X-ray beam was scanned through the contact

at the fixed Bragg-angle of MAPbI$_3$ (main peak at 2θ=14.1°), PbI$_2$ (main peak at 2θ=12.7°) or Graphite (main peak at 2θ=26.55°). In both samples, PbI$_2$ is an almost negligeable solid byproduct that can be left as residue from the preparation procedure. On their basis, the compositional line profiles of MAPbI$_3$, PbI$_2$ and graphite are traced in Figures 2.1e-f. The graphite peak, as the main component in the commerical paste, was used to draw the contact profile. Through the contact, the intensity ratio between MAPbI$_3$ and PbI$_2$ lies in the range 4.6-6.2, with the relatively small amount of PbI$_2$ not sensibly changing outside the contact area. A similar scenario is indeed depicted in the two explored cases meaning that no macroscopic degradation of the perovskite layer occurred after contact formation. This testifies that both methods are viable.
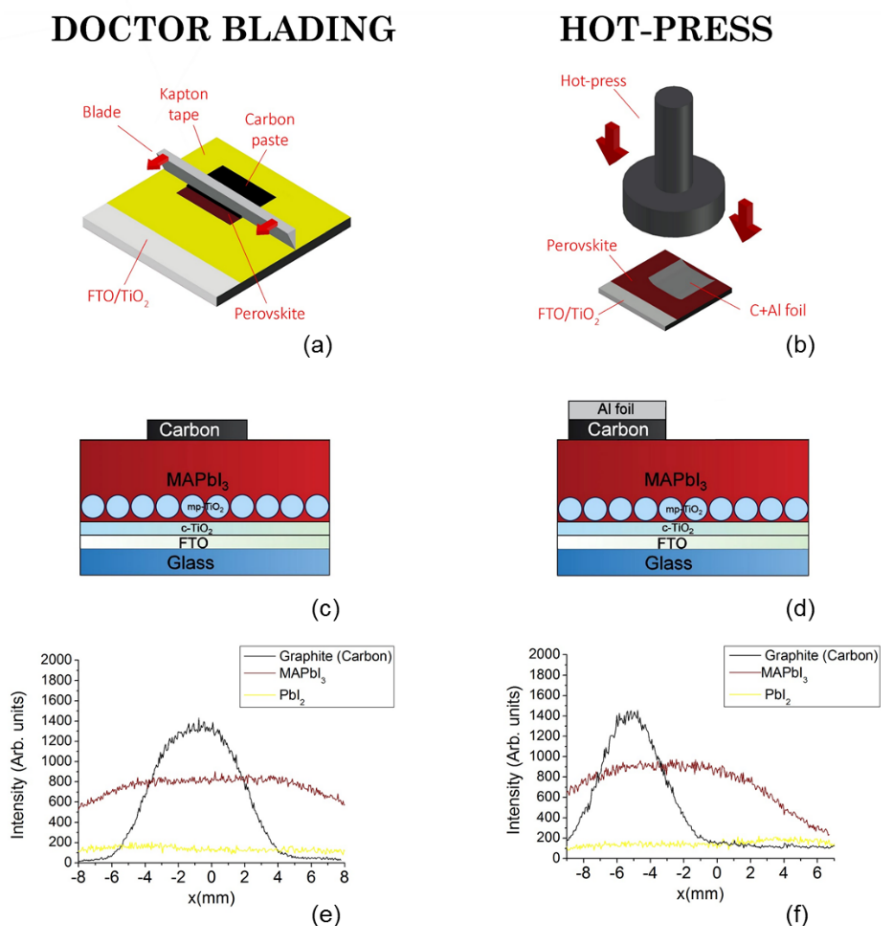


*Figure 2.1 Doctor blading and hot press transfer methods for carbon electrode fabrication and compositional line-profiles. (a) Schematic illustrating doctor blading and (b) hot press methods. (c-d) Two devices architectures. (e-f) Line profiles taken by XRD through the contact regions. (Ref. [32]. Creative Commons License CC BY 4.0 [21])*

Figures 2.2a-b show the electrical response in as prepared devices (day 1) under 1 sun illumination. In particular, the PSC with the carbon electrode made by the doctor blading method (DB-PSC) shows better performance than the PSC with the carbon electrode fabricated by the hot-press method (HP-PSC). We firslty argue a minor role of the Al foil used in the HP-PSCs (notice the slope at the $V_{oc}$). The best cell works at an efficiency of 7.94% with short-circuit photocurrent density ($J_{sc}$) = 14.73 mA/cm$^2$, open-circuit voltage ($V_{oc}$) = 1.01 V, and fill factor (FF) = 53.35%. These values match quite well with the data reported in the literature for similar device architectures and commercial C-based pastes, as summarised in ref.[5]. On the other hand, the starting efficiency of the HP-PSC is 1% less than the reference DB-PSC (6.87% vs. 7.94%). The discrepancy is verified over a statistics of 4-5 devices, being indeed not ascribable to a perovskite layer variability. This finding provides the first indication of a better initial contact between the DB-carbon electrode and the perovskite layer immediately after its production. It is indeed likely that, via DB, a chemical-assisted coupling of the C-electrode with the perovskite is nicely promoted by the solvent, as opposed to the case of Hot-Pressing the C+Al-foil wherein the film is induced to a structural coupling by heat and pressure from the C-side. In countertrend, the short circuit current value is instead higher in HP-PSCs and this likely helps the performance improvement over time discussed hereafter.

In order to evaluate how stable are the device performances, DB-PSC and HP-PSC were measured at regular intervals over 1 month, under one-sun illumination and in environmental atmosphere without any encapsulation. After each measurement, the devices were stored in nitrogen atmosphere under open-circuit and dark conditions.

The J-V curves at the beginning and end of operation, together with the curves taken at day 14, testify that a recovery of the performances can be achieved by both DB-PSCs and HP-PSCs (Figures 2.2a-b). It is noteworthy that this recovery allows getting back the initial $J_{SC}$ ,$V_{OC}$ and FF values in the HP-PSCs; it is instead partial in the DB-PSCs. The structural analysis in Figures 2.2c-d demonstrates that the recovery corresponds to a slight reduction of the $PbI_2$/$MAPbI_3$ ratio of the related diffraction peaks with respect to what measured in the same samples at day 14 (lower performances). This finding can be equally interpreted as an improvement of the perovskite lattice quality during time or as a reduction of the $PbI_2$ amount (by a factor 0.6 from day 14 to day 90 in the HP-PSC) that would imply the overall mass (including the organic cations) being preserved during the cycle of operation. The measured lattice improvement cannot be fully ascribed to compositional disuniformities along the sampled area, since this would produce smaller normalized variations in the $PbI_2$/$MAPbI_3$ peak intensity ratio.

In conjunction with a recovery of the material structure that was observed in both samples, the uncomplete restoring of the photovoltaic parameters in the DB-PSC with respect to what occurs in the HP-PSCs at the end of the cycle (day 90), addresses that the C/Perovskite interface has been irreversibly modified.
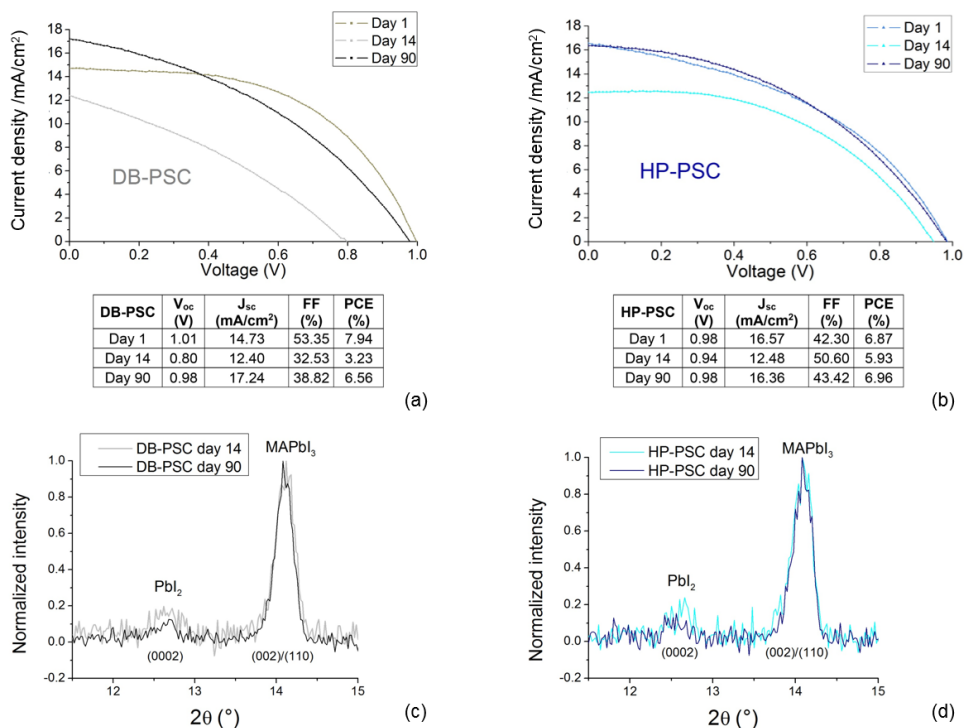


| DB-PSC | $V_{oc}$ (V) | $J_{sc}$ (mA/cm$^2$) | FF (%) | PCE (%) |
|---|---|---|---|---|
| Day 1 | 1.01 | 14.73 | 53.35 | 7.94 |
| Day 14 | 0.80 | 12.40 | 32.53 | 3.23 |
| Day 90 | 0.98 | 17.24 | 38.82 | 6.56 |

| HP-PSC | $V_{oc}$ (V) | $J_{sc}$ (mA/cm$^2$) | FF (%) | PCE (%) |
|---|---|---|---|---|
| Day 1 | 0.98 | 16.57 | 42.30 | 6.87 |
| Day 14 | 0.94 | 12.48 | 50.60 | 5.93 |
| Day 90 | 0.98 | 16.36 | 43.42 | 6.96 |

Figure 2.2 (a-b)  J-V curves and photovoltaic parameters of representative DB-PSC and HP-PSC, respectively at the beginning (day 1) and at the end (day 90) of the cycle. Data related to day 14, taken as intermediate cases, are also shown to represent the photovoltaic response during recursive operation. (c-d) XRD patterns acquired at day 14 and day 90. Material recovery is represented by the relative reduction (normalised to the MAPbI$_3$ peak maximum) of the PbI$_2$ amount after prolonged storage in nitrogen, open circuit and dark conditions. The diffraction patterns are labelled with the related Miller indexes of the exagonal (PbI$_2$) and tetragonal (MAPbI$_3$) phases. (Ref. [32]. Creative Commons License CC BY 4.0 [21])

Figure 2.3a shows the temporal trend of the PCE values collected in representative DB-PSC and HP-PSC. We notice that the efficiency of the DB-PSC has a long-lasting transient behaviour consisting of a severe reduction until day 14. This suggests the occurrence of further structural changes and/or interfacial re-arrangements in proximity of the interface between the carbon contact and the perovskite layer, which was initiated with the intermediation of the solvent of the

carbon paste at the curing temperature (120 °C). On the other hand, a significant deterioration of the perovskite bulk is not expected on the basis of our previous investigation[22]. A similar transient behaviour is observed for all the other photovoltaic parameters, namely $V_{OC}$, $J_{SC}$, and FF (Figures 2.3a). Although the nature of the solvent in the commercial paste is not specified, some hints can be drawn [20] on polarity- and steric hindrance-related effects[23] in charge separation (e.g. by charge screening) and indeed in defect generation (e.g. iodide charged species) contributing to local structural changes. Provided the overall mass is preserved inside the material, a recovery of the performances is feasible by a structural rearrangment. At the structural side, the diffraction pattern in figure 2.2c does not show any dramatic degradation of the perovskite layer under the contact after 14 days of operation. From day 14 to day 30, the device shows deterioration/recovery pathways and the PCE consequently fluctuates in the range 3-3.5%.

HP-PSCs show a different behaviour. As a first evidence, the device does not exhibit a marked transient in the PCE values after intial operation (Figure 2.3a). Moreover, since day 1, a path of deterioration and recovery is immediately initiated. In particular, the PCE values fluctuate in the range 5-6%, which is significantly above the one measured on the DB-PSC (fluctuating in the range 2.5-3.5%). Moreover, a medium-term quasi-full recovery of the device performances, not detected in DB-PSCs, is even achieved if the storage time is long enough (e.g. 5 days). This effect is shown in Figure 2.3a between day 22 and day 26. It is finally noteworthy that storing the HP-PSC device without break for 60 days in nitrogen atmosphere under open-circuit and dark conditions (at day 90) allows a full recovery of the efficiency (6.96 %) and of all the other photovoltaic parameters ($V_{OC}$, $J_{SC}$, FF). This is clearly stated by figures 2.3b-d.

On the other hand, the DB-PSC (figure 2.3a) at day 90 has only a partial recovery of the efficiency (6.56 %) with respect to the value recorded at day 1 (7.94%). The specific behaviour of $V_{OC}$ , $J_{SC}$ and FF (figure 2.3a-c) over time frames that a crucial role is played by the FF with its link to the carrier extraction and transport at the interfaces.

Although in a different scalebar, a deterioration/recovery behaviour is feasible on both kinds of devices during operation. This is a phenomenon likely linked to 1) migration of ions in the perovskite layer under illumination and electric field (partially reversible), 2) defects formation under operation and self-curing [24] of the perovskite in absence of electric field and under dark condition, 3) healing action by nitrogen[14,16] on the perovskite and at the perovskite/carbon interface.

In this respect, the cross-correlation of data suggests that the release of solvent from the carbon paste before being in touch with the perovskite layer results in preserving the perovskite/carbon interface from irreversible changes. On the other hand, the partial reversibility of the DB-PSC performances can be linked to a permanent modification of the interface that is not fully recoverable during time. Above the full recovery of the HP-DSC, a further improvement of the cell efficiency is expected by engineering the contact[25] such to reduce the series resistance and increase contact selectivity. This is expected to primarily impact on the fill factor of the solar cells.
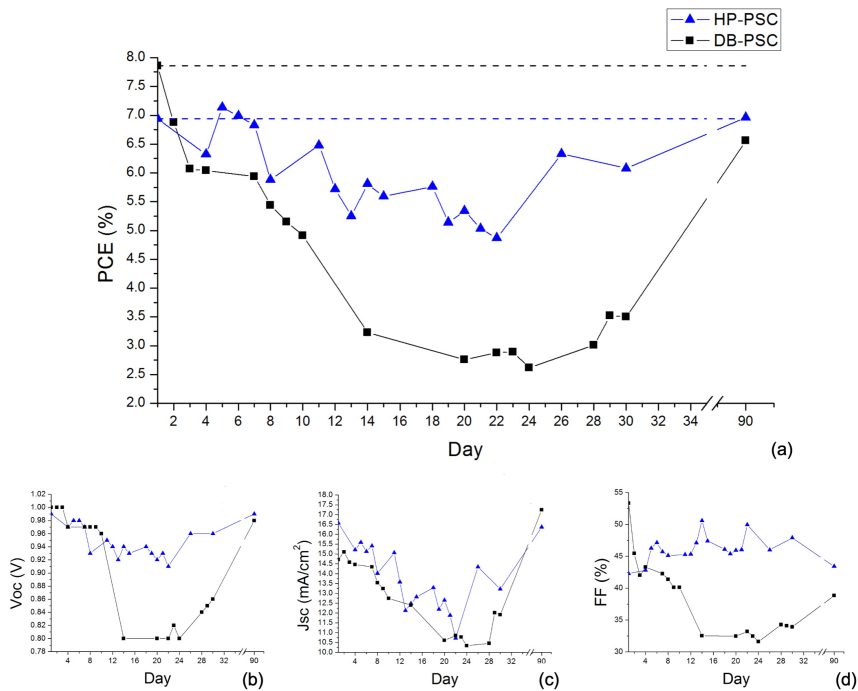


*Figure 2.3 Temporal trend of the PCE values for representative DB-PSC and HP-PSC (a). In both cases a recovery of the starting performances can be noticed, which is fully achieved for HP-PSC (b-d). (Ref. [32]. Creative Commons License CC BY 4.0 [21])*

The statistical distributions of the $V_{OC}$, $J_{SC}$, FF and PCE values for the DB-PSCs and HP-PSCs over 4-5 devices taken along the full temporal scale of the experiment (90 days), including indeed all data along the degradation-recovery path, are summarized as box plots in Figure 2.4. We notice that all the values of the electrical parameters in DB-PSCs are more widely scattered than those of HP-PSCs, resulting in larger boxes. Moreover, the median values are higher in HP-PSCs. All those findings imply that HP-PSCs exhibit 1) a better reproducibility of the top-side

electrical contact, 2) more reliable and improved performances and 3) better long-term stability.
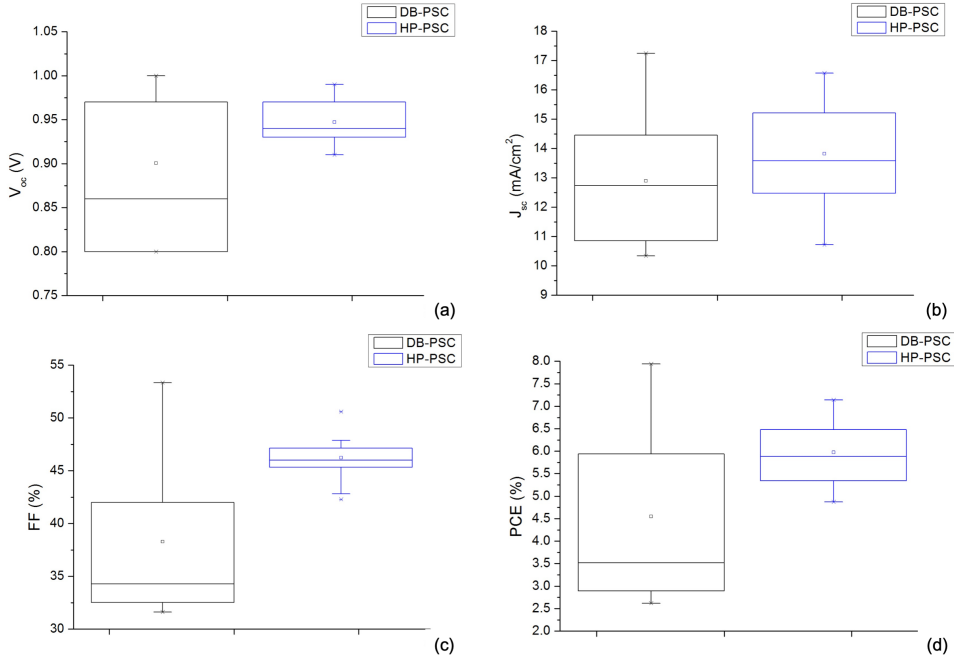


*Figure 2.4 Box plots representing data distributions of $V_{OC}$ (a), $J_{SC}$ (b), FF (c), and PCE (d) for DB-PSCs and HP-PSCs. (Ref. [32]. Creative Commons License CC BY 4.0 [21])*

## 2.3    Carbon/MAPbI₃ interface preservation: a vacuum curing treatment

Herein, we investigate a simple fabrication method for the Carbon contact consisting of doctor blading deposition ($T_{annealing}$=100 °C) and successive vacuum-curing treatment at $10^{-2}$ mbar for 24 h (samples are hereafter called DBv-PSCs). The use of vacuum-curing treatment has been recently reported in the literature for PCBM/Cu selective contacts[26], but differently from our procedure, high vacuum conditions ($10^{-6}$ mbar) have been applied for a longer time period (100 h). As a further difference, we do not remove and then re-deposit the contact layer after vacuum curing, therefore proposing a simplified fabrication procedure. Devices with carbon electrode without the vacuum curing treatment were fabricated for comparison (samples are hereafter called DB-PSCs). Both kinds of prepared devices, with and without vacuum-treatment, were taken without encapsulation for the entire

experiment. The schematic representation of the preparation process of vacuum-cured perovskite solar cells (DBv-PSCs) is shown in Figure 2.5.
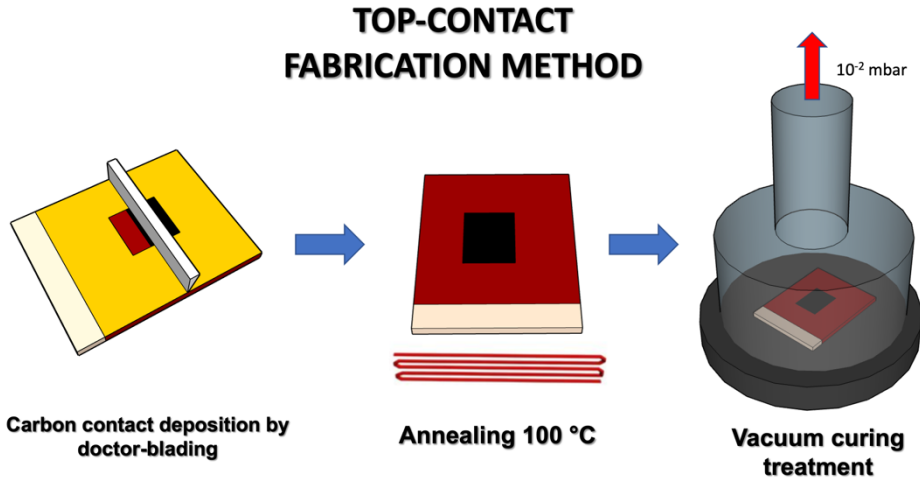


*Figure 2.5 Schematic of top-contact fabrication on a PSC and successive vacuum curing treatment. (Ref. [27]. Creative Commons License CC BY 4.0 [21])*

A systematic investigation of the photovoltaic response of representative vacuum cured devices was done by monitoring the performances for 30 days in comparison with reference no-vacuum-treated devices. Measurements were made once per day acquiring J-V characteristics under simulated sunlight.

Table A2.1 illustrates the operative parameters for solar cell characterization, the ageing conditions and the measurements made in order to follow the evolution of device performances during time. The ageing conditions are taken from protocol ISOS-D1[33], with the only difference that our cells, after the measurement in air, were kept in nitrogen instead of ambient conditions. That was a precise choice to highlight exclusively the role of the Carbon/perovskite interface without additional effects due to exposure to humidity. The storage in nitrogen environment, in fact, preserves the MAPbI$_3$ from degradation during storage[17]. X-ray diffraction analyses were performed after recursive peeling of the carbon contact up to complete removal by an adhesive tape (3M Scotch) in order to explore the entire layer structure and the eventual effect of the vacuum curing treatment. Atomic Force Microscopy (AFM) was also used to investigate the perovskite surface morphology after carbon contact removal in comparison to the one outside the contact area. Current maps were acquired by Conductive Atomic Force Microscopy (CAFM) using a Platinum (Pt) tip to extract a current of holes from the perovskite layer inside and outside the contact regions.

Figure 2.6a shows the initial performance (day 1) of a representative DBv-PSC compared to a reference device, namely a DB-PSC which was not treated in vacuum after C-deposition.

We notice that both devices start working with similar initial power conversion efficiency (PCE). The DBv-PSC exhibits an efficiency of 6.95% (6.94% for the DB-PSC) with short-circuit photocurrent density (Jsc) = 14.42 mA/cm2 (15.65 mA/cm2 for the DB-PSC), open-circuit voltage (Voc) = 0.99 V (0.96 V for the DB-PSC), and fill factor (FF) = 48.7% (46.2% for the DB-PSC), as shown in Table 2.1. Such close similarity of the PV parameters, that fall well within the statistics of the single kind of device, indicates that the vacuum treatment does not have any negative effect on the photovoltaic performances.
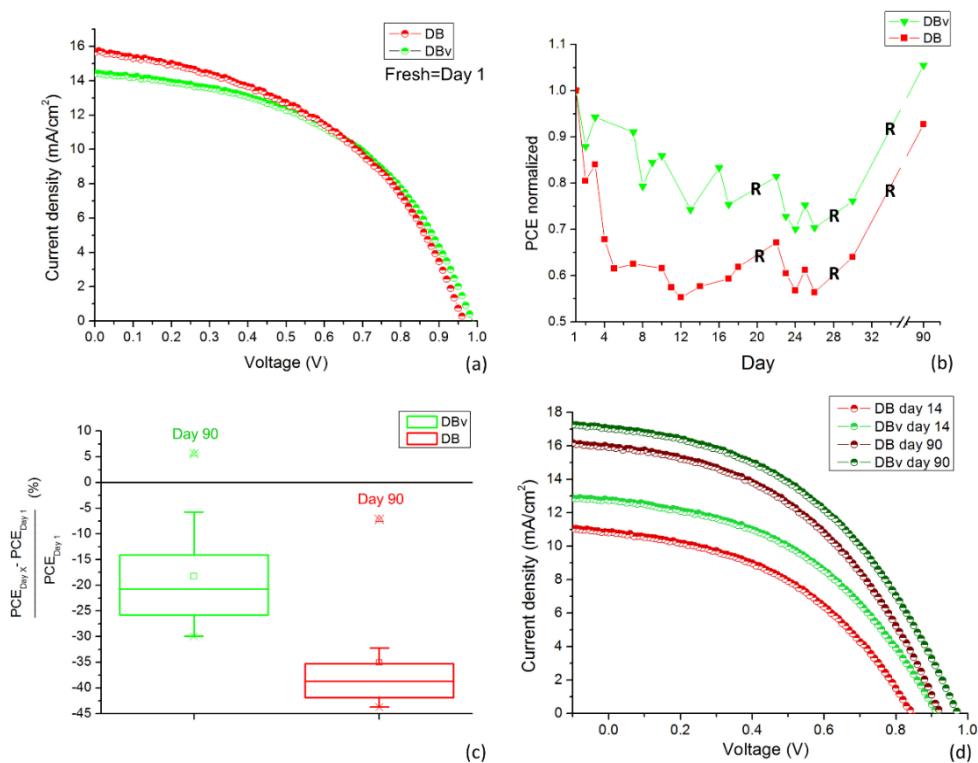


*Figure 2.6 (a) J-V curves of representative DB-PSC and DBv-PSC at day 1, i.e. with fresh devices; (b) PCE trend along 30 days and after 60 days storage in dark condition and nitrogen environment. "R" in the figure indicates the partial recovery of performance due to dark storage in nitrogen environment for a time ≥ 4 days; (c) Box plot of PCE Percent variations with respect to the value of day 1; (d) JV curves of representative DB-PSC and DBv-PSC (as in Figure a) at day 14 and day 90. Measurements were taken on the same device for each type (DB-PSC and DBv-PSC). (Ref. [27]. Creative Commons License CC BY 4.0 [21])*

| | | $V_{OC}$ (V) | $J_{SC}$ (mA/cm$^2$) | FF (%) | PCE (%) |
|---|---|---|---|---|---|
| *Day 1* | **DB-PSC** | 0.96 | 15.65 | 46.2 | 6.94 |
| | **DBv-PSC** | 0.99 | 14.42 | 48.7 | 6.95 |
| *Day 14* | **DB-PSC** | 0.85 | 10.83 | 43.52 | 4.01 |
| | **DBv-PSC** | 0.92 | 12.73 | 44.02 | 5.16 |
| *Day 90* | **DB-PSC** | 0.92 | 15.93 | 44.00 | 6.45 |
| | **DBv-PSC** | 0.97 | 17.05 | 44.38 | 7.34 |

*Table 2.1 Photovoltaic parameters of representative DB-PSC and DBv-PSC on day 1 (fresh), day 14 (worst condition) and day 90 taken on the same device for each type (DB-PSC and DBv-PSC).*

The temporal trend of the PCE normalized to the value on day 1 is shown in Figure 2.6b. Relative increase or decrease of the PCE of each device is ascribable to degradation/recovery paths. Here, relative recovery of performances occurring in a time interval ≥ 4 days of storage in dark and nitrogen environment is marked as "R".

In general, in the DB-PSC, a short-lasting performance degradation transient was observed, with a 40% PCE loss with respect to the initial value within ~5 days. From day 5 to day 30, the device shows deterioration/recovery behaviour and the PCE accordingly fluctuates in the range 55-65% of the value on day 1. On the other hand, vacuum curing impacts the long-term stability of the PSC positively, resulting in better efficiency stability over time compared to DB-PSC. In the end, the vacuum-cured PSC indeed loses in average ~20% of the initial PCE value, as also shown in the box plots in Figure 2.6c. This is similar to what we have observed in PSCs with a carbon electrode made by solvent-free hot press transfer method (HP-PSC)[32]. Moreover, contrary to the DB-PSC, the DBv-PSC does not show the degradation transient behaviour in the first days. Since day 1, it exhibits the degradation/recovery pathways similarly to what happens for HP-PSC[32].

On day 30, both kinds of devices were stored in dark conditions, with no bias applied and in a nitrogen environment. After 60 days of storage, both DB-PSC and DBv-PSC were measured to evaluate their "aged" performances. It is noteworthy that both cells have instead recovered their performances in comparison with the last run of measurements. A similar effect is reported in the previous paragraph wherein the top contacts were made without HTL, with the maximum gain achieved by avoiding solvent-perovskite interaction during contact fabrication. In this regard, doctor blading compared to the Hot-Press transfer method provides a better guarantee of adhesion to the underlying perovskite through the whole contact area and thus it is believed to be technologically more reliable.

Furthermore, as shown in Figure 2.6b, the performances of the DBv-PSC on day 90 are even better than those on day 1, with an increase of the PCE value by ~6%

(7.34% vs 6.95%), as opposite to what happens to the DB-PSC (decrease of PCE values by ~6% ). Figure 2.6c shows the distributions of percent variations of PCE from day 1 up to day 90, displayed as box-plots, with respect to the value on day 1 for the DB-PSC and the DBv-PSC. The average values, represented by the horizontal lines in the figure, are -20% and -40% for the DBv-PSC and the DB-PSC respectively, indicating a minor loss of performances for vacuum-treated devices. The values recorded in the DBv-PSC are more widely scattered than those of the DB-PSC, resulting in a larger box. This is due to better efficiency recovery in the DBv-PSC case. Finally, the outliers in Figure 2.6c present the PCE percent variations after 60 days of storage/measured on day 90. The DBv-PSC shows a surprising PCE increase by ~6% (value higher than the zero line) as opposite to the DB-PSC (~ -6%).

Figure 2.6d compares the J-V curves of the two kinds of devices on day 14 (worst condition) and day 90 (final condition). Table 2.1 summarizes the values of photovoltaic parameters (open circuit voltage, short current density, fill factor and PCE) for both DB-PSC and DBv-PSC on day 1, day 14 and day 90. A huge improvement of all photovoltaic parameters  is observed on day 90 (after 60 days of storage in dark conditions with no bias applied and in nitrogen environment) compared to values on day 14. The increase in Jsc of the vacuum-treated device is especially noteworthy (Figure 2.6a).

The observed electrical phenomenon likely arises from improved perovskite lattice structure that could also involve the interface with the contacting material. However, the extra-gain introduced by the vacuum treatment indicates that the self-healing of the perovskite core[28], which would occur in both kinds of device, is not an exhaustive explanation. To understand the origin, the carbon contacts were removed by a process of progressive peeling using a sticky tape (Figure 2.7a) on day 90 after the last J-V measurements. The structural, morphological and electrical changes of the exposed $MAPbI_3$ surface were analysed. The composition inside the contact regions was unfolded by X-ray diffraction, as shown in Figure 2.7b. The measurements reveal the same amount of $MAPbI_3$ (main peak at $2\theta = 14.1°$) and almost negligible traces of $PbI_2$ (main peak at $2\theta = 12.7°$) in both kinds of devices, suggesting no irreversible macroscopic degradation in the perovskite layer under the carbon contact. Our finding indeed moves the focus towards the carbon/perovskite interface. This interface could be pivotal in improving the stability of the device, in agreement with the recent literature on other cell architectures[29,30,31].

We have thus investigated the morphology of the MAPbI$_3$ surface by Atomic Force Microscopy (AFM) measurements in different regions, namely inside and outside the contact area after peeling. The morphological analyses on representative devices show negligible differences between the DBv-PSC and the DB-PSC (Figure 2.7c-d-e-f) in both regions, with no evident changes in grain size and roughness. On this basis, we conclude that no significant morphological changes have occurred after deposition of the carbon contact by the doctor-blading method, during vacuum curing and after the contact peeling.
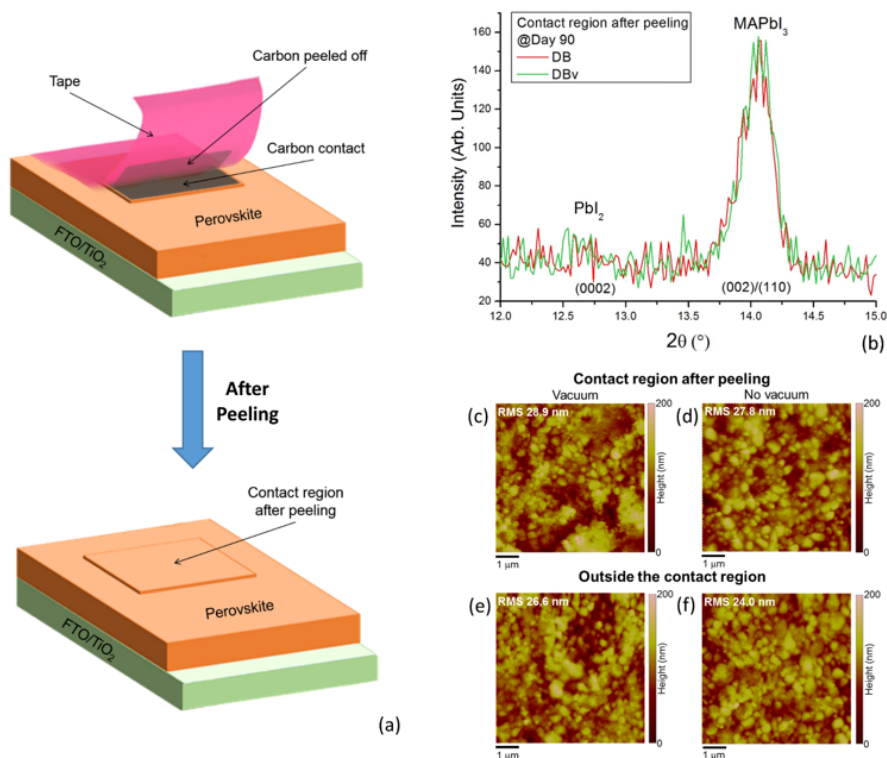


*Figure 2.7 (a) Schematic of the carbon contact removal by peeling; (b) XRD patterns of representative DB-PSC and DBv-PSC acquired at day 90 inside the contact region after peelings. The diffraction patterns are labelled with the related Miller indexes of the hexagonal (PbI$_2$) and tetragonal (MAPbI$_3$) phases. AFM morphologies inside (c)-(d) and outside (e)-(f) the contact region after peeling in DB-PSC and DBv-PSC. (Ref. [27]. Creative Commons License CC BY 4.0 [21])*

Surface morphology and electrical behaviour are not necessarily correlated. To go deeper into the process of carrier extraction from the perovskite surface, local electrical analyses using Conductive Atomic Force Microscopy (CAFM) were performed. CAFM was applied to explore the electrical behaviour of the MAPbI$_3$ surface at the nanometre scale both inside and outside the contact region after peeling.

Local current mapping of MAPbI$_3$ surfaces, as illustrated in Figure 2.8a, was collected by CAFM using a Pt-coated Silicon tip. By applying a positive bias to the electrode, holes are extracted owing to a proper band position of Pt with respect to MAPbI$_3$. All the measurements have been performed under dark conditions.

From the CAFM maps, it is clear that higher currents flow-out through the Pt-tip in the contact region of the DBv-PSC (Figure 4b) while the DB-PSC (Figure 2.8c) counterpart shows low current flow. The more efficient hole extraction from the perovskite surface inside the contact region (after C-contact peeling) in vacuum-treated devices is confirmed by the local I-V measurements shown in Figure 2.8d. From the shape of the electrical curve, we notice that the rectifying behaviour of the tip-perovskite interface and the higher collected current at a fixed voltage in the forward scan (V>0), compared to the reference DB-PSC. Both devices in the area outside the peeled C-contact region exhibit similar electrical response and are less performing than the perovskite surface after peeling in the vacuum-treated devices.
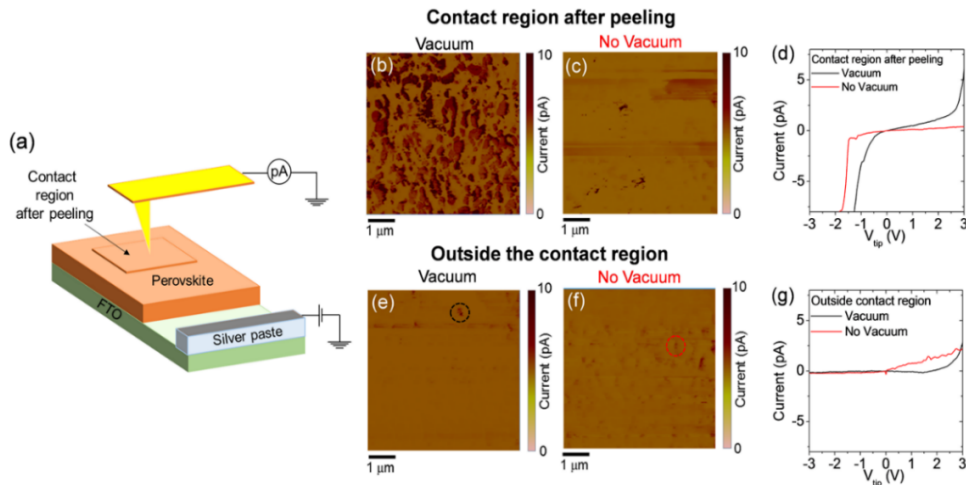


*Figure 2.8 Schematic of CAFM measurements (a); current map in the region of the contact after peeling and outside the contact region for DBv-PSC (b), (e) and for DB-PSC (c), (f), respectively. The maps are taken at a fixed voltage of 3 V. Local I-V measurements for DBv-PSC and DB-PSC performed inside the contact region (d) and outside the contact region in the areas indicated respectively by black and red circles (g). (Ref. [27]. Creative Commons License CC BY 4.0 [21])*

The positive role of the vacuum treatment was indeed clearly stated by the improved quality of the perovskite surface under the C-contact to release holes. We argue this effect to be partially linked to a positive action of the vacuum to further remove residual solvent from the contact after doctor blading deposition. This agrees with the previous findings wherein the solvent was prevented to interact with the perovskite layer by applying a hot-press method[32]. Additional positive effects linked

to carbon interacting and stabilising the perovskite surface through modifications at the atomic scale cannot be excluded.

## Methods

*MAPbI₃ synthesis and deposition:* a 450nm-thick MAPbI$_3$ layer was deposited on a 90nm-thick meso-porous-TiO$_2$/c- TiO$_2$/FTO by solution processing. Before preparation of perovskite film, a perovskite precursor solution and the substrates were warmed at 70 °C. A 1.5 M solution of methylammonium iodide (MAI) and PbI$_2$ (1 : 1 in mol) in *N,N*-dimethylformamide (DMF) and dimethylsulfoxide (DMSO) (4:1 v/v) was poured onto the TiO$_2$ mesoporous substrate and spin-coated (kept for 60 sec, 5000 rpm for 30 sec with chlorobenzene dripping). The as prepared film was pot-roast vapour annealing (PR-VA) treated at 100 °C for 10 min on a hot plate. The resulting perovskite layer is compact and uniform. The size of the grains is in the range 400-800nm

*C-based top electrode deposition:* in the hot-press transfer method, glass substrate was coated with the commercial carbon paste by doctor-blading, forming a wet carbon film. Then it was soaked into ethanol for a solvent-exchange. After that, the carbon film was peeled off from the glass substrate and, differently from ref. [19], dried at RT on an aluminium foil. As a result, a C+Al free standing electrode (A=0.25 cm$^2$) was formed and directly hot pressed onto the perovskite layer under the pressure of 0.1 MPa at 100 °C for 40 minutes. In the doctor blading method, a commercial carbon paste (Dyenamo DN-CP01) was coated onto the perovskite layer with a blade. A kapton tape frame is used to define area (A=0.25 cm$^2$) and thickness (30 µm) of the top electrode. Then, the PSC with the wet carbon film was dried at 120 °C for 15 minutes (according to the Dyenamo datasheet) in nitrogen atmosphere to remove the solvent and to promote the curing of the paste. Trials by using 100 °C annealing produced similar performances in devices. For selected vacuum-treated solar cells (DBv-PSC) we applied 10$^{-2}$ mbar for 24h to the device inside a small vacuum chamber

*X-ray Diffraction:* X-ray diffraction analyses were performed using a high angular resolution diffractometer made by Bruker AXS equipped with a Cu-kα source, soller slits and a Goebel mirror. Line profiles were acquired at a fixed Bragg angle using a beam size of 1cmx1mm that was moved through the contact area.

*Conductive Atomic Force Microsc*opy: Morphology and current maps were acquired by conductive atomic force microscopy with a DI 3100 AFM by Bruker equipped with Nanoscope V electronics. A Pt-coated Silicon tip, connected to the current amplifier, was scanned on the sample's surface, while a dc bias was applied to the Al electrode of the cell. In addition to current maps, local current voltage (I-V) characteristics have been also acquired at several fixed positions of the tip by sweeping the dc bias.

*Device characterization:* J–V characteristics were measured by a digital source meter (Keithley model 2401) under AM 1.5 simulated sunlight (100 mW/cm$^2$)

from Peccell PEC-L01. The solar cells devices were masked to define the active area of 0.25 cm$^2$ and then irradiated from the back-side at the FTO/TiO$_2$ side. Scan range was from −0.1 to 1.2 V for forward scan and from 1.2 to −0.1 V for reverse scan with step of 0.01 V. The delay time was of 0.1 s.

## Appendix

The appendix of this chapter contains a table that describes the parameters used for solar cell characterization, frequency of analyses and ageing conditions.

| | | |
|---|---|---|
| **Solar cell characterization** | *Type of measurements* | *J-V curves* |
| | **Light source type** | Simulated sunlight (Peccell PEC-L01) |
| | **Intensity** | 100 mW/cm$^2$ |
| | **Spectrum** | AM 1.5 |
| | **Filters applied** | No |
| | **Active area** | 0.25 cm$^2$ (mask) |
| | **Range measurements** | -0.1-1.2 V |
| | **ΔV** | 0.01 V |
| | **Scan speed** | 0.50 mV/s |
| | **Atmosphere of measurements** | Air |
| | **Humidity** | 55% |
| | **Temperature** | 24 °C |
| | **Direction** | Forward and reverse |
| | **Preconditioning** | No |
| **Ageing conditions** | **Light** | No |
| | **Temperature** | 24 °C |
| | **Atmosphere** | N$_2$ |
| | **Electrical bias condition** | No bias |
| | **Encapsulation** | No |
| | **Comply with known protocols** | Similar to ISOS-D1 (but ageing in N$_2$ not in air) |
| **Measurements during ageing** | **Type of measurements** | J-V curves |
| | **Recording frequency** | Once per day for one month |

*Table A2.1 Parameters used for solar cell characterization, frequency of analyses and ageing conditions (ISOS-D1) taken from ref. [33].*

# References

[1] A.K. Jena et al. *J. Mater. Chem. A* 2018,6, 2219-2230.

[2] H. Chen et al. *Adv. Mater.* 2017, 29, 1603994.

[3] S. Kim et al. *Sci Rep* 2017, 7**,** 1200.

[4] K. Domanski et al. *ACS Nano*. 2016, 10(6), 6306-6314.

[5] Y. Cai et al. *Chin. Phys. B*. 2018, 27, 018805.

[6] H. Chen et al. *Mater. Chem. A*, 2019, 7, 15476–15490.

[7] M. Hadadian et al. *Energy Environ. Sci.,* 2020, 13, 1377-1407.

[8] V. Babu et al. *ACS Appl. Energy Mater*. 2020, 3, 5126−5134.

[9] L. Fagiolari, et al.  *Energy Environ. Sci.* 2019, 12, 3437-3472.

[10] D. Bogachuk et al. *Energy Environ. Sci.* 2020, 13, 3880-3916

[11] J. Zhou et al. *J. Mater. Chem. A* 2019, 7, 7710-7716.

[12] J. Barichello et al. *Solar Energy Materials and Solar Cells* 2019, 197, 76–83.

[13] M. Omrani et al. *Sci Rep* 2022, 12**,** 5367

[14] A. Alberti et al. *Adv. Energy Mater.* 2019, 9, 1803450.

[15] A. Alberti et al. *Nat. Commun.* 2019, 10, 2196.

[16] G. Mannino et al. *J. Phys. Chem. C* 2017, 121, 7703.

[17] I. Deretzis et al. *Appl. Phys. Lett*. 2015, 106, 131904.

[18] A. Alberti et al. *Riv. Nuovo Cimento* 2019, 7, 301-366.

[19] H. Zhang et al. *Adv. Funct. Mater.* 2018, 28, 1802985.

[20] H. Wei et al. *Carbon* 2015*,* 93, 861–868.

[21] https://creativecommons.org/licenses/by/4.0/

[22] E. Smecca et al. *Phys. Chem. Chem. Phys.* 2016, 18, 13413-13422.

[23] S. Sanzaro et al. *J. Mater. Chem. A* 2017, 5, 25529–25538.

[24] A. Fakharuddin et al. *Adv. Energy Mater.* 2017, 7, 1700623.

[25] H. Chen and S. Yang. *J. Mater. Chem. A* 2019, 7, 15476–15490.

[26] H. Back et al. *Energy Environ. Sci.* 2020, 13, 840–847

[27] S. Valastro et al. *Energies* 2020, 13(15), 3953

[28] D.R. Ceratti et al. *Adv. Mater.* 2018, 30, 1706273

[29] A.K. Jena et al. *Mater. Chem. A* 2018, 6, 2219–2230.

[30] P. Schulz et al. *Chem. Rev.* 2019, *119*, 3349–3417. 8.

[31] S. Shao and M.A. Loi. *Adv. Mater. Interfaces* 2020, 7, 1901469.

[32]  S. Valastro et al. *Front. Chem.* 2020, 8, 200

[33] M.V. Khenkin et al. *Nature Energy* 2020, 5, 35–49.

# Chapter 3: Eu-doped CsPbI₃ triple-mesoscopic carbon-PSCs

*In this chapter, sustainability is viewed from the perspective of the circular economy, more specifically from the viewpoint of materials recycle and device reuse. We thus demonstrate that the reuse of triple‑mesoscopic carbon‑based solar cells using CsPbI₃ as active layer is feasible. To the purpose, the special feature of the HT black γ-phase-reversibility is exploited.*
*The data shown in this chapter were published in Solar RRL (Valastro et al. 2022, 2200267).*

## 3.1    High-temperature CsPbI₃: applications and challenges

As discussed in Chapter 1, the black phase of Eu-doped CsPbI₃ can be formed at LT (80-90 °C) or at HT (325-250 °C). The black phase formed at HT exhibits better absorption properties with respect to that formed at LT (Figure 1.2d). In addition, the HT-γ black phase has a better thermal stability with respect to the LT-γ black phase.
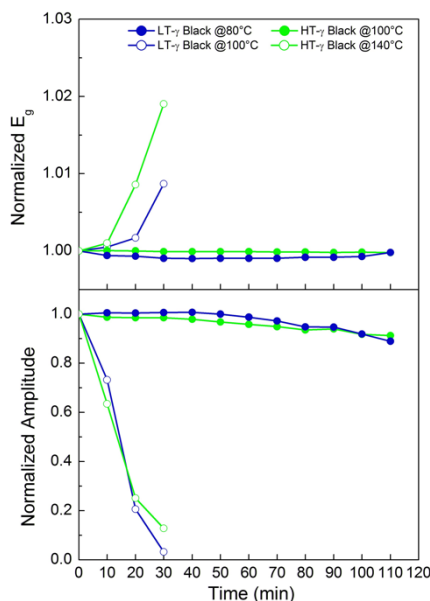


*Figure 3.1 LT and HT black phase thermal stability evaluated by stress tests in terms of the evolution over the time of $E_g$ and of the related amplitude A, calculated by CPs analysis, normalized to the respective values at t=0 for the LT-γ–black phase at 80° C and 100° C, and for the HT- γ– black phase at 100°C and 140°C.(Ref.[2], Creative Commons License CC BY 4.0[1])*

As shown in Figure 3.1, the HT-γ black phase is longly stable at 100 °C whereas the LT-γ black phase turns to yellow after 30 minutes[2]. We associate the differences between the two materials to a better lattice order in HT-γ black achieved as it is heated up to high temperature (325°C). For those reasons, in all the applications which do not require low temperature of fabrication (e.g. monolithic Si/PSK tandem solar cells) the HT-γ black is preferable.

The black phase of pure $CsPbI_3$, which can be formed exclusively at HT, exhibits a very poor stability in ambient air, being very sensitive to moisture which triggers the conversion towards the δ-yellow phase after a few minutes of exposure. For this reason, the materials and devices are mandatorily prepared in $N_2$-filled gloveboxes[3], hindering the chances for scaling-up and future commercialization. The use of additives[4] (organic, inorganic, elemental doping) in the $CsPbI_3$ precursor solution allows not only to form a black phase at LT (Chapter 1) but also to improve the morphological and structural properties of the $CsPbI_3$ films formed at HT[5]. As consequences, the $CsPbI_3$ layers prepared with additives have a better stability in air and enhanced device performances that enable out-of-glovebox procedures for PSC fabrication.

In the literature, $CsPbI_3$ perovskites have been widely used as active layers in the traditional architectures of cells[6,7], including planar low-temperature carbon-based HTL-free solar cells[8]. In those types of devices, the perovskite is spin-coated onto FTO/ETL substrates while the carbon contact, thanks to its low annealing temperature (<120 °C), is deposited directly on the $CsPbI_3$ surface by screen printing or doctor blading[9] techniques. Among the $CsPbI_3$-based LT-carbon HTL-free devices, Liang et al. [10] obtained a PCE of 12.04% by adding lead bromide and Indium Iodide to the $CsPbI_3$ solution; Xiang et al.[11] reached a PCE of 9.5% using hydrogen lead iodide ($HPbI_3$) as precursor[12] instead of $PbI_2$; more recently Zhang et al.[13] achieved a 10.95% of efficiency using CsBr in excess in the precursor solution and the bilayer $SnO_2$/ZnO as electron transporting layer. In 2021, Wang et al.[14] achieved the current record efficiency for carbon-based HTL-free PSCs with $CsPbI_3$, with a value of 14.6% using dimethylammonium iodide (DMAI) as additive in the $CsPbI_3$ precursor solution.

A different architecture of carbon based HTL-free PSCs is the triple mesoscopic carbon perovskite solar cells (mC-PSCs)[15,16,17]. This kind of device consists of three mesoporous layers including an electron transport layer (ETL, usually $TiO_2$), an insulating layer (usually $ZrO_2$) and a porous conductive carbon top electrode.

The whole structure has the value-added to be resistant to the high temperature (400-500 °C) that is usually applied to remove the organic binders. Perovskite solutions are usually infiltrated in the micrometer-thick stack by the drop-casting method. This architecture is 1) fully printable, making it industrially attractive due to the feasible scalability[18,19], 2) low-cost, avoiding expensive HTLs like spiro-

MeOTAD[20], 3) highly stable[21,22]. In addition, more recently, a module based on mC-PSCs using AVA-MAPbI$_3$ as active layer has surpassed, for the first time, the hotspot tests described in IEC 61215-2:2016 International standard for silicon-based PV and thin-film-based PV modules, showing an amazing strength against the reverse-bias-induced degradation[23].

Herein, we have successfully integrated and stabilized CsPbI$_3$ perovskites into a triple mesoscopic (mp) carbon architecture (mp-TiO$_2$/mp-ZrO$_3$/Carbon). CsPbI$_3$ is prepared with the addition of a small amount of Eu (Eu/Pb = 5%) introduced in the form of EuCl$_3$ (CsPbI$_3$:EuCl$_3$) or EuI$_2$ (CsPbI$_3$:EuI$_2$)[24,25], as seen in the Chapter 1. The high-temperature resistant mesoscopic carbon architecture allows producing an orthorhombic black γ-phase following the high-temperature route of formation by fast quenching the whole device from 350 °C to RT[26]. All devices are fabricated outside the glovebox, with an easily scalable nitrogen-assisted method. The integration of Eu in CsPbI$_3$ has the main role in reducing defects to boost efficiency and durability. The HT γ-phase integrated in such temperature-resistant device architecture owns the exceptional advantage of the reversibility of the phase transition[27] with mass preservation due to the lack of volatile organic cations. Recycle and reuse are indeed feasible.

## 3.2    Device fabrication and characterization

Three different CsPbI$_3$-bearing solutions, with and without Eu-precursors, were infiltrated into Carbon-Based Monolithic HTL-free architectures called mC-PSCs[28] (Solaronix). The preparation procedure is depicted in Figure 3.2 and further described in the Methods section. The three different samples are labelled hereafter as CsPbI$_3$:EuCl$_3$, CsPbI$_3$:EuI$_2$, and CsPbI$_3$. Figures 3.2a-b-c-d show the steps of the fabrication procedure of CsPbI$_3$ mC-PSCs, entirely performed outside the glovebox. After the monolithic triple mesoporous layer substrate has been annealed at 400 °C for 30 minutes to remove contaminants trapped in the porous structure, the perovskite solution was drop-casted in ambient air (RH 35%) on the carbon electrode surface, and got transported to the underlying porous layers by capillary action. To protect the CsPbI$_3$ from humidity and to ensure an optimal infiltration into the porous structure, the mC-PSC was placed under a dynamic nitrogen flow with a pressure slightly above the atmospheric value (Figure 3.2d).  The described method represents a low-cost easily implementable procedure, alternative to more complex and expensive processes involving gloveboxes. The devices were then annealed by a double step heating at 80 °C for 5 minutes and 350 °C for 2 minutes to form the CsPbI$_3$ black cubic α-phase (Figure 3.2c) and were immediately quenched at RT by flowing nitrogen to form the black orthorhombic γ-phase (Figure 3.2d)[2,26].

Figure 3.2e draws a section of the multilayer stack of a complete device, and Figure 3.2f shows the image of the device wherein the complete infiltration of the CsPbI$_3$ into the mesoporous layers under the carbon is visible. The deep CsPbI$_3$

infiltration into the whole mC-PSC structure is demonstrated by the uniform dark brown colour of the back side of the device when it is illuminated by the solar simulator (Figure A3.1).
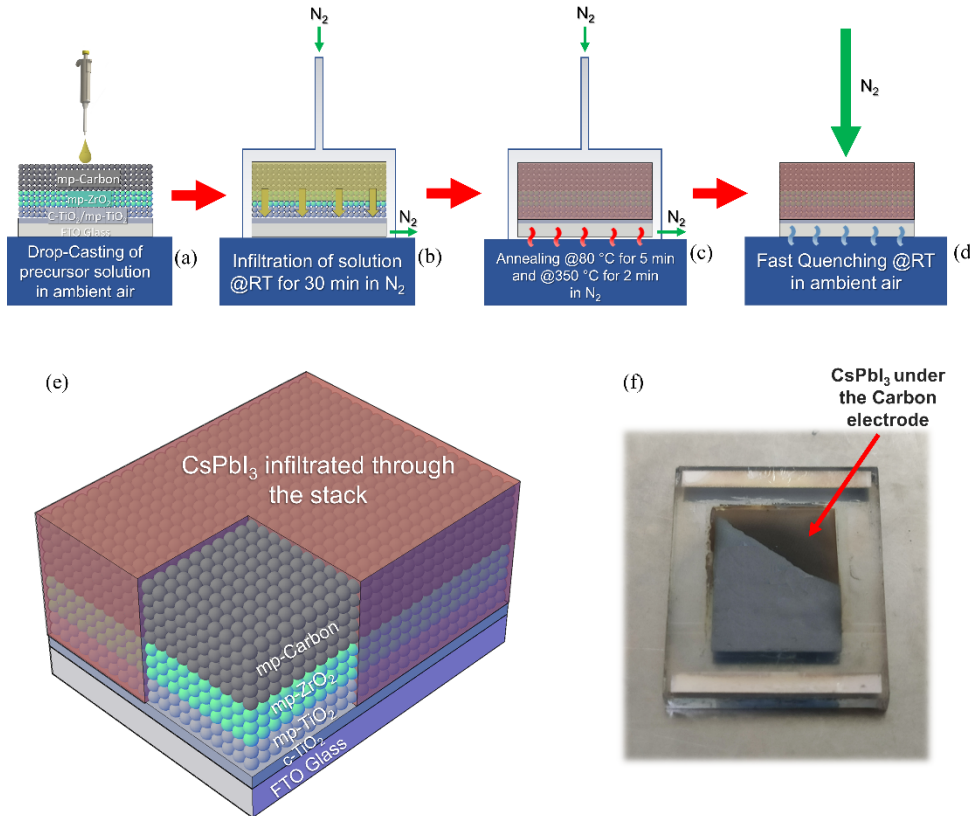


*Figure 3.2 (a)-(b)-(c)-(d) Schematic of mC-PSC fabrication procedure. (e) Schematic of mC-PSC architecture. (f) Photo of CsPbI₃-based mC-PSC. A part of carbon electrode was intentionally peeled-off. (Ref. [29]. Creative Commons License CC BY 4.0[1])*

The strength of the method in creating an interconnected meso-structured PSC has been evaluated by local analyses at the nanoscale through Conductive Atomic Force Microscopy (CAFM). Local current maps were collected by CAFM using a Pt-coated Silicon tip and by applying a bias to extract holes from the materials (figure 3.3a) owing to a proper band position of the Pt tip with respect to the components of the PSC (figure 3.3b).

All the measurements have been performed under dark conditions. Representative current maps coupled with the corresponding morphology (AFM) are shown in figures 3.3 c-f. The first raw of data refers to scans inside the mpC-PSK

region and shows modulations of currents in the 100 nA scale. Relatively darker areas in figure 3.3d are attributed to blends of PSK and mp-C crossing the contact section and indeed resulting in a more resistive percolation path for the current with respect to more conductive bordering regions with dominant mp-C. According to those findings, it has been found (figure A3.2) that the PSK and mp-C blend is identified by local I-V curve with a rectifying character (as in a Schottky diode) whilst regions dominated by mp-C are characterised by ohmic I-V curves. CAFM results, in combination with the morphological maps, denote that a blend between mp-C and PSK is well established. Moving to the underlying layer (figures 3.3 e-f) after mp-C removal, lower current intensity values were recorded (in the pA scale). This is due to the presence of lowly conductive materials under dark conditions. The CAFM map nicely allows distinguishing between regions that are less conductive (ZrO$_2$) with respect to their boundaries that are more conductive (PSK). These boundaries form a frame enveloping, grain by grain, the oxide scaffold. On this basis and by the comparison with the morphological map, it is undoubted that a blend of materials is established and that a deep infiltration path was followed by the PSK during device fabrication (see also figure A3.1).
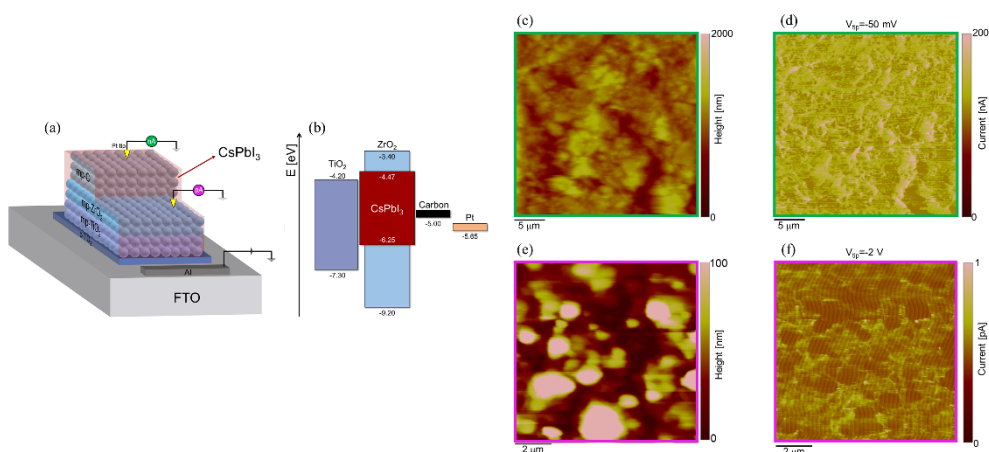


*Figure 3.3 (a) schematic of the mC-PSC structure with the CAFM setup: current flows vertically from the nanoscale tip contact through the entire architecture; (b) band positions for all the materials in the mC-PSC architecture; (c) and (d) AFM morphology and CAFM maps taken in the mpC-PSK blend; (e) and (f) AFM and CAFM maps taken in the ZrO$_2$-PSK blend: the PSK material (yellow colour) envelops the ZrO$_2$ grains (brown colour). Deep PSK infiltration is testified by the different percolation paths of the current. (Ref. [29]. Creative Commons License CC BY 4.0[1])*

We investigated the intrinsic structural and optical differences among CsPbI$_3$:EuCl$_3$, CsPbI$_3$:EuI$_2$ and CsPbI$_3$ deposited on bare glass by spin-coating (see Methods section for details) followed by annealing through the two-step procedure. The samples were analyzed by Spectroscopy Ellipsometry (SE) and the absorption

coefficient $\alpha$ ($cm^{-1}$) was extracted from the real ($\varepsilon_1$) and imaginary ($\varepsilon_2$) parts of the dielectric function using the equation $1.1^{30}$ shown in the Chapter 1.

Figures 3.4a-b display the absorption coefficient as a function of the photon energy and the energy gap calculated from Tauc-plots of $CsPbI_3:EuCl_3$, $CsPbI_3:EuI_2$, and $CsPbI_3$ samples. The profile of the absorption coefficient of $CsPbI_3$ (without Eu) was characterized by a huge sub-bandgap absorption in the range 1-1.7 eV. This feature is attributed to the presence of intrinsic defects states in the material[31]. A slight sub-bandgap absorption is also visible in the sample prepared with $EuCl_3$ but notably lower than in the reference sample without Europium. Finally, it is noteworthy that the sample prepared with $EuI_2$ did not have detectable sub-bandgap absorption. The normalized PL spectra of all samples did not display any peak in the range 1-1.7 eV (Figure A3.3), suggesting that the defect states are associated with non-radiative recombination. In analogy, in the literature, [10] it has been reported that sub-bandgap absorption is absent in $CsPbI_3$ prepared in $N_2$-filled gloveboxes. Hence, our results highlight the positive effect of Eu in controlling intrinsic defects, thus allowing the fabrication of a material with good optical properties without the use of a glovebox.

The bandgap energy of the three kinds of samples were estimated from the x-axis intersecting point of the linear fit; $(\alpha h\nu)^2$ vs $h\nu$ (Tauc-plot). As shown in Figure 3.4b, $CsPbI_3:EuCl_3$ and $CsPbI_3:EuI_2$ samples show slightly higher bandgap values (1.75 eV and 1.76 eV, respectively) compared to the sample w/o Eu (1.71 eV), which is in full agreement with the PL peaks shown in Figure A3.3.

Figure 3.4c shows the X-Ray Diffraction (XRD) patterns of the carbon monolithic stack infiltrated with $CsPbI_3:EuCl_3$, $CsPbI_3:EuI_2$ and $CsPbI_3$. The XRD pattern of the bare substrate acquired in the $\theta$–$2\theta$ configuration shows the distinctive peak of graphite at 26.5°, related to the carbon top electrode, the peak of $TiO_2$ at 25.3°, and the peak of $ZrO_2$ at 30.2°. The three patterns also bear features of the black orthorhombic $\gamma$-phase[26] of $CsPbI_3$ at 14.3° and 28.9° (as further supported by selected area diffraction patterns acquired by Transmission Electronic Microscopy and reported in Figure A3.4), confirming that the symmetric $\theta$–$2\theta$ configuration allows exploring the material in depth through the whole thickness of the mC-PSC architecture. To further explore the infiltration, as shown in figure 3.4d, we compared the XRD patterns collected in $\theta$–$2\theta$ and grazing incidence configuration at an incident angle of 0.4°, with special focus on the perovskite peak at 14.3°. The dominance of the peak intensity under $\theta$–$2\theta$ configuration reinforces the evidence of a deep infiltration and subsequent reaction of the perovskite material deep in the mesostructure. Similar results were obtained with $CsPbI_3:EuI_2$ and $CsPbI_3$.

To investigate the structural differences between $CsPbI_3:EuCl_3$, $CsPbI_3:EuI_2$, and $CsPbI_3$, we focused on the peak at 28.9° which is the most intense one. This peak is the result of the overlap of two peaks which were deconvoluted (pseudo-Voigt shape) and ascribed to (004) and (220) planes. The fitting curves are shown in Figure

A3.5. The lattice parameters, extracted by standard Rietveld refinement procedures and listed in Table 3.1, unveil some structural differences between the three perovskite lattices. The samples with Eu show a smaller c-value (the longest axis) with respect to pure $CsPbI_3$, producing a slightly measurable contraction of the unit cell volume[32], similarly as reported in our recent work[25] for black LT γ-phase formed at 80 °C. As a difference between $CsPbI_3$ LT γ-phase and HT γ-phase, the crystallite size was found to have an average diameter of 20 nm and 52 nm in the two cases, respectively. This finding indicates a better crystalline quality for the benefit of a lower volume density of intrinsic defects.

Europium addition in HT γ-phase of $CsPbI_3$ plays indeed a double role of decreasing: 1) the unit cell volume and 2) the crystallite size, with respect to pure $CsPbI_3$.
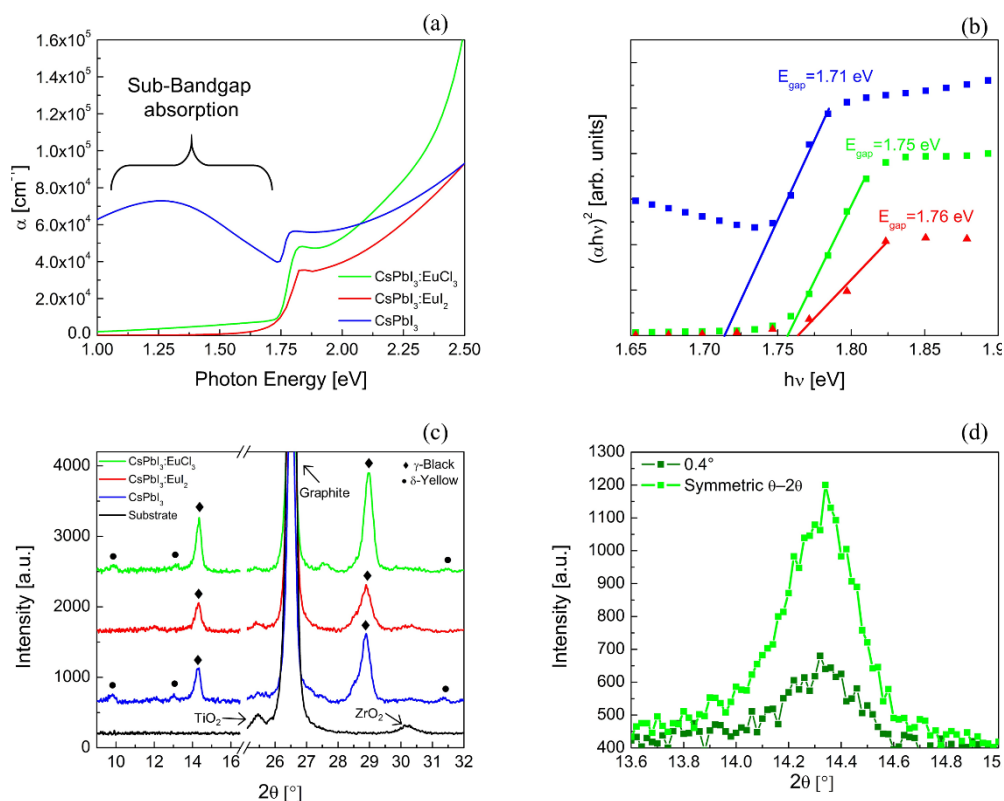


*Figure 3.4 (a) Absorption coefficient (α) of CsPbI₃:EuCl₃, CsPbI₃:EuI₂ and CsPbI₃ sample. (b) (αhν)² vs hν (Tauc-plot) for the extraction of the bandgap value for CsPbI₃:EuCl₃, CsPbI₃:EuI₂ and CsPbI₃. (c) XRD patterns of the substrate, CsPbI₃:EuCl₃, CsPbI₃:EuI₂ and CsPbI₃ samples. (d) XRD analyses using grazing incidence configuration at the incidence angle of 0.4° compared to θ–2θ configuration for CsPbI₃:EuCl₃. (Ref. [29]. Creative Commons License CC BY 4.0[1])*

As a similarity, $CsPbI_3$:$EuCl_3$ and $CsPbI_3$ samples prepared at HT in mC-PSC accommodate a small amount of the orthorhombic δ- phase (1-2%)[33], confirmed from peaks at 9.8°, 13.8°, and 31.4° (figure 3.4c). It is expected to be detrimental for the performance of the devices[34]. On the contrary, $CsPbI_3$:$EuI_2$ prepared at HT in mC-PSC does not show residual yellow phase.

| | *CsPbI₃* | *CsPbI₃:EuI₂* | *CsPbI₃:EuCl₃* |
|---|---|---|---|
| *a (Å)* | 8.76 | 8.76 | 8.85 |
| *b (Å)* | 8.70 | 8.70 | 8.57 |
| *c (Å)* | 12.45 | 12.41 | 12.39 |
| *Cell Volume (Å³)* | 949 | 946 | 939 |
| *Crystallite Size G (nm)* | 89 | 58 | 52 |

*Table 3.1 Lattice parameters extracted by standard Rietveld refinement procedure for CsPbI₃:EuCl₃, CsPbI₃:EuI₂ and CsPbI₃.*

Figure 3.5a displays the J-V curves of the best mC-PSCs fabricated with $CsPbI_3$:$EuCl_3$, $CsPbI_3$:$EuI_2$ and $CsPbI_3$  measured in forward and reverse scan (see Figure A3.6 for dark J-V curves) under solar simulator (AM 1.5, 100 mW/cm$^2$) The illuminated area of the solar cells was defined through a shadow mask having an aperture of  4.2 mm$^2$.

The solar cells based on $CsPbI_3$ using Eu as additive exhibited remarkably higher photovoltaic performances compared to those based on pure $CsPbI_3$. As a matter of fact, the best $CsPbI_3$:$EuI_2$ and $CsPbI_3$:$EuCl_3$ devices exhibited  a Power Conversion Efficiency (PCE) of 9.2% and 5.2% in the reverse scan, respectively, and these values were remarkably higher than that of the $CsPbI_3$ sample that demonstrated a poor efficiency of 1.4% (all photovoltaic parameters are listed in Table 3.2). All kind of $CsPbI_3$ mC-PSCs show hysteresis effect similarly to what was previously reported in the literature for mesoscopic carbon architecture infiltrated with other perovskite compositions[21,35]. In this regard, Rong et al.[36] recently reported that the hysteresis can be mainly attributed to the positive charge accumulation at the c-$TiO_2$/perovskite interface and it can be eliminated by regulating the c-$TiO_2$ thickness.
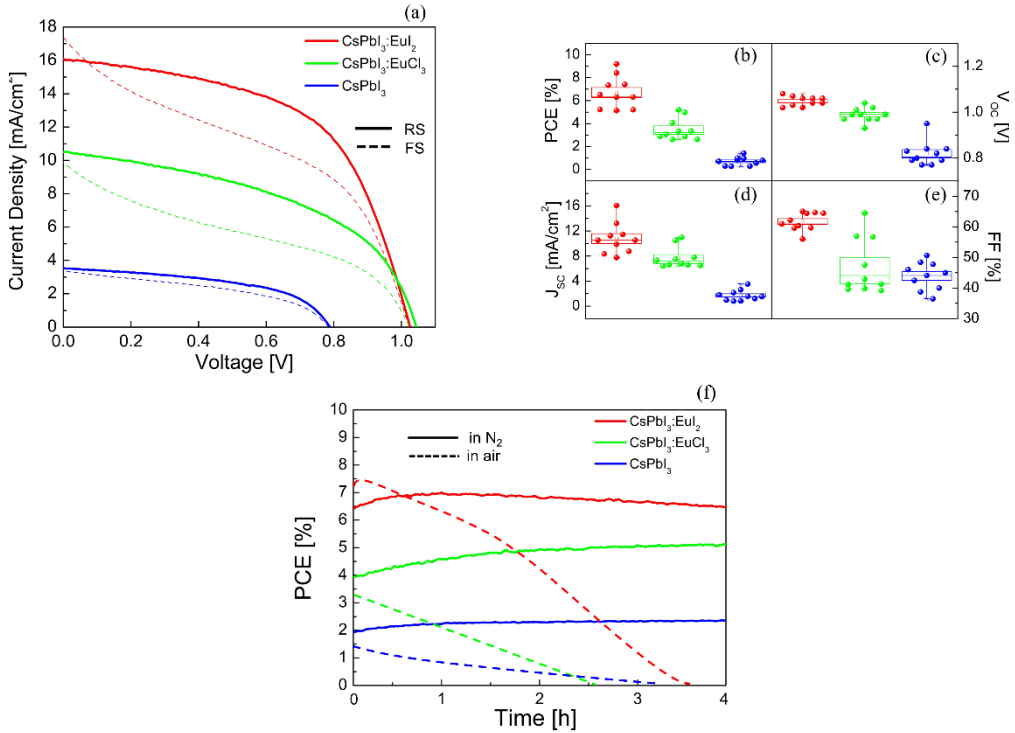
*Figure 3.5 (a) J-V curves in forward and reverse scan direction under solar simulator of the best mC-PSCs fabricated with CsPbI$_3$:EuCl$_3$, CsPbI$_3$:EuI$_2$ and CsPbI$_3$ perovskite. Statistical distributions as box-plots over ten devices for each kind of perovskite composition of PCE (b), V$_{OC}$ (c), J$_{SC}$ (d) and FF (e). (f) MPP Tracking of CsPbI$_3$:EuCl$_3$, CsPbI$_3$:EuI$_2$ and CsPbI$_3$ solar cell in N$_2$ environment (continuous line) and ambient air (dashed line). (Ref. [29]. Creative Commons License CC BY 4.0[1])*

| | PCE rs | V$_{OC}$ rs | J$_{SC}$ rs | FF rs | PCE fs | V$_{OC}$ fs | J$_{SC}$ fs | FF fs |
|---|---|---|---|---|---|---|---|---|
| *CsPbI$_3$:EuI$_2$* | 9.2 | 1.03 | 16.1 | 55.5 | 7.1 | 1.03 | 17.4 | 39.9 |
| *CsPbI$_3$:EuCl$_3$* | 5.2 | 1.04 | 10.5 | 47.6 | 3.4 | 1.02 | 9.9 | 33.9 |
| *CsPbI$_3$* | 1.4 | 0.79 | 3.5 | 50.7 | 1.1 | 0.79 | 3.4 | 42.8 |

*Table 3.2 Photovoltaic parameters extracted in reverse and forward scan for the best prepared CsPbI$_3$:EuI$_2$, CsPbI$_3$:EuCl$_3$ and CsPbI$_3$ devices.*

The statistics on 10 devices, as represented by box-plots in figure 3.5 b-c-d-e, confirm that CsPbI$_3$:EuI$_2$ shows higher values of all photovoltaic parameters with respect to CsPbI$_3$:EuCl$_3$ and CsPbI$_3$ samples. The lower performances of CsPbI$_3$:EuCl$_3$ with respect CsPbI$_3$:EuI$_2$ can be mostly explained by the presence of defect states acting as Shockley Read Hall (SRH) recombination centers that reduce V$_{OC}$ and FF values[37,38] (as disclosed by the data in figure 3.4) and partially by a residue of non-

photoactive yellow phase. This first effect is more pronounced in the devices without Eu wherein huge amount of pre-gap intrinsic defects (figure 3.4a) act on the overall performances.

Figure 3.5f shows the Maximum Power Point Tracking (MPPT) curve on unencapsulated devices (not the best prepared ones but other devices within the statistics reported in figures 3.5b-e) collected over 4 hours in $N_2$ environment under a continuous solar simulator. It shows a stable efficiency of ∼ 7% for $CsPbI_3$:$EuI_2$ and ∼ 2% for pure $CsPbI_3$ devices, whilst the PCE values of $CsPbI_3$:$EuCl_3$ devices increase from the initial 4% to ∼ 5%. However, in ambient air conditions, the MPPT curves were drastically different for the samples. This is ascribed to humid air action (RH ∼35%) that promotes the phase transition from the photoactive black orthorhombic HT γ-phase to the non-photoactive yellow δ-phase, leading to a fast efficiency decrease in ∼3 hours. The results suggest that focused strategies, like the encapsulation of mC-PSCs in $N_2$ environment[39], are needed to counteract degradation against phase transition and retain the stable high value of PCE of sample with Eu over time.

## 3.3    A simple procedure for the device reuse

What can be done after the black γ-phase is transformed into the yellow δ-phase? Being $CsPbI_3$ a full inorganic perovskite, the risk of mass loss during operational degradation ($T_{operation}$=40-80°C) is intrinsically prevented and consequently a full phase reversibility, in principle, is feasible.

To explore reversibility, the degraded mC-PSC devices with the yellow δ-phase inside were annealed at 350 °C for 2 minutes under dynamic nitrogen flow and rapidly quenched at RT, similarly to what done in the preparation of the initial devices. The method is shown in figure 3.6a. This procedure is feasible since the devices do not have organic layers in the architecture (like PCBM, spiro-MeOTAD etc.) which would easily degrade at the high temperature used for recycle. Moreover, traditional top contact materials like Au, Al, Ag, which would easily diffuse into the perovskite layer[40], are avoided using the mC-PSC architecture. In addition, the mC-PSC stack is resistant to high temperature (T∼400°C), making the recycling of solar cells easily achievable.

As a proof of concept, we recycled $CsPbI_3$:$EuCl_3$ and $CsPbI_3$:$EuI_2$ mC-PSC as described above, and compared the J-V curves (reverse scan) of recycled samples to those of the pristine devices, as plotted in figure 3.6b. It is noteworthy that both recycled $CsPbI_3$:$EuI_2$ and $CsPbI_3$:$EuCl_3$ showed PCE quite close to the original values, losing only ∼10% of their initial efficiency value (7.9% vs 8.7% for $CsPbI_3$:$EuI_2$ and 3.9% vs 4.2% for $CsPbI_3$:$EuCl_3$).

In the recycled devices, we observe an increase of the fill factor, a similar Voc, but a decrease of $J_{SC}$ compared to the values of the pristine samples, as shown in

Table 3.1. Further investigation on the recycling method and the characteristics of the recycled samples is needed to target a full recovery for unlimited cycles.
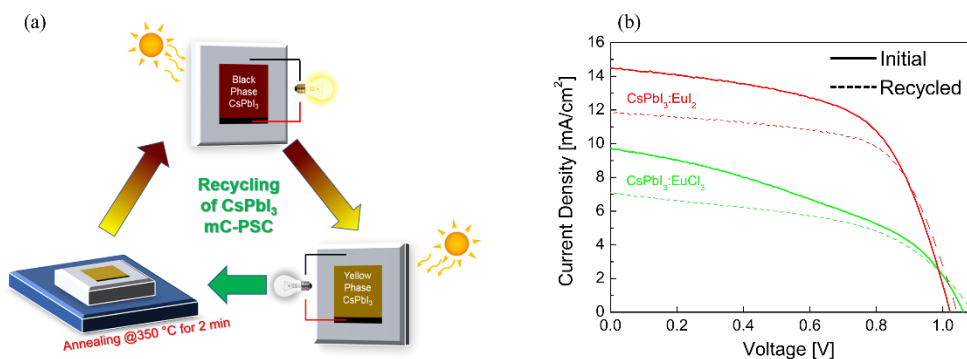


*Figure 3.6 (a) Schematic of recycle procedure for CsPbI₃ mC-PSC. (b) J-V curves acquired in reverse scan of pristine (continuous line) and recycled (dashed line) sample for CsPbI₃:EuCl₃, CsPbI₃:EuI₂ device. (Ref. [29]. Creative Commons License CC BY 4.0[1])*

|  | PCE (%) | $V_{OC}$ (V) | $J_{SC}$ (mA/cm²) | FF (%) |
|---|---|---|---|---|
| *CsPbI₃:EuI₂ pristine* | 8.71 | 1.03 | 14.53 | 58.3 |
| *CsPbI₃:EuI₂ recycled* | 7.88 | 1.04 | 11.93 | 63.8 |
| *CsPbI₃:EuCl₃ pristine* | 4.24 | 1.06 | 9.69 | 41.1 |
| *CsPbI₃:EuCl₃ recycled* | 3.87 | 1.08 | 7.09 | 50.5 |

*Table 3.2 Photovoltaic parameters of pristine and recycled devices prepared with CsPbI₃:EuCl₃ and CsPbI₃:EuI₂.*

To summarise, we fabricated mC-PSCs integrating the black HT γ-phase of pure and Eu-doped CsPbI₃ perovskite as the active layer. The perovskite integration was made outside the glovebox, in an ambient atmosphere with RH=35% and partially under dynamic N₂ flow. The Europium, added in the form of EuCl₃ and EuI₂, improves the quality of the material by mitigating the formation of intrinsic defects. Consequently, the best Eu-enriched CsPbI₃ devices achieved efficiency of 9.2% (EuI₂) and 5.2% (EuCl₃), notably higher than the efficiency of pure CsPbI₃ devices (1.4%). The integration process is simple with the huge value added of not requiring the use of gloveboxes that are instead expensive and unsuitable for production chains. Moreover, the overall architecture benefits from being HTL-free and indeed it is in the footstep of reducing cost of production.

The devices show good stability of performances under continuous illumination for 4 hours in $N_2$ environment. On the contrary, in ambient air, the mC-PSCs lose the initial efficiency after ~2 hours due to the γ-to-δ polymorphic transition.

The whole devices can be easily recycled by reconverting the yellow δ -phase to the black γ -phase, losing only 10% of the initial efficiency. The process does not require to recycle raw materials and does not involve expensive/highly energy-consuming processes.

Our pioneering study paves the way for easy fabrication and recycling of $CsPbI_3$ mC-PSCs. We argue that focused strategies, like the implementation in the mC-PSC architecture of hole-selective inorganic interlayers or coverages, can further improve the initial efficiency of the devices. Moreover, further progresses on the minimization of the efficiency loss after each recycle step can make $CsPbI_3$-based mC-PSCs competitive to other perovskite compositions and solar cell architectures.

## Methods

*Perovskite Film Fabrication*: A mix solution of 1 M $PbI_2$ (Tokyo Chemical Industry) and 1 M CsI (Tokyo Chemical Industry) was prepared by mixing them in a mixed solvent of DMF and DMSO (3:1 v/v). $EuCl_3$ (Sigma-Aldrich) and $EuI_2$ (Sigma-Aldrich) solutions of 0.1 M concentration were made in a mixed solvent of DMF and DMSO (3:1 v/v). The solutions were stirred at room temperature for 1 h. Then, 1 ml of the $PbI_2$/CsI solution was mixed respectively with 0.5 ml of the $EuCl_3$ solution for $CsPbI_3$:$EuCl_3$ samples and with 0.5 ml of the $EuI_2$ solution for $CsPbI_3$:$EuI_2$ samples to reach the desired stoichiometry and then stirred for 1 h. The entire procedure is conducted in ambient air (RH~35%). For SE and PL measurements the perovskite film was deposited by spin-coating the precursor solution on glass substrates in two steps: 1000 rpm for 10 s followed by 5000 rpm for 25 s in ambient environment.

*mC-PSC Fabrication:* The layers of monolithic architecture are screen-printed on a fluorine-doped tin oxide (FTO) glass substrate and consist of a compact titanium oxide (c-$TiO_2$) as hole blocking layer (~50 nm), a mesoporous $TiO_2$ (mp-$TiO_2$) as electron transporting layer (~500 nm), a mesoporous zirconium oxide ($ZrO_2$) as insulating layer (~1 μm) and a high temperature annealed carbon electrode (~10 μm). The entire procedure of $CsPbI_3$ solution infiltration is described in the main text.

*Conductive Atomic Force Microsc*opy: Morphology and current maps were acquired by conductive atomic force microscopy with a DI 3100 AFM by Bruker equipped with Nanoscope V electronics. A Pt-coated Silicon tip, connected to the current amplifier, was scanned on the sample's surface, while a dc bias was applied to the Al electrode of the cell. In addition to current maps, local current voltage (I-V) characteristics have been also acquired at several fixed positions of the tip by sweeping the dc bias.

*X-Ray Diffraction:* XRD patterns were collected using a D8Discoved (Bruker AXS) diffractometer equipped with a high-precision goniometer (0.0001 Å), a thin film attachment (long soller slits), and a Cu Kα source (instrumental broadening 0.07°). An Anton Paar heating stage, equipped with a polyether ether ketone dome filled with dry nitrogen at a pressure slightly above the atmospheric one (+0.3 bar), was used to keep the samples at controlled temperatures (30°C) in controlled atmospheres. The step size for pattern recording was 0.02° with acquisition time 12 s per step.

*Spectroscopic Ellipsometry*: We used a V-VASE, J A Woollam spectroscopic ellipsometry equipped with an autoretarder for optical characterization. Ellipsometric data have been collected at different angles below and above the Brewster angle of the glass substrate, over a wide range of wavelengths 245-1240 nm (1-5 eV) with step of 10 nm or less (5 nm) depending on the curve steepness. The optical model is a three-layer model that considers the optical constants of the glass substrate, the perovskite layer and the surface layer needed to simulate the layer roughness. Within the effective model approximation this last layer is assumed to be made 50% of the upper layer (air) and 50% of the lower layer (perovskite). The presence of a transparent substrate has been properly considered including the possibility that part of the light hits the back surface of the glass slide. We build a Kramers-Kronig consistent optical model based on multiple Critical Points Parabolic Band (CPPB) oscillators to fit experimental data (Ψ and Δ) and determine the real and imaginary part of the dielectric function. Measurements have been collected using a slightly over pressurized N$_2$ filled chamber in order to prevent perovskite degradation in air. The cell setup allowed to vary the temperature in the range 30-100 °C with an Instec MK100 heater/cooler system with an accuracy of 0.1 °C. Although it is known that CsPbI$_3$ is orthorhombic and therefore it presents an optical anisotropy along the three axes, this property has not been considered since the sample is a randomly oriented polycrystalline layer.

*TEM measurements:* TEM analyses were done in plan-view using a JEOL JEM 2010F microscope operating at 200 kV. The analysis is performed on the powder obtained by scratching the carbon electrode containing CsPbI$_3$:EuI$_2$ on the TEM grid.

*Device characterization:* J-V characteristics were measured by a digital source meter (Keithley model 2401) under AM 1.5-simulated sunlight (100 mW/cm$^2$) from Peccell PEC-L01. The solar cells devices were masked (shadow mask) to define the active area of 4.2 mm$^2$. Scan range was from −0.1 to 1.2 V for forward scan and from 1.2 to −0.1 V for reverse scan with a step of 0.01 V. The delay time was of 0.1 s. The Maximum Power Point Tracking is performed with a "Perturb and observe" algorithm. After the initial sweep to find the first maximum power point, the operating voltage is slightly perturbed to identify a new operating voltage which maximizes the output power (Perturb step). This voltage is maintained for 5 seconds and,

simultaneously, the output current is recorded (Observe step). These two steps are consecutively repeated for 4 hours.

## Appendix

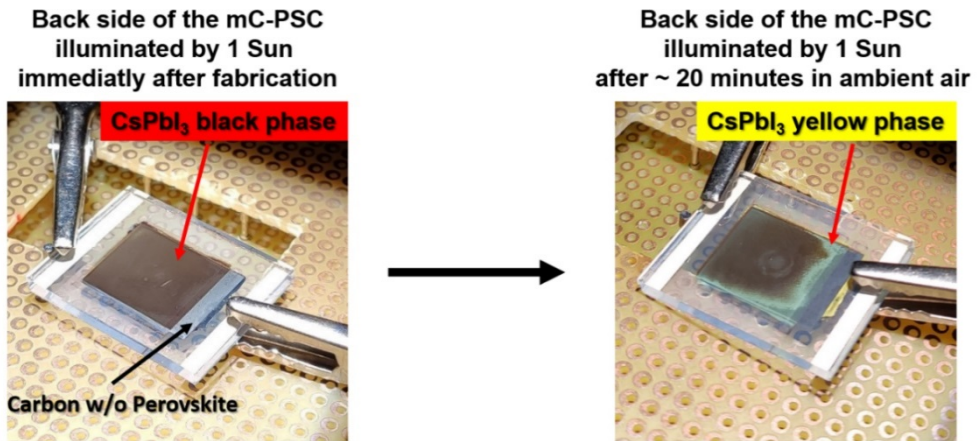The appendix of this chapter contains supplementary figures.



*Figure A3.1 Photos of the back side of CsPbI₃-based mC-PSC illuminated by 1 Sun immediately after fabrication when the film is totally black and after ~20 minutes in ambient air when the film begins to move to the yellow phase. (Ref. [29]. Creative Commons License CC BY 4.0[1])*
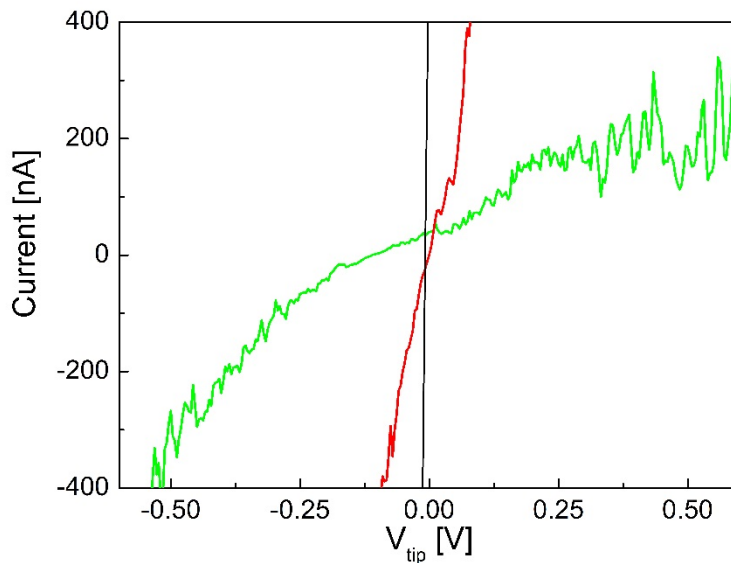


*Figure A3.2 I-V curves taken by CAFM on 1) the mpC-PSK blend (green curve) and 2) pure mpC (black curve). The red curve represents an intermediate case wherein graphite is dominant in the mpC-PSK blend. (Ref. [29]. Creative Commons License CC BY 4.0[1])*
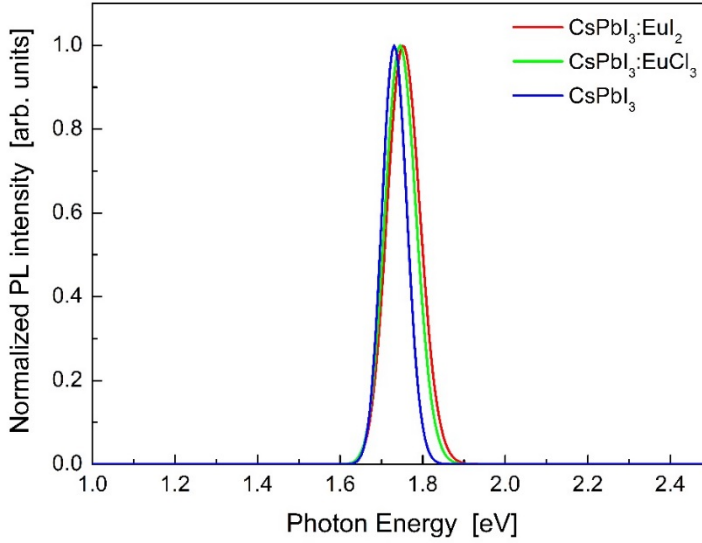
*Figure A3.3 Normalized photoluminescence (PL) spectra of CsPbI₃, CsPbI₃:EuI₂ and CsPbI₃:EuCl₃ samples on glass, taken with 440 nm wavelength as excitation source. (Ref. [29]. Creative Commons License CC BY 4.0[1])*
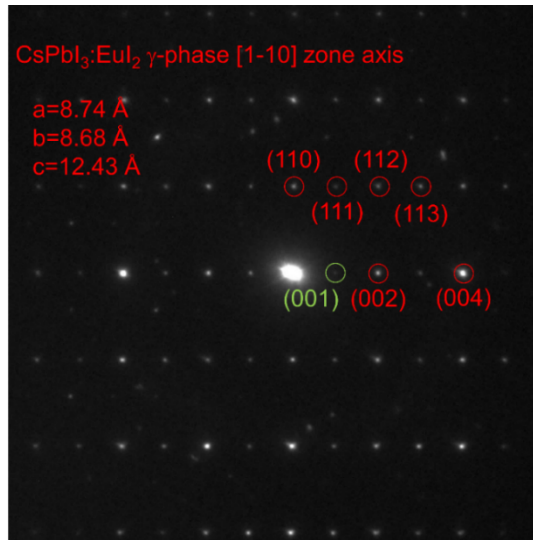


*Figure A3.4 Electron diffraction pattern of a single grain, derived from carbon infiltrated with CsPbI₃:EuI₂, observed along the [1-10] direction. The pattern can be unequivocally associated to γ-phase, due to the presence of the (001) spot arising from planes having 1.243 nm as interplanar distance, diagnostic of the black orthorhombic γ-phase. Cell parameters were deduced from the comparison and fitting of several different electron diffraction patterns*
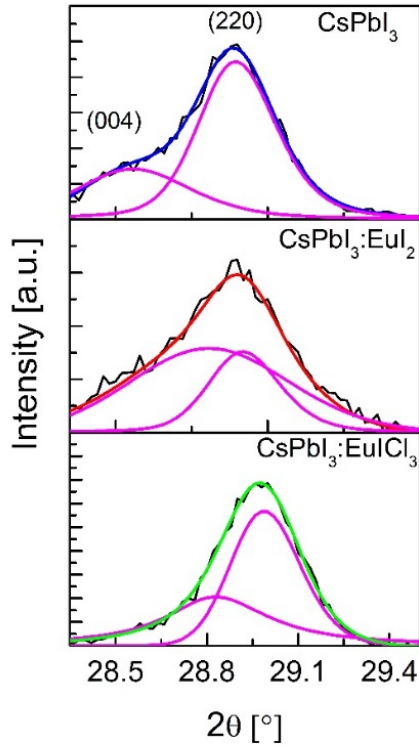
*Figure A3.5 Peak deconvolution around 2θ ≈ 28.9° for CsPbI₃, CsPbI₃:EuI₂ and CsPbI₃:EuCl₃ sample with Pseudo-Voight profiles for the single contribution. (Ref. [29]. Creative Commons License CC BY 4.0[1])*
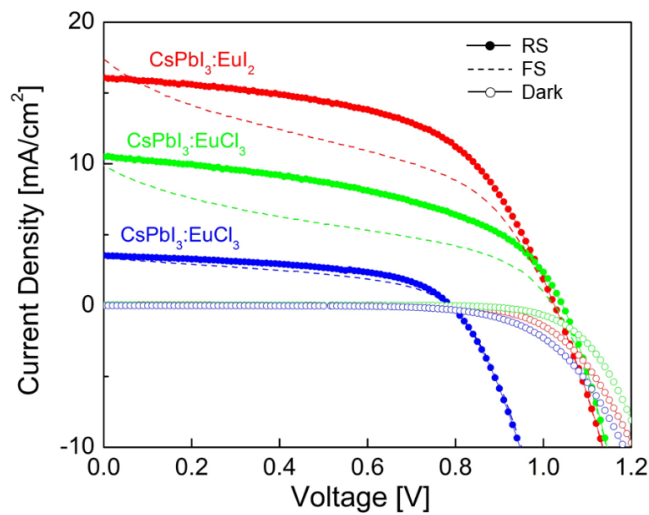


*Figure A3.6 J-V characterization of the best mC-PSCs fabricated with CsPbI₃:EuCl₃, CsPbI₃:EuI₂ and CsPbI₃ perovskites. (Ref. [29]. Creative Commons License CC BY 4.0[1])*

# References

1 https://creativecommons.org/licenses/by/4.0/

2 S. Valastro et al. *J. Phys. Mater.* 2021, 4, 034011

3 L. Liang et al. *J. Mater. Chem. A*, 2019, 7, 26776

4 Y. Ahmed et al. *J. Energy Chem.* 2022, 67, 361

5 D.Y. Heo et al. *J. Phys. Chem. C* 2018, 122, 15903

6 H. Yao et al. *Mater. Chem. Front.* 2021, 5, 1221

7 X. Chang et al. *Adv.Mater.* 2020, 32, 2001243

8 D. Bogachuk et al. *Energy Environ. Sci.* 2020, 13, 3880

9 Y. Yang et al. *J. Mater. Chem. A* 2019,7, 22005

10 J. Liang et al. *Adv. Mater.* 2019, 31, 1903448

11 S. Xiang et al. *ACS Energy Lett.* 2018, 3, 1824

12 W. Ke et al. *Nat. Comm.* 2018, 9, 4785

13 J. Zhang et al. *J. Alloys Compd.* 2021, 862, 158454

14 H. Wang et al. *Nano Energy* 2021, 84, 105881

15 S.M.P. Meroni et al. *Energies* 2021, 14, 386

16 Z. Ku et al. *Sci. Rep.* 2013, 3, 3132.

17 J. Baker et al. *J. Mater. Chem. A* 2017, 5, 18643.

18 M. Duan et al. *Today Energy* 2018, 7, 221

19 A. Verma et al. *J. Mater. Chem. C* 2020, 8, 6124

20 S. Valastro et al. *Front. Chem.* 2020, 8, 200

21 G. Grancini et al. *Nat Commun* 2017, 8, 15684

22 A. Mei et al. *Science* 2014, 345, 295

23  D. Bogachuk et al. *Sol. RRL* 2021, 2100527

24 A. K. Jena et al. *Chem Mater* 2018, 30, 6668

25 A. Alberti et al. *Adv. Energy Sustainability Res.* 2021, 2, 2100091

26 R.J. Sutton et al. *ACS Energy Lett.* 2018, 3, 1787

27 A. Marronnier et al. *ACS Nano* 2018, 12, 3477

28 S. Zouhair et al. *Sol. RRL* 2021, 2100745

29 S. Valastro et al *Sol. RRL* 2022, 2200267

30 M. Fox 2010 Optical Properties of Solids (Oxford: Oxford University Press)

31 B. Subedi et al. *Sol. Energy Mater Sol. Cells* 2018, 188, 228

32 S. Valastro et al. *Sol. RRL* 2022, 6, 2200008

33 H. Meng et al. *ACS Energy Lett.* 2020, 5, 2630

34 D. Liu et al. *Small Struct*. 2021, 2, 2000089

35 L. Zhou et al. *Sci Rep* 2019, 9, 8778

36 Y. Rong et al. *Energy Environ. Sci.* 2017, 10, 2383

37 T.S. Sherkar et al. *ACS Energy Lett.* 2017, 2, 1214

38 G. Landi et al. *Adv. Sci.* 2017, 4, 700183.

39 A. Alberti et al. *Adv. Energy Mater.* 2019, 9, 1803450

40 W.Ming et al. *Adv. Sci.* 2018, 5, 1700662

# Chapter 4: Sequestration of leaked Pb from PSCs by TiO₂ sponges

*In this chapter, the concept of sustainability is interpreted as protection of environmental matrixes against toxic elements present in the perovskite compositions. It will be demonstrated that Pb release in the environment by eventually damaged PSCs can be prevented using a transparent TiO₂ sponge for its stable sequestration. The same sponge can be used for Pb recycle in end-of-life devices.*
*The data shown in this chapter can be found in Nature Sustainability (Valastro et al., accepted for publication).*

## 4.1    Pb leakage from PSCs: concerns and strategies

Some issues are still hindering the commercialization of PSC technologies. Remedies have been proposed to increase the stability of the interfaces[1] and to rationalize up-scalable production chains[2]; nonetheless, the potential release of Pb in the environment remains the biggest concern.

It is a matter of consensus that Pb ions, dissolved from residual $PbI_2$ salts by water action on the exposed perovskite film after events of break (catastrophic events like hail, storms, hurricanes or other mechanical failures) can enter soil and groundwater. It was reported in the literature[3] that $Pb^{2+}$ leaked from perovskite films can enter plants, crops, and consequently the food cycle ten times more efficiently than Pb contaminants coming from other Pb -containing electronic devices. This seems to be enhanced by the presence of organic cations like Methylammonium ($MA^+$) which promotes the Pb uptake[4]. The potential Pb leakage can indeed be viewed as a public environmental and health risk source, especially with PSCs applied in Agrivoltaics[5], in Building Integrated and Building Applied Photovoltaics (BIPV and BAPV)[6]. For all those applications, achieving and preserving semi-transparency (ST) along the production chain are targeted issues. The massive production of ST-PSC without worries about the presence of Pb is indeed a transversal pivotal challenge.

To solve the concern, two different routes can be pursued: 1) the substitution of Pb with other elements like tin[7] ($Sn^{2+}$) and 2) a direct action against Pb release through focused strategies. The first approach is currently deserving a huge effort to tackle the compositional stabilization of the perovskite against the tendency of $Sn^{2+}$ to change its charge state to $Sn^{4+}$. Moreover, the efficiency record value in tin halide solar cells (~14%[8,9]) is currently far from one of the Pb -based solar cells (25.8%), making Pb a necessary actor to accelerate the lab-to-fab-to-market transition.

On the other side, mitigation of Pb leakage is achieved either by encapsulating materials[10] that protect devices from mechanical damages or by materials that

sequestrate Pb through chemical adsorption mechanism[11]. Encapsulation alone is not enough to fully prevent the Pb leakage from perovskite modules, especially under breaks in severe weather conditions and, consequently, Pb-absorbing layers are required in addition. The ones proposed in the literature[12,13,14,15] are resins or polymers deposited by spin-coating or doctor-blading methods on the surface of transparent conductive oxides (TCO) or the charges transporting layer (CTL) of the solar cell, with a drawback in complicating the fabrication flow-chart and potentially limiting the charges transport through the device. A recent approach[16] consists of applying a Pb -absorbing material named P, P'-di(2-ethylhexyl) methanediphosphonic acid (DMDP) (thickness of 5.7 µm) on ethylene-vinyl acetate (EVA) foils which is a standard encapsulating material used in PV technology. This remedy has achieved the capture of 99.8% of Pb leakage. DMDP was applied on both the front and back sides of the solar cell, with a rise in consumption of materials, costs, and complexity. As a common trait, all the aforementioned Pb-absorbing materials are fabricated by wet chemical methods (Figure 4.1a) using solvents whose losses would contribute to a significant part of the organic pollution[17,18], with the disposal of the related large waste is a further concern[19].

There is a large consensus in the literature that titanium dioxide ($TiO_2$) is a material with high adsorption capability towards metal ions[20,21] specifically on $Pb^{22}$, for environmental risk mitigation. $TiO_2$ has been used over several decades for many purposes, including contaminated water treatments[23] (never for PSC), since it is non-toxic, low-cost and insoluble in water. In addition, $TiO_2$ is one of the most used and efficient electrons transporting layer (ETL) in perovskite solar cell architectures[24]. It is fabricated by different techniques like chemical approaches[25] but also with solvent-free methods like atomic layer deposition[26] and sputtering[27]. Combining the two uniqueness of the material leads us to conclude that, as soon as a $TiO_2$ layer is enabled for the capture of Pb eventually released from perovskite solar cells, it will attract a huge interest to be integrated into device architecture without high extra costs for equipment investment, well-fitting its fast industrialization in production flow-charts.

## 4.2    Gig-lox $TiO_2$ sponge integration in PSCs for Pb sequestration

We propose a solvent-free physically deposited porous $TiO_2$ material as a transparent adsorbing layer to capture Pb eventually released in water environments from damaged PSCs. As a further applicative impact, it can be used to capture lead from end-of-life perovskite solar cell devices during recycling.

$TiO_2$ layers were grown at room temperature (RT) with DC-pulsed (Direct Current) sputtering equipment. The method bears the great advantages of the up-scalability for industrialization and the material reproducibility over large areas[28] for the benefit of high production throughput. Wasting material is intrinsically avoided

with this approach (Figure 4.1b). We specifically applied a grazing incidence geometry for the titanium atoms flux travelling through the plasma and a growth process assisted by local oxidation at the substrate side through oxygen confinement. The process is hereinafter called gig-lox. It permits the growth of a spongy fine-branched structure with interconnected mesopores (pipelines) and nanopores that guarantee an in-depth pathway of hosts into the porous structure. Gig-lox TiO₂ layers grown at RT offer high surface exposure[32] and reactivity. As a matter of fact, the same sponge was previously applied for gas sensing (active layer)[28,29], molecular functionalization[30] and photovoltaics (ETL for PSC)[31,32], taking additional advantages from the material transparency. Deposition at RT further enables the integration of gig-lox TiO₂ layers as the last production step on any kind of ready-to-use-PSC architecture.

We exploited all those gig-lox TiO₂ properties for Pb sequestration experiments. As a technological proof-of-concept, we have integrated a 340 nm-thick gig-lox TiO₂ layer at room temperature on a ready-to-use p-i-n solar cell made by a stack of ITO/PTAA/MAPbI₃-HEC/PCBM/BCP/Au in which the active layer is a 220 nm-thick blend (Figure 4.1c). The blend, made by MAPbI₃ and a small amount of Hydroxyethyl cellulose (HEC), was applied in a recent work[33] to improve the transparency of the perovskite active layer, still maintaining good efficiency for application in BIPV, BAPV and Agrivoltaics.

The gig-lox TiO₂ has been deposited on the back side of the unprotected ready-to-use solar cells, in contact with the Au contacts and the BCP layers. No surface damage or modifications are found after deposition. Figures 4.1d-e show how a representative PSC appears with respect to its pristine aspect. As a first paramount result, the current density-voltage (J-V) curves taken in reverse scan on the same device (Figure 4.1f) are unchanged before and after deposition, demonstrating that no damage/changes occur on the underlying layers during the sputtering process. The corresponding J-V curves in the forward scan follow the same behaviour and are shown in Figure A4.1. In addition, the Average Transmittance (AVT) value on the PSC covered with gig-lox TiO₂ and measured in the visible range (400-800 nm) is unmodified at a value of 31.4%. That is an optimal value for application in BIPV[34] and Agrivoltaics[5]. The transmittance curve of the gig-lox TiO₂-covered device is reported in Figure A4.2 (before water soaking).

To investigate the effectiveness of the Pb capture by gig-lox TiO₂, we have soaked the covered devices in 10 ml of deionised water for 10 days to permit water to fully infiltrate and dissolve the perovskite layer. Identical devices without TiO₂ coverage were soaked in the same amount of water for comparison. Our intent was to simulate extreme rainfall conditions that are nowadays not unusual due to the ongoing severe climate change, and accordingly, we assumed a rainfall rate (rain shower) of 3 cm/h lasting for 3 hours. Furthermore, we supposed that the PV maintenance crew intervenes to repair the damaged panels 10 days after the incident. It is important to

recall that, in our experiment, the PSCs are soaked in $H_2O$ without any type of other encapsulation, i.e. fully exposed to direct water action. In other literature papers[12,13,14,16], instead, the soaking experiments were done on encapsulated (e.g. with an encapsulant material and a cover glass) devices damaged on the surface with a blade cutter or hammer in order to allow water infiltration towards the PSC. We indeed do not simulate the break being the devices under the worst shape with the perovskite more closely exposed to water. To further worsen the conditions, the vials containing devices in water are mechanically shaken on a flat orbital shaker at a frequency of 200 rpm all over time.

When dipped into water, both devices uncovered and covered with gig-lox $TiO_2$, immediately change their colour from the initial brown (Figure 4.1d-e) to yellow (Figure A4.3) reflecting the transformation of $MAPbI_3$ into $PbI_2$. With time, they become more and more transparent indicating the complete dissolution of $PbI_2$ (Figure A4.3). This evidence indicates that the gig-lox $TiO_2$ layer does not act as an encapsulant because it does not prevent water access through the device layers, as expected owing to its characteristic porosity. We measured the Pb concentrations in water at the end of the full PSCs soaking by inductively coupled plasma mass spectrometry (ICP/MS) (Figure 4.1g). The Pb concentration in water hosting the uncovered PSC is 2.65 ppm, a value close to the calculated amount of Pb in 220 nm-thick and 1 $cm^2$ water-exposed area of $MAPbI_3$ (2.90 ppm). Conversely, in the water hosting the gig-lox $TiO_2$-covered PSC, the Pb concentration is significantly reduced to 0.26 ppm (average value calculated on three different soaked samples reported in Table A4.1), indeed corresponding to a considerable value of Pb sequestration efficiency (SQE) of 90.2%. The data demonstrates that the 340nm-thick gig-lox $TiO_2$ layer effectively acts as a filter to capture Pb to minimise its release in water from unprotected (without protective glass coverage) or damaged (with the protective glass broken, being less exposed than the uncovered) PSCs. The finding was complemented by a similar experiment in which the gig-lox $TiO_2$ coverage on the PSC was raised to 1100nm (Figure A4.4). The density ($g/cm^3$) of the upper portion of the gig-lox layer (~20nm from the surface) measured by X-ray Reflectivity unveils that lead atoms do not reach the surface in this last case. The finding, joined with the evidence that lead species are not found in water, leads us to argue that the Pb sequestration within the gig-lox layer is a bottom-up process that starts at the interface with the device and proceeds upwards likely assisted by capillary forces.
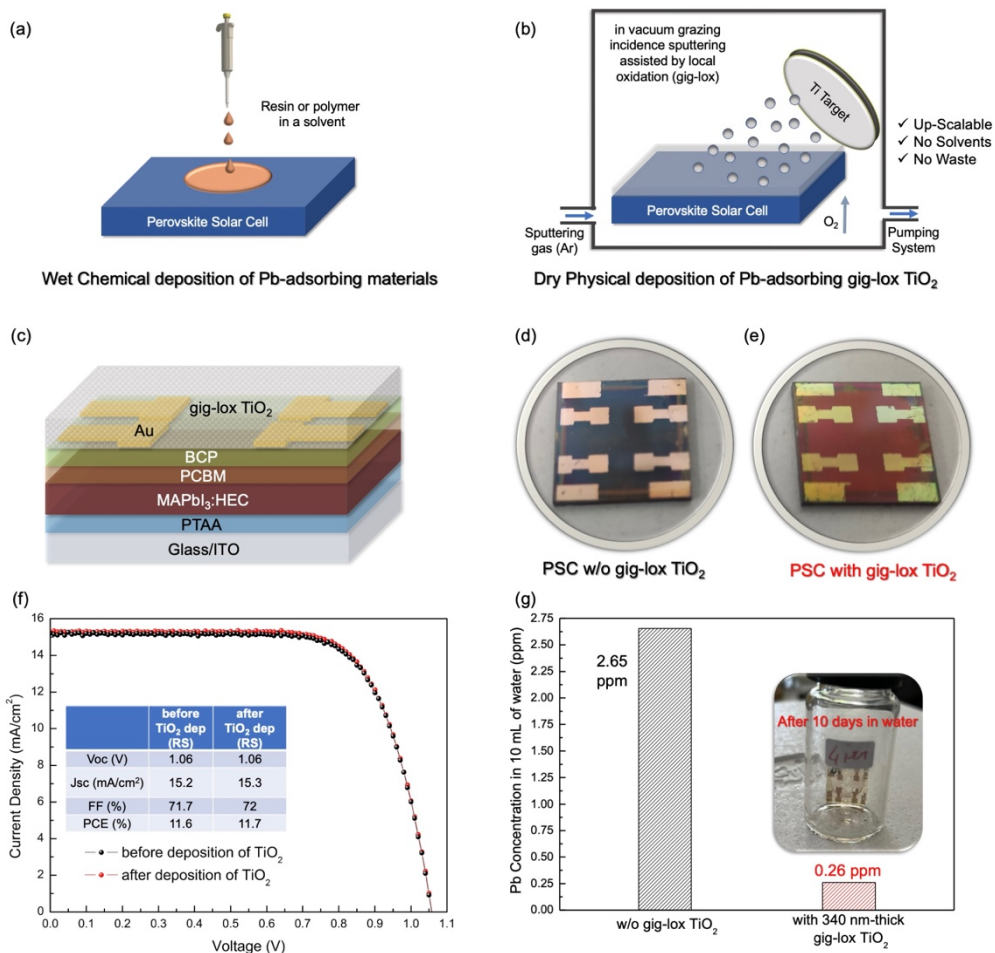
*Figure 4.1 (a) Pb-adsorbing materials fabricated by wet chemical approaches vs (b) gig-lox TiO$_2$ fabricated by dry physical method. (c) Architecture of a semi-transparent perovskite solar cell with the gig-lox TiO$_2$ layer directly deposited on it. Photo of the PSC before (d) and after (e) the gig-lox TiO$_2$ deposition. (f) Representative current density vs. voltage curves (J-V) of the PSCs before and after the gig-lox TiO$_2$ deposition. (g) Pb concentration after 10 days of soaking in 10 mL of water of PSCs with and without gig-lox TiO$_2$. The values are calculated in average on three soaked devices.*

## 4.3    Kinetics and adsorption mechanism of Pb sequestration by gig-lox TiO$_2$

To closely investigate the kinetic of Pb adsorption into the 340 nm-thick gig-lox TiO$_2$ layers, we have deposited a layer equivalent to the one used on PSC (340 nm) but on 1.25x1.25cm bare glasses (schematic in Figure 4.2a). They have been soaked into three different aqueous solutions of lead-iodide (PbI$_2$) with known Pb ions concentrations, specifically: 2.2 ppm, a value close to the Pb amount released by the

soaked semi-transparent PSCs without $TiO_2$; 1 ppm; 0.4 ppm. The samples were mechanically shaken for all the test period (inset of Figure 4.2b) and the Pb-concentration in water was monitored along a time interval of 96 hours (it was not necessary to prolong to 10 days due to value saturation). As shown in Figure 4.2b, the gig-lox $TiO_2$ sequesters a percentage in the range of 90-94% of the initial Pb in water in the first 4 hours of dipping (the perovskite layer integrated into the devices was dissolved in a couple of hours[16]). This percentage well agrees with the Pb-SQE value measured in soaked PSCs.
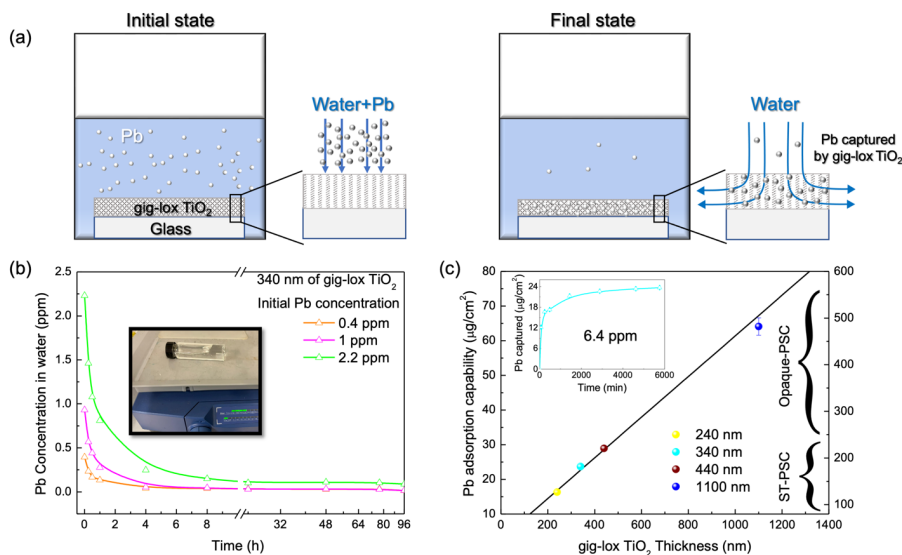


Figure 4.2 (a) Schematic of the experimental setup: 340 nm-thick gig-lox $TiO_2$ layers deposited on bare glass soaked into Pb-containing water solution. (b) Pb concentration in water vs time for 340 nm-thick gig-lox $TiO_2$ layers soaked into different Pb-concentrated water solution: the final Pb-concentration values measured in water are 14.5, 14.8 and 88.1 ppb, for 0.4 ppm, 1 ppm and 2.2 ppm respectively. The inset is the sample into the vial over the mechanical shaker, continuously working at 200 rpm for 96 hours. The error bars in Pb concentration measurements by ICP/MS is 1%. (c) Pb adsorption capability values, with error bars, measured in different thicknesses of gig-lox $TiO_2$ (240, 340, 440 nm) soaked in 6.4 ppm Pb water solution (a representative kinetic curve of the Pb captured into 340nm-thick gig-lox $TiO_2$ layer is shown in the inset). The calculated Pb-adsorption capability is 70 ng/(cm$^2$·nm) in 340nm of gig-lox $TiO_2$ and ~58 ng/(cm$^2$·nm) in the range 240-1100nm from the linear fit in Figure 4.2c. The sequestrated lead is made in relationship (right axis) with the corresponding $MAPbI_3$ thickness, once all the Pb contained in the film is dissolved in water. Thereby, a gig-lox $TiO_2$ layer in the range of thickness 240-440 nm sequesters all Pb contained in Semi-Transparent (ST) PSCs (70-240 nm). If thicker gig-lox $TiO_2$ layers are grown (e.g.1000nm), they can be also used for the full Pb capture in opaque PSCs.

The experiment also demonstrates that the gig-lox TiO$_2$ layer is effective in capturing Pb also from its top, according to the peculiar, branched porosity with vertical pipelines across the entire layer thickness (structure commented later on). In the three explored cases, the maximum capture of Pb is limited by its concentration in the solution.

A second pivotal finding is that the gig-lox TiO$_2$ layer does not release the captured Pb in water for a prolonged dipping time up to 96 hours under continuous mechanical shaking. This evidence demonstrates that the captured lead is well linked to the oxide and suggests a chemical anchoring onto the gig-lox TiO$_2$ surfaces.

The adsorption capability of the gig-lox TiO$_2$ layer was further boosted by soaking it in a more concentrated Pb solution (6.4 ppm). In this case, the Pb capture is limited by the number of available binding sites within the 340 nm thickness, and therefore the adsorption saturates to a final value of 24 $\mu g_{Pb}/cm^2$ (normalized to the gig-lox TiO$_2$ sample area, inset of figure 4.2c). We observe that the Pb capture by gig-lox TiO$_2$ results in modifications of the optical response of the layer, namely the absorption coefficient and the transmittance of the material, as shown in Figure A4.5.

Now, we explore the Pb-adsorption tunability by varying the film thickness. Indeed, we deposited gig-lox TiO$_2$ on bare glass with thicknesses of 240, 440 and 1100 nm to soak them into 6.4 ppm of Pb in water solution and monitor the Pb adsorption over time (the same experiment with similar results was done using polymeric foils as substrate). The 240nm, 440nm and 1100 nm-thick layers achieve a maximum Pb adsorption of 16 $\mu g_{Pb}/cm^2$, 29 $\mu g_{Pb}/cm^2$ and 63 $\mu g_{Pb}/cm^2$, respectively. Those results describe how the gig-lox TiO$_2$ layer thickness can be engineered according to the specific need, which is firstly dictated by the perovskite thickness and secondly by the specific architecture and application.

Figure 4.2c also offers a figure of merit on the fine thickness scale-up of the oxide layer in relationship with the MAPbI$_3$ thickness to be used in the device: gig-lox TiO$_2$ layers in the range of 240-440 nm are able to capture all the Pb contained in MAPbI$_3$ layers in the range of thickness 70-240nm, usually applied/needed in ST-PSCs for BIPV and Agrivoltaics[6]; gig-lox TiO$_2$ layers with thicknesses of 1100 nm allows to sequester all the Pb contained into 500 nm-thick MAPbI$_3$ layers used for opaque PSCs. The calculated Pb-adsorption capability (linear fit in Figure 4.2c) of the gig-lox TiO$_2$ layer is ~58 ng/(cm$^2$·nm) that is close to what was previously achieved in the literature with chemical DMDP (54 ng/(cm$^2$·nm))[12,16]. Fine tunability of the gig-lox TiO$_2$ thickness by regulating the deposition time is a further value-added for the adaptability to a specific application/need.

Hereafter some additional remarks that sum-up to the transparency of the layer, the easy integrability and the methodological sustainability:

1)    Gig-lox TiO$_2$ layers with proper thickness can be deposited at RT on any kind of substrate for direct (on ready-to-use device) or indirect (on glass or foils) capture of Pb, as summarised in Figure 4.3.

2)    The Pb adsorption capability in gig-lox TiO$_2$ layers does not depend on the substrate used. Figure A4.6 shows a comparative capturing behaviour in oxide layers deposited on glass and Polyethylene naphthalate (PEN) foils.

3)    Pb sequestration in end-of-life devices can be engineered by TiO$_2$ capturing surfaces, using flat or bent surfaces, for recycling purposes.
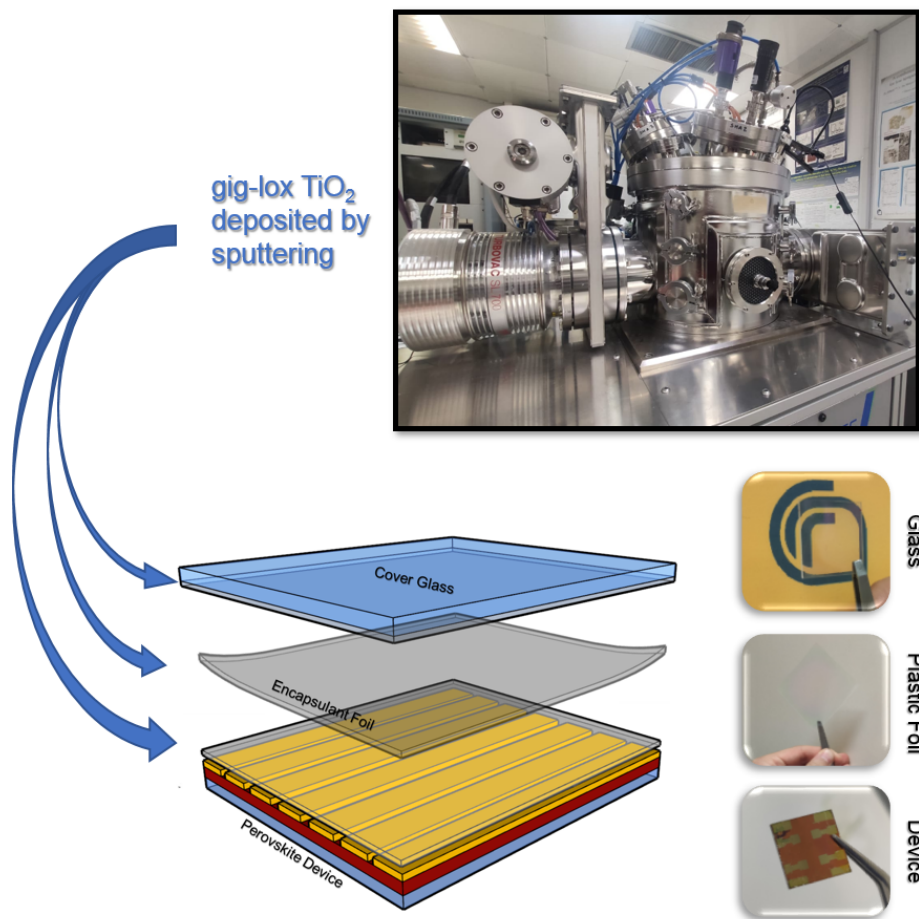


*Figure 4.3. Sputtering equipment used for gig-lox TiO$_2$ deposition and possible schemes for the layer integration on ready-to-use device, glass, and polymeric foil. The arrows indicate the side wherein the oxide can be applied (transparent grey layer in the rendering). Bifacial depositions are also feasible. The pictures on the right panel are taken on proof-of-concept samples immediately after deposition. The gig-lox TiO$_2$ layer deposition is done at RT for the preservation of materials and devices; it also guarantees high surface reactivity and durable capture. The method is at zero-waste production and at zero-solvent use.*

The mechanism of Pb capture by the gig-lox TiO$_2$ layers has been explored at the atomistic level by performing scanning transmission electron microscopy (STEM) analyses. The high resolution and the high atomic mass contrast of the STEM images, coupled with energy dispersive X-ray fluorescence (EDX) spectroscopy done in situ, enabled a detailed study on Pb location and spatial distribution after capture.

The gig-lox TiO$_2$ layer morphology is schematized in the rendering of Figure 4.4a. The layer is composed of columnar mesopores (inlet pipelines for host species), 10-50 nm in diameter (Figure 4.4b), extending through the entire layer thickness and interconnected by a network of branched nanopores with diameters in the range of 1-5 nm[31]. The high magnification STEM images in Figure 4.4c-d show, together with oxide branched structure, that Pb (bright regions) is located on the inner wall surfaces of the oxide nano- and mesopores, decorating the exposed areas of the branches. We further zoomed into them, as shown in the high-resolution image of Figure 4.4e, to disclose that Pb is uniformly and atomically distributed on the pore surfaces. As a matter of fact, brilliant Pb atoms are clearly identifiable in comparison with the Ti-O ordered rows due to the mass contrast (Pb=207.2u, Ti=47.9u). The presence of Pb was further validated by its diagnostic spectra locally acquired by EDX (Figure 4.4f). Based on all those combined findings, we conclude that the extended surfaces of the gig-lox TiO$_2$ layer are (all) available and accessible for effective capture of Pb and that Pb is blocked within an oxide-rich environment.
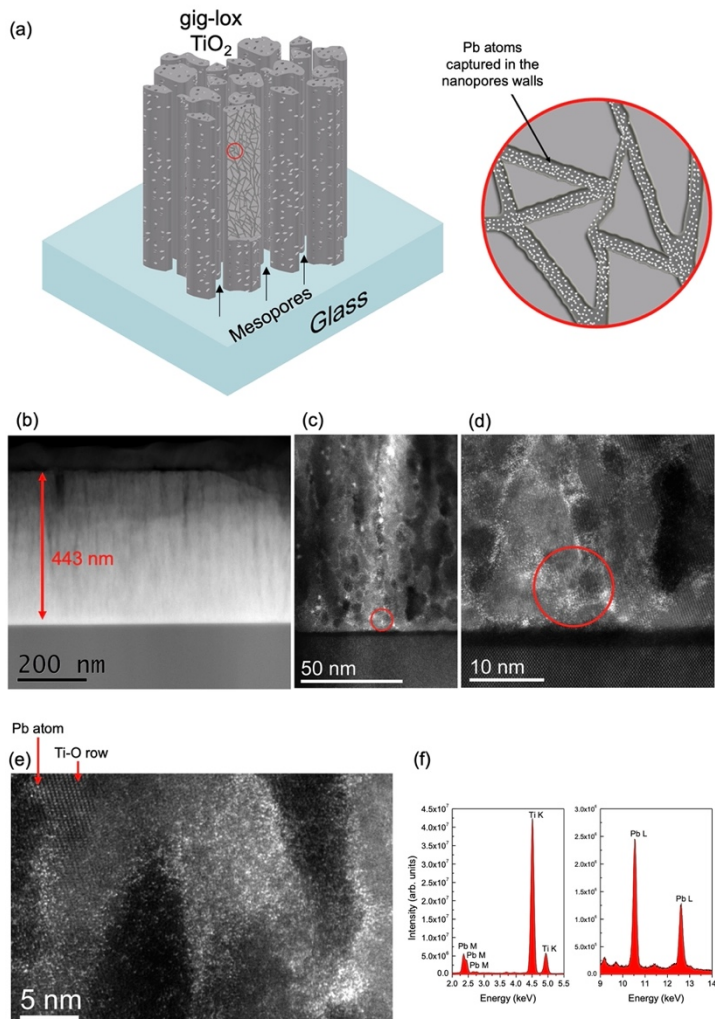
*Figure 4.4 (a) Rendering of the gig-lox TiO₂ nanostructure wherein we highlight the oxide rod structure, the vertical mesopores (indicated by the black arrows), and the inner branched structure of nanopores also connected to the mesopores that serves as inlet pipelines. (b) Cross-sectional STEM image of a 440 nm-thick gig-lox TiO₂ layer, wherein the mesopores have a dark contrast (some of them labelled by vertical arrows). Note that the mesopores cross the entire layer from the interface to the surface. (c-e) STEM image sequence that zooms into the gig-lox TiO₂ sponge after Pb sequestration. Pb is uniformly captured all over the surfaces of the wall of the gig-lox TiO₂ nano and mesopores. Note in (e) the Ti-O rows within the atomic planes taken in high resolution and the brilliant extra-spots that are, instead, Pb captured species. (f) integrated EDX spectrum taken inside the circled area showing L and M shell peaks of Pb along with K shell peaks of Ti.*

We investigate the phenomenon of adsorption of a single Pb atom at the inner surfaces of the gig-lox TiO$_2$ layer with Density Functional Theory (DFT) calculations. Previous experimental findings[31] suggest that the gig-lox TiO$_2$ mainly exposes (101) anatase surfaces, whose degree of order depends on whether they are annealed or not. Therefore, the local stoichiometry at the interior terminations forming the three-dimensional cavities can differ from the perfect 1:2 ratio for Ti:O. Local oxygen or titanium deficiencies can expose vacancy sites where Pb atoms can be adsorbed.

We model the Pb adsorption process taking place at the anatase TiO$_2$ (101) surface (the most stable among low index surfaces[35], named A$_{101}$ hereinafter), considering both the perfect and nonstoichiometric terminations. Figure 4.5a shows a ball and stick model of the A$_{101}$ 4x1 supercell. Our *ab-initio* analysis highlights a strong adsorption interaction of a Pb atom both at the perfect and nonstoichiometric A$_{101}$ in contact with both vacuum or water environment. Stable adsorption configurations are characterized by Pb-O bonds rather than Pb-Ti ones in all cases. This is easily rationalized considering both the +2 and +4 preferential oxidation states of Pb, as well as the relative electronegativity of the involved species which increases going from Ti, to Pb and O. At the perfect A$_{101}$ a Pb atom binds to three outermost oxygens forming three O-Pb bonds (Figure 4.5b) in the same way at the vacuum and at the water interface. The strong interaction between Pb and A$_{101}$ has been quantified by the large adsorption energy (Equation A4.1) of 3.40 eV at the A$_{101}$/vacuum interface and 2.49 eV at the A$_{101}$/water interface (see Table A.4.2). The substitution of Pb with an O1-O8 oxygen atom of the first two O-Ti-O layers, hence modelling the Pb adsorption on an A$_{101}$ surface with an oxygen vacancy, is highly unstable and brings strong local atomic adjustments characterized by the tendency to increase the number of Pb-O bonds. Replacing Pb with titanium, hence mimicking Pb adsorption on an A$_{101}$ surface with a deficit of titanium, induces negligible structural rearrangements (Figure A4.7 and Table A4.3). Among various adsorption sites of the first two O-Ti-O layers at the nonstoichiometric surface, a Pb atom prefers to lie at outermost sites O1 (Figure 4.5c) or Ti1 (Figure 4.5d). Only at the A$_{101}$/water interface, Ti2 is slightly energetically more favorable. Figure 4.5e shows the change of the Kohn-Sham total energy of all O1-O8 optimized configrations of Figure A4.7 with respect to the energy of the O1 adsorption case. Energy differences among the various O1-O8 adsorption sites are on the order of 1-2 eV, indicating a driving force for migration of a Pb atom towards outermost O1 sites (lying at the vacuum or water interface) if initially placed in a subsurface site. Energy differences between various Ti1-Ti4 adsorption sites are below 1 eV, with such differences even below 100 meV in the case of the A$_{101}$/water interface (Figure 4.5f).

The calculations demonstrate the strong tendency of the Pb impurities to segregate at the TiO$_2$ surfaces where stable oxide-coordinated configurations are gained for permanent loading during and after the immersion in water. X-ray Photoelectron Spectroscopy results have provided the experimental evidence on the

chemisorption of lead on the gig-lox TiO$_2$ surfaces based on the coordination with oxygen atoms as shown in Figures A4.8a-b.
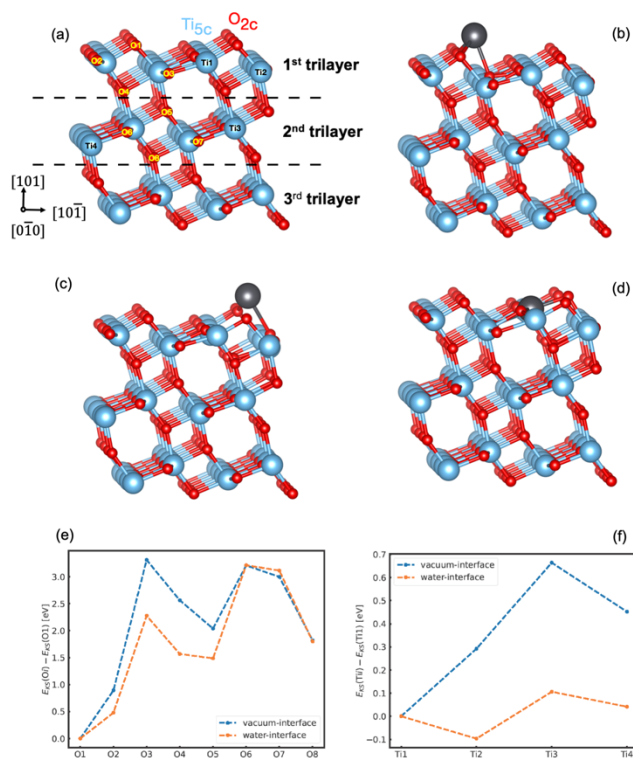


*Figure 4.5 First principle DFT simulations of Pb adsorption on the perfect and nonstoichiometric anatase TiO$_2$ (101) surface under both vacuum and water interfaces. (a) Ball and stick model of the 4x1 supercell for the anatase TiO$_2$ (101) surface (only the first three O-Ti-O layers are shown). The first layer is the outermost in contact with vacuum or water. The atomic numerical labelling supports the identification of initial sites for the Pb adsorption analysis in panels (e-f). (b) Lowest energy adsorption configuration of a single Pb atom on the perfect anatase TiO$_2$ (101) surface. (c-d) Adsorption configurations after a structural optimization starting from the substitution of a Pb atom with an oxygen atom placed at the O1 surface site (c) and a titanium atom placed at the Ti1 surface site (d). (e-f) Kohn-Sham total energy of all adsorption configurations after a structural optimization starting from the substitution of a Pb atom with an oxygen atom placed at the O1-O8 sites (e) and Ti1-Ti4 (f). KS energies in (e) and (f) are calculated with respect to the global minima energy (at the vacuum interface) of O1 (panel c) and Ti1 (panel d) adsorption cases, respectively. The corresponding atomistic configurations are showed in Figure A4.7 of the supplementary information. Energetics are extracted both at the vacuum and the water interface of a nonstoichiometric A$_{101}$. Oxygen: red; titanium: cyan; lead: dark grey.*

Theory and experiments firstly converge to explain the reasons for the stable sequestration of lead and secondly support the cruciality of the pore accessibility and surface reactivity.

In brief, we offer a technologically viable solution to tackle the commercialization of Pb-based perovskites. We demonstrate that Pb leakage is prevented using a TiO₂ sponge for its stable sequestration. With respect to other proposed chemically deposited materials, the TiO₂ sponge is grown without solvents by sputtering, which is an up-scalable methodology well suited to be implemented in the production chain at high throughput. Cost assessment also benefits from the current use of mesoporous TiO₂ layers in most PSC architectures as ETL.

The multi-branched multi-dimensional character of the TiO₂ pores in the sponge and the high surface reactivity, coupled with the pore in-depth accessibility, are the mainstays for effective and durable Pb sequestration. The high degree of interaction between the Pb species and the TiO₂ surfaces explains the permanent stable loading of Pb on the exposed interior surfaces of the porous TiO₂ scaffold.

## Methods

*Chemicals for PSC fabrication:* lead-iodide (PbI₂, ultradry 99.999% metals basis) and methylammonium iodide (CH₃NH₃I, MAI) were purchased from Alfa Aesar (Kandel, Germany) and GreatCell Solar, respectively. 2-hydroxyethyl cellulose (HEC), dimethyl sulfoxide anhydrous, 99.9% (DMSO); toluene anhydrous, 99.8% (TOL); chlorobenzene anhydrous, 99.8% (CB); 2-propanol (IPA); PTAA [poly(bis{4-phenyl}{2,4,6- trimethylphenyl}amine)]; bathocuproine, 96% (BCP) were purchased from Sigma Aldrich; [6,6]-phenyl C₆₁ butyric acid methyl ester (PCBM) was purchased from Nano-c.

*PSC Fabrication and characterization:* Perovskite solar cells based on a p-i-n architecture were realized employing 15x15x1.1 mm ITO (Indium Tin Oxide) patterned glass as substrates and anode, PTAA as hole transporter layer (HTL), MAPbI₃-HEC as a photoactive layer, PCBM as electron transporter material and BCP as hole blocking layer. ITO-glass substrates were cleaned prior to use by ultrasonication baths with deionized water, acetone, 2-propanol, 10 min. at room temperature for each step, and then dried by N₂ flow. PTAA (1.5 mg ml⁻¹ in Toluene), PCBM (25 mg ml⁻¹ in Chlorobenzene) and BCP (0.5 mg ml⁻¹ in 2-propanol) were deposited by spin coating, respectively, with the following parameters: 6000 rpm for 30 sec (100 °C for 10 min of annealing), 1000 rpm for 60 sec (no annealing required), 6000 rpm for 20 sec (no annealing required). MAPbI₃-HEC solution was obtained by solubilizing 0.76 M of PbI₂ and 0.76 M of MAI in DMSO, stirring for 30 min at 80 °C. Next, this solution was added to the HEC powder (11.8 mg of polymer for each ml of MAPbI₃) and stirred for 3 h at 80 °C. 45 μl of cooled MAPbI₃-HEC was deposited on top of PTAA by spin coating at 12000 rpm for 30 sec and washing with

200 µl of Toluene as antisolvent at the $30^{th}$ sec, following 30 min of annealing at 100 °C. All materials were deposited in $N_2$ filled glove box (< 0.1 ppm [O.2], < 0.1 ppm [$H_2O$]). The device stack was completed by the high vacuum ($8x10^{-7}$ mBar) thermal evaporation (Lesker Co. instrument) of 10 nm of Au as anode top electrode with a deposition rate of 0.4 A/s and employing a mask that defined a 0.04 $cm^2$ active area. J-V characteristics were measured by a digital source meter (Keithley model 2401) under AM 1.5-simulated sunlight (100 $mW/cm^2$) from Peccell PEC-L01. The scan range was from −0.1 to 1.2 V for the forward scan and from 1.2 to −0.1 V for the reverse scan with a step of 0.01 V. The delay time was of 0.1 s.

*Gig-lox $TiO_2$ fabrication:* Gig-lox $TiO_2$ layers were deposited on different substrates (glass, silicon, PEN, PSCs) by a grazing incidence geometry using a customized Magnetron DC-pulsed Sputtering equipment fabricated by Kenosistec s.r.l. The flowrate of the carrier gas (Ar) and the reactive gas ($O_2$) is set to 69 and 2 sccm, respectively, in all deposition processes. A pre-sputtering step of 1 min is performed before the deposition process to clean up the surface of the Titanium target to remove oxidised layers. The deposition is done at room temperature using a power of 140 W, a current of 424 mA and a voltage of 330 V (power loading 6.9 W/cm2). The deposition rate is equal to 3.4 nm/min. The thickness of gig-lox $TiO_2$ is regulated by varying the deposition time. Deposition can be done up to 4 inches wafers in our equipment, as shown in a previous paper dedicated to the use of gig-lox $TiO_2$ for environmental gas detection[28] (US patent)[36], with further scale-up feasible in dedicated industrial equipment.

*Absorption coefficient and transmittance measurements:* absorption coefficient and transmittance measurements are collected by using a V-VASE, J.A. Woollam spectroscopic ellipsometer equipped with a monochromator and autoretarder. The AVT is calculated from the arithmetic mean of the 400–800 nm transmittance range.

*Pb-adsorption characterization:* For known Pb concentration aqueous solution, different amounts of $PbI_2$ (Sigma-Aldrich, 99.99% purity) were dissolved in 10 mL of deionized water. 1.25x1.25 $cm^2$ gig-lox $TiO_2$ samples with different thicknesses were soaked in Pb aqueous solutions. Samples were mechanically shaken over the time at 200 rpm with a flat orbital shaker (IKA KS 260 basic). Pb concentrations were determined with an ICP/MS Nexion 300X using the kinetic energy discrimination mode (KED) for interference suppression. Before analysis, samples were diluted, acidified with nitric acid, and added to the internal standards required to determine. Each determination was performed three times. The accuracy of the analytical determination was confirmed by measuring a standard reference material, SRM 1643f - Trace Elements in Water, without observing an appreciable difference.

*STEM and EDX analyses:* Preparation was carried out in a standard mechanical way and final ion milling process on the gig-lox $TiO_2$ sample with the

maximum Pb uptake (soaked in 6.4 ppm Pb water solution for 96 hours). STEM analyses were carried out with a Cs-corrected JEOL ARM200C at 200 keV, equipped with 100mm$^2$ JEOL energy dispersive X-ray (EDX) detector. STEM images were acquired in scanning mode using the HAADF detector. Pb atoms proved to be very stable under electron illumination, despite their atomically dispersed fashion. All the data analysis and elemental quantification were carried out with Gatan Microscopy suite v3.4.

*Density Functional Theory Calculations:* The Kohn-Sham density functional theory (DFT) has been employed within the BigDFT package[37,38], using wavelets as basis functions. Soft norm-conserving pseudo-potentials including non-linear core corrections[39,40] along with the Perdew-Burke-Ernzerhof functional were used to describe the core electrons and exchange-correlation as implemented in the Libxc[41] library. We performed all runs with equivalent parameter settings and convergence criteria. All structures were relaxed using the Hellman-Feynman scheme until forces were less than 5.0 meV/Å.

The lattice parameters of the conventional anatase cell were optimized using a 4x4x2 k-point Monkhorst-Pack grid until the pressure converged below 0.05 kbar, obtaining a cell with lattice constants a = 3.79 Å and b = 9.71 Å. The experimental lattice constants are a = 3.79 Å and b = 9.625 Å [42]. The anatase TiO$_2$ (101) surface was modelled with six layers of a 4x1 supercell (288 atoms in total), starting from the optimized bulk lattice parameters with periodic dimensions of 15.18 Å and 10.43 Å[43]. The first layer is the outermost in contact with vacuum or water. Atoms at the bottom layer were fixed at their bulk coordinates to emulate bulk behaviour. The 4x1 periodicity prevents spurious interactions with periodic images. Surface boundary conditions and a wavelet uniform mesh of $h_{grid} := h_x = h_y = h_z = 0.40$ Bohr have been set for all calculations. Only the Γ point has been used for the k-space integration.

A water environment has been included by means of the soft-sphere implicit solvation model[44,45,46]. When solvent effects are considered, one surface is considered to be in contact with the implicit solvent. For the opposite (bottom) surface, vacuum conditions are always used by setting a large radius of the soft-sphere model for bottom atoms. Water has a relative permittivity of 78.36 at T=20° C[47].The soft-sphere model parameters are reported in Ref.[45].

*XPS analyses:* X-ray Photoelectron Spectroscopy (XPS) spectra were acquired using the K-alpha system of Thermo Scientific, equipped with a monochromatic Al-Ka source (1486.6 eV), operating in a constant analyser energy (CAE) mode with a pass energy of 20 eV for high resolution spectra and a spot size of 400 mm.

*XRR analyses:* X-Ray Reflectivity analyses were done using a D8Discover Bruker AXS diffractometer equipped with a Cu-kα source, a Goebel mirror and a scintillator for detecting the reflected X-ray beam. The critical angle was measured

correspondingly to a penetration depth of ~20 nm in the $TiO_2$ material. This parameter is sensitive to the electronic density of the material within the surface layer.

*Estimation of Pb amount in MAPbI₃ layer:* The $MAPbI_3$ density is assumed equal to 4 g/cm³[48]. The mass percentage of Pb with respect $MAPbI_3$ is 33.4% (207.2u/620u). Considering an area of 1 cm² and a film thickness of 220 nm, the volume of $MAPbI_3$ is ~2.2x10⁻⁵ cm³, with an amount of 29 μg of Pb. Consequently, in 10 ml of water, the Pb concentration is ~2.9 ppm.

*Calculation of Pb sequestration efficiency (SQE):* Pb sequestration efficiency (SQE) is calculated with the following formula:

$$SQE = 1 - \frac{Pb\ leakage\ from\ devices\ covered\ with\ gig-lox\ TiO_2}{Pb\ leakage\ from\ devices\ uncovered}$$

# Appendix

The appendix of this chapter contains supplementary figures, tables and equations. Furthermore, it contains an extended description of DFT calculations methods.
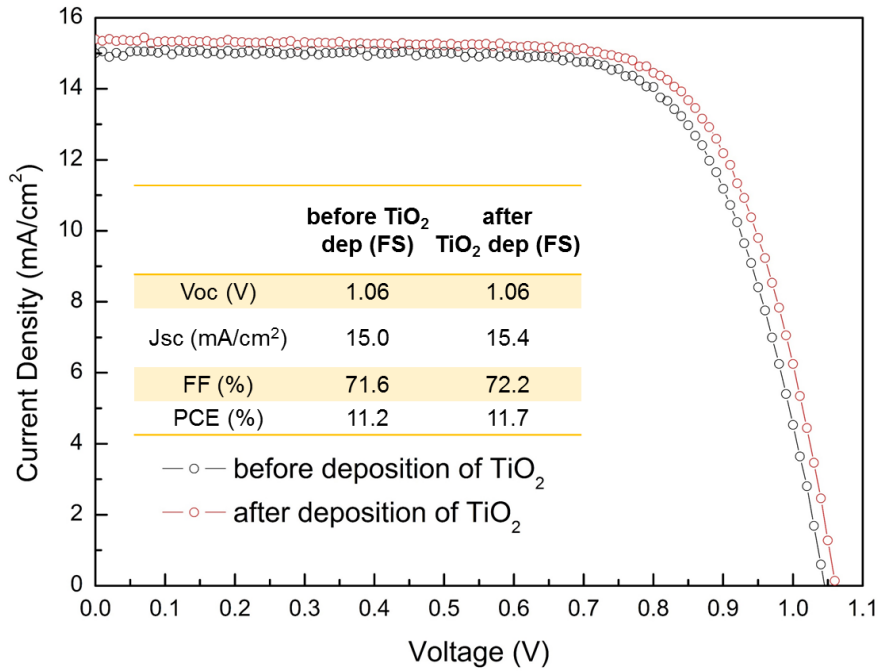


*Figure A4.1 J-V curves taken in forward scan on the same PSC device before and after the deposition of a 340 nm-thick gig-lox TiO₂ layer.*
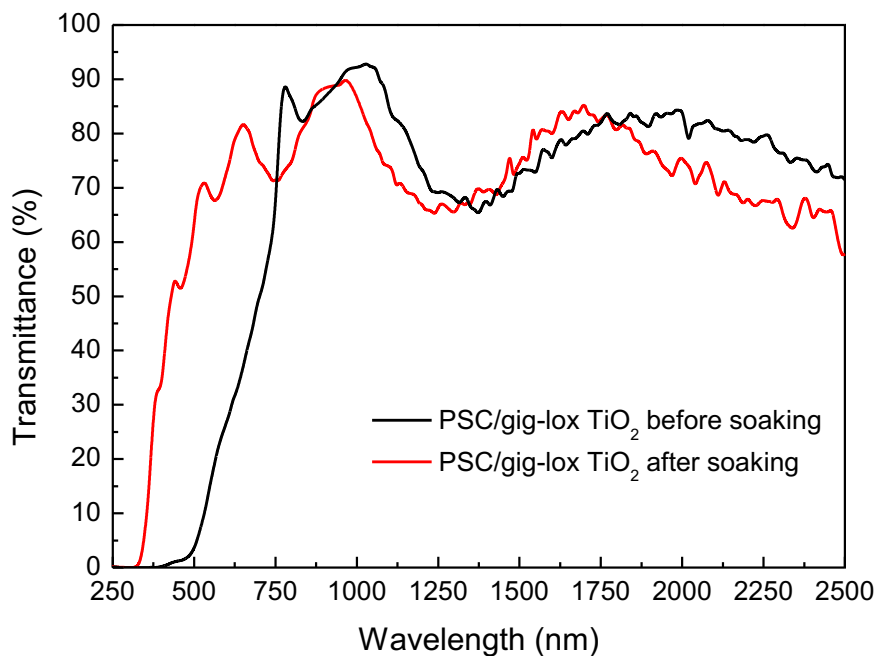
*Figure A4.2 Transmittance vs wavelength of PSC/gig-lox TiO₂ (340 nm) before and after soaking in 10 mL of water. The dissolution of the MAPbI₃ layer is testified by the raised transparency of the sample under 820 nm and by the appearance of the thickness fringes due to the oxide that has a bandgap in the UV as expected.*



*Figure A4.3 Photos of a representative PSC/gig-lox TiO₂ sample before, immediately after soaking and after 10 days of soaking in water (pH ~ 5.8).*

| | PSC w/o gig-lox TiO₂ | PSC/gig-lox TiO₂ (340 nm) Sample #1 | PSC/gig-lox TiO₂ (340 nm) Sample #2 | PSC/gig-lox TiO₂ (340 nm) Sample #3 |
|---|---|---|---|---|
| Pb concentration in 10 mL of water after 10 days soaking (ppb) | 2654.5±13.3 | 311.4±1.6 | 179.0±0.9 | 300.1±1.5 |
| % Sequestration with respect to 2654.5 ppb measured without gig-lox TiO₂ | / | 88.3% | 93.3% | 88.7%. |

*Table A4.1 Pb concentration in 10 mL of water after 10 days soaking (ppb) of device without and with gig-lox TiO₂. The initial calculated amount of Pb into the PSC is 2900 ppb; the one measured after soaking without gig-lox TiO₂ is 2654.5ppb.*
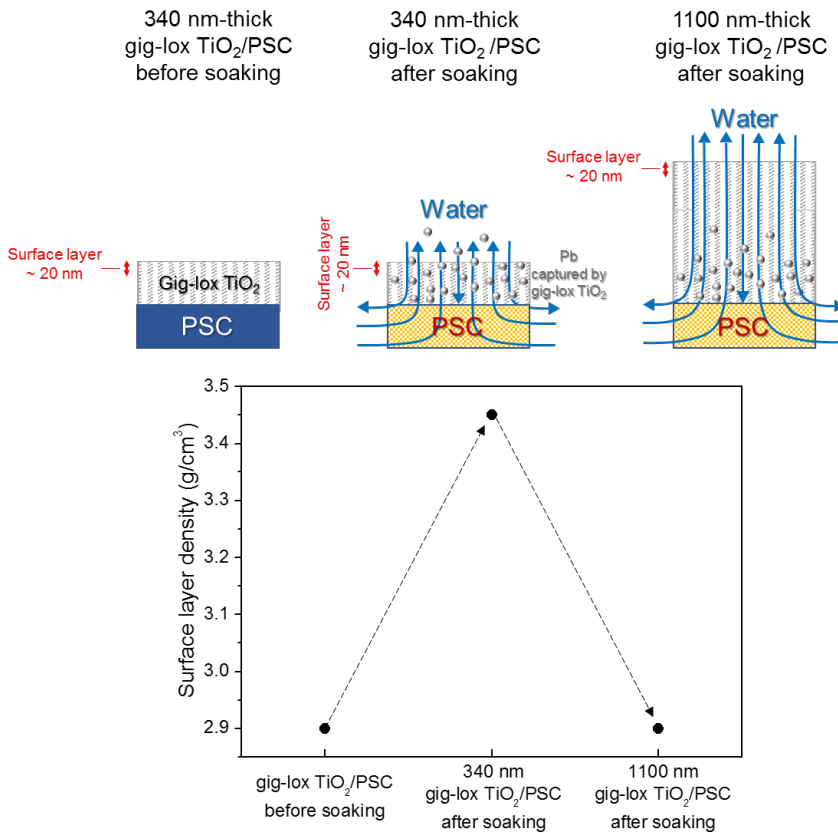
*Figure A4.4 Schematic of 340 nm-thick gig-lox TiO₂ deposited on PSC before and after soaking in water, and 1100 nm-thick gig-lox TiO₂/PSC soaked in water. The density of the upper portion of the gig-lox TiO₂(Pb) surface layer ($\sim$20 nm) is calculated by measuring the critical angle for total external reflection by x-ray Reflectivity (XRR). The density of the 340 nm-thick gig-lox TiO₂/PSC upper layer after soaking is 3.45 g/cm³, higher than the one in gig-lox TiO₂/PSC before soaking (2.90 g/cm³), indicating that the sequestered Pb reaches the TiO₂ surface. In contrast, for 1100 nm-thick gig-lox TiO₂/PSC after soaking, the density of the upper portion is the same of the gig-lox TiO₂/PSC before soaking in water (2.90 g/cm³), and therefore the sequestered Pb has filled a portion of the layer. This finding, joined with the evidence that Pb is not found in water, leads us to argue that the sequestration is a bottom-up process that starts at the interface with the device and proceeds upwards likely assisted by capillary forces.*
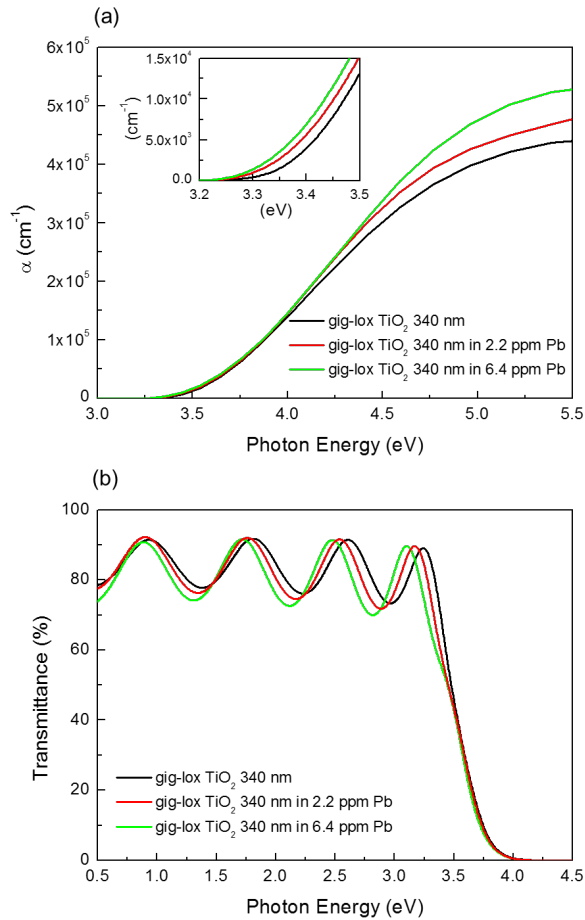
*Figure A4.5 (a) Absorption coefficient and (b) transmittance vs photon energy of 340 nm-thick gig-lox TiO₂ layers before and after soaking in 2.2 ppm and 6.4 ppm Pb water solution. A redshift of the curves is observed when the amount of lead captured by gig-lox TiO₂ increases.*
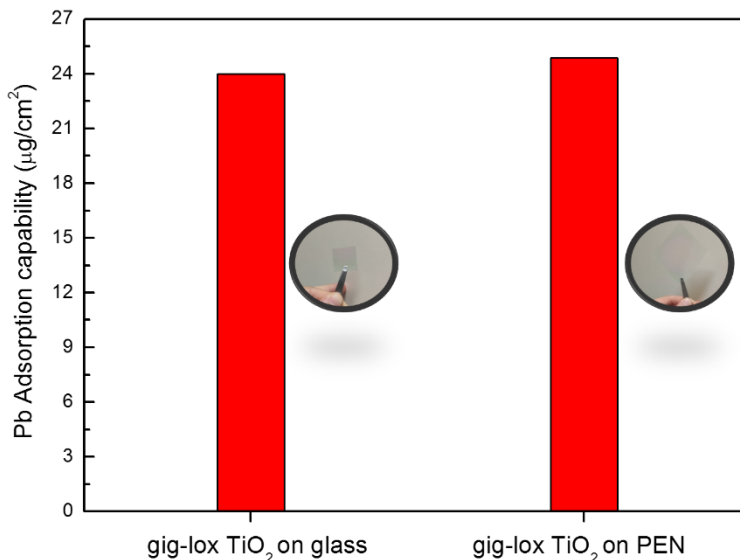
*Figure A4.6 Pb adsorption by 340 nm-thick gig-lox TiO₂ deposited on glass and Polyethylene naphthalate (PEN) foils after 96 hours of soaking in 10 mL of water with a Pb concentration of 6.4 ppm. The adsorption capability of gig-lox TiO₂ is comparable by using different kinds of substrate (~24 μg/cm²).*

### First principle study of lead adsorption

We investigate the adsorption behaviour of a single lead atom at the exposed interior surfaces of the experimentally synthesized multi-scale-porosity (nano and meso) TiO₂ scaffold. Experimental data suggests that the multi-porosity TiO₂ crystallizes in the anatase phase exposing mainly its (101) surfaces. Theoretical calculations reveal the order $\gamma_{(110)} > \gamma_{(001)} > \gamma_{(100)} > \gamma_{(101)}$ for the surface energies of major exposed facets of anatase TiO₂ crystal[49,50]. Thus, the anatase TiO₂ (101) surface (named A₁₀₁ hereafter) turns out to be the most stable among low index surfaces. Most of the anatase TiO₂ micro- and nanostructures reported to date are dominated by {101} facets[51]. As a consequence, to model Pb at the exposed interior surfaces of the multi-porosity TiO₂, we consider the adsorption process taking place at an A₁₀₁ termination. Fig.4.5a shows a ball and stick model of the 4x1 supercell for the anatase TiO₂ (101) surface.

To quantify the interaction between the adsorbed Pb atom and the perfect or nonstoichiometric A₁₀₁ surface, we calculated the adsorption energy as

$$E_{ads} = E_{KS}(Pb) + E_{KS}(A_{101}) - E_{KS}(Pb/A_{101}) \qquad \text{Eq. (A4.1)}$$

Where $E_{KS}$(Pb), $E_{KS}$(A$_{101}$) and $E_{KS}$ (Pb/A$_{101}$) represent the total Kohn-Sham energy of an isolated spherical Pb atom, the (perfect or nonstoichiometric) anatase A$_{101}$ surface, and the Pb/A$_{101}$ system, respectively. The reference systems to compute adsorption energies in vacuum are a slab, an isolated Pb atom and a slab with an adsorbed Pb in vacuum. The reference systems to compute adsorption energies in water are a slab in contact with the implicit solvent, a lead atom immersed in implicit solvent and a slab/liquid interface (liquid described by the implicit model) with an adsorbed Pb. Positive adsorption energy means that the adsorption is exothermic. All energetics refer to the final relaxed structures in the proper environment, that is vacuum or in the presence of water.

### Pb adsorption at the perfect A$_{101}$ surface

First, we inspect the Pb adsorption on the perfect A$_{101}$ surface. For the A$_{101}$/vacuum interface we extracted a surface energy of 0.50 J/m$^2$, in agreement with the value of 0.44 J/m$^2$ reported by Lazzeri et al[52]. To search for the lowest energy adsorption configuration, we performed several structural optimizations starting from various possible adsorption sites of Pb on the anatase TiO$_2$ (101) surface. Fig. 4.5b shows the most stable configuration in which the Pb atom is adsorbed at the A$_{101}$ forming three O-Pb bonds. Pb adsorbs with the same configuration both at the A$_{101}$/vacuum and at the A$_{101}$/water interface. The adsorbed lead atom binds to two O$_{2c}$ atoms lying along the [101] direction, with a Pb-O$_{2c}$ bond length of 2.25 Å, and to one O$_{3c}$ atom with a Pb-O$_{3c}$ bond length of 2.37 Å. This adsorption configuration is slightly different from the most stable adsorption site of a single Ru, Pt or Pd atom approaching the anatase TiO$_2$ (101) surface[53,54,55]. In these latest cases, the lowest energy adsorption configuration is characterized by only two X-O$_{2c}$ bonds (X being a single Ru, Pt or Pd atom) at a bridge site of two edged O$_{2c}$ atoms along the [101] direction. A geometry optimization starting from this surface site is not stable for Pb and ends up to our reported adsorption configuration of Fig. 4.5b.

Our results agree with similar adsorption studies of metals on anatase (101) or rutile (110) TiO$_2$ surfaces[56]. The binding of a metal atom M to a bare and non-defective TiO$_2$ surface involves a formal electron transfer from M to the surface that contributes to the stability of the M–TiO$_2$ system. This makes most often the metal atom a cation which binds to the outermost superficial oxygens.

The corresponding adsorption energy, following Eq. A4.1, is 3.40 eV at the A$_{101}$/vacuum interface (see Table A4.2). This high value suggests a strong interaction between the metallic atom and the titania termination. As expected from the preferential oxidation states of lead, a single Pb atom prefers to bind to oxygen atoms rather than titanium ones. The adsorption energy of Pb at the A$_{101}$ surface is of the same order of that of Ru (3.59 eV)[55], and much larger than that of some metal atoms like Au (0.39 eV)[57], Pd (2.18 eV)[54] and Pt (2.84 eV)[53]. Trends in the adsorption energies for these transition metals agree well with their heat of oxide formation[50].

The adsorption energy of Pb at the $A_{101}$/water interface is 2.49 eV. In this case the Pb atom as well as the outermost O and Ti atoms at the solid/liquid interface interact with the water environment, sharing part of their bonding interaction and valence electrons with the solvent. Nevertheless, the interaction between Pb and $A_{101}$ is still strong, suggesting a permanent loading of Pb on the exposed interior surfaces of the multi-scale-porosity (nano and meso) $TiO_2$ scaffold before and after the immersion in water. Pb loading will take place also during multiple diving of the porous $TiO_2$ in water.

| $A_{101}$ SURFACE | PB-INITIAL POSITION | $A_{101}$/VACUUM | $A_{101}$/$H_2O$ | CONFIG. |
|---|---|---|---|---|
| **PERFECT** | on top | 3.40 | 2.49 | Fig. 4.5b |
| **NONSTOICHIOMETRIC O1 VACANCY** | O1 site | 3.11 | 1.18 | Fig. 4.5c |
| **NONSTOICHIOMETRIC TI1 VACANCY** | Ti1 site | 11.54 | - | Fig. 4.5d |
| **NONSTOICHIOMETRIC TI2 VACANCY** | Ti2 site | - | 10.82 | Fig. A4.7 |

*Table A4.2: Adsorption energies $E_{ads}$ [eV] following Eq. A4.1 of a single Pb atom at the perfect and nonstoichiometric anatase $TiO_2$ (101) surface.*

### Pb adsorption at the nonstoichiometric $A_{101}$ surface

Although the synthesized multi-scale-porosity (nano and meso) $TiO_2$ scaffold is mainly dominated by (101) surfaces, we expect that the complex interior cavities, related to the porous nature of the material and its high specific surface area, expose a variety of superficial local atomic environments. Consequently, the local stoichiometry at the interior terminations forming the three-dimensional cavities can be different from the perfect 1:2 ratio for Ti:O of the anatase $TiO_2$.

Local oxygen or titanium deficiencies can expose vacancy sites where Pb atoms can adsorb. To inspect and quantify this scenario, we simulated the adsorption of a single Pb atom in a nonstoichiometric $A_{101}$ surface characterized by the lack of an oxygen or a titanium atom. In particular, we substituted an oxygen or a titanium atom, lying at an ideal crystal position and belonging to the first two O-Ti-O layers of the 4x1 $A_{101}$ supercell, with a Pb atom and then performed a geometry optimization.

Figure A4.7 shows the configurations after structural optimizations starting from the substitution of a Pb atom with one of the O1-O8 or Ti1-Ti4 atoms. Each panel is labelled with the starting crystal site for Pb. Essentially, we are simulating lead adsorption at a nonstoichiometric surface with a deficit of a single oxygen or titanium atom.
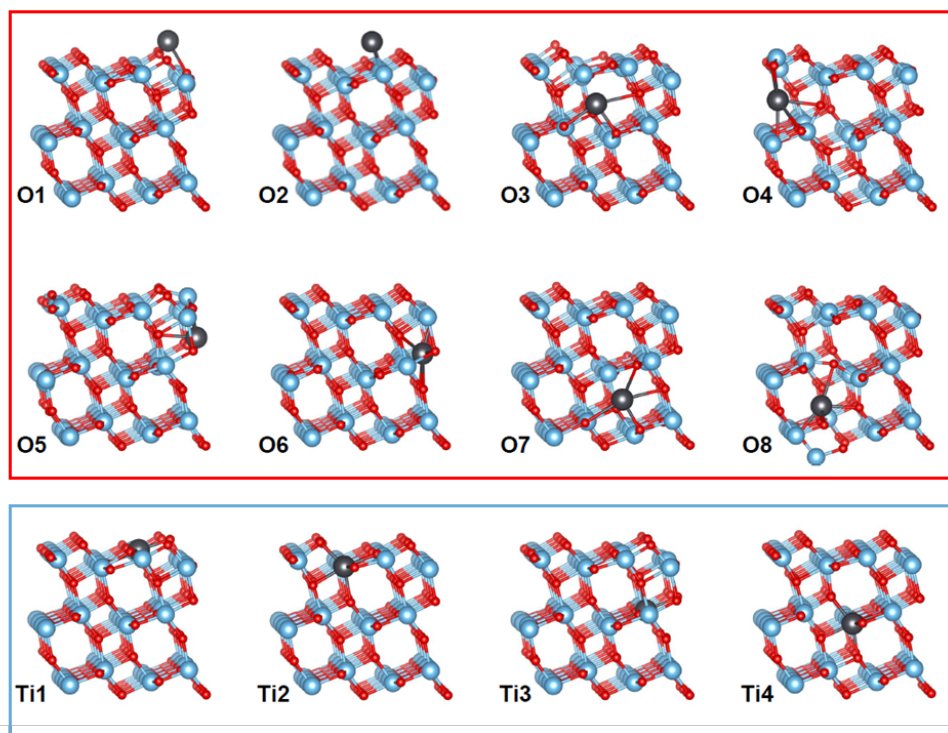


*Figure A4.7 Configurations after structural optimizations starting from the substitution of a Pb atom with various O or Ti crystal surface sites belonging to the first two O-Ti-O layers. Each panel is labelled with the starting crystal site for Pb. Oxygen: red; Titanium: cyan; Lead: dark grey.*

Structural optimizations where Pb is initially placed at an oxygen O1-O8 site are characterized by a strong atomic rearrangement around the adsorbed lead atom. Both the size mismatch between the Pb and O atoms as well as the tendency to form Pb-O bonds play a major role during the structural arrangement. In all cases, Pb moves away from Ti atoms and tries to increase bonds with oxygens. TiO₂ being a highly ionic semiconductor, the local crystal stability is driven by the strength of the Coulombic attraction between its cations and anions. In general, an ionic crystal prefers structures that maximize the number of oppositely charged nearest neighbours for each ion[58].

To quantify such local atomic rearrangement, we report in Table A4.3 the numbers of O and Ti atoms falling in a coordination shell of 2.5 Å around the adsorbed Pb at the end of the geometry optimization (Ti-O bond length for the local octahedral arrangement in bulk anatase is ~ 2.0 Å). Numbers between round brackets refer to the coordination at the starting ideal lattice position. We notice an increase of oxygens bonds in the 2.5 Å coordination shell after all geometry optimizations. Fig. 4.5c and 4.5d show two adsorption configurations after a structural optimization starting from the substitution of a Pb atom with an oxygen atom placed at the O1 surface site (panel c) and a titanium atom placed at the Ti1 surface site (panel d). Fig. 4.5e shows the change of the Kohn-Sham total energy of all O1-O8 optimized configurations of Fig. A4.7 compared to the O1 adsorption case. Among all adsorption configurations, adsorption of Pb at the O1 surface site is energetically more favourable. This well matches with the energetic analysis of oxygen vacancy defects, where surface oxygen vacancies are found to be energetically more favourable than subsurface ones at the $A_{101}$/water interface[59]. The adsorption energy of a Pb atom on such O1 site is 3.11 eV at the $A_{101}$/vacuum interface and 1.18 eV at the $A_{101}$/water, suggesting a strong bond in both cases. Energy differences among the various adsorption sites are on the order of one-two electronvolts, indicating a fast migration of a lead atom towards outermost O1 sites (lying at the vacuum or water interface) if initially placed in a subsurface site.

| $A_{101}$ SURFACE | PB-INITIAL POSITION | O ATOMS | TI ATOMS | CONFIG. |
|---|---|---|---|---|
| **PERFECT** | on top | 2 | 0 | Fig. 4.5b |
| **NONSTOICHIOMETRIC O1 VACANCY** | O1 site | 2(1) | 0(2) | Fig. A4.7 O1 |
| **NONSTOICHIOMETRIC O2 VACANCY** | O2 site | 0(0) | 0(3) | Fig. A4.7 O2 |
| **NONSTOICHIOMETRIC O3 VACANCY** | O3 site | 4(0) | 0(3) | Fig. A4.7 O3 |
| **NONSTOICHIOMETRIC O4 VACANCY** | O4 site | 2(1) | 0(3) | Fig. A4.7 O4 |
| **NONSTOICHIOMETRIC O5 VACANCY** | O5 site | 1(1) | 0(3) | Fig. A4.7 O5 |
| **NONSTOICHIOMETRIC O6 VACANCY** | O6 site | 4(2) | 0(3) | Fig. A4.7 O6 |
| **NONSTOICHIOMETRIC O7 VACANCY** | O7 site | 3(2) | 0(3) | Fig. A4.7 O7 |
| **NONSTOICHIOMETRIC O8 VACANCY** | O8 site | 4(2) | 0(3) | Fig. A4.7 O8 |
| **NONSTOICHIOMETRIC TI1 VACANCY** | Ti1 site | 5(5) | 0(0) | Fig. A4.7 Ti1 |
| **NONSTOICHIOMETRIC TI2 VACANCY** | Ti2 site | 6(6) | 0(0) | Fig. A4.7 Ti2 |
| **NONSTOICHIOMETRIC TI3 VACANCY** | Ti3 site | 6(6) | 0(0) | Fig. A4.7 Ti3 |
| **NONSTOICHIOMETRIC TI4 VACANCY** | Ti4 site | 6(6) | 0(0) | Fig. A4.7 Ti4 |

*Table A4.3 Number of atoms in a coordination shell of 2.5 Å around the adsorbed Pb. Numbers between round brackets refer to the coordination at the starting ideal lattice position.*

The adsorption energy of Pb at the O1 vacancy sites of $A_{101}$/vacuum interface is of the same order as the one of Pd (2.67 eV), Pt (4.87 eV) and Au (3.15 eV).

The scenario drastically changes when Pb replaces one of the four Ti1-Ti4 titanium sites of the first two O-Ti-O layers. This scenario represents a nonstoichiometric surface with a deficit of titanium. Fig. A4.7 shows that structural optimizations in these cases leave the initial configuration almost unmodified. The Pb atom is already in its optimal local environment surrounded by six oxygen atoms (five oxygens only for the most superficial Ti1 site). This can be easily rationalized considering both the +2 and +4 preferential oxidation states of lead, as well as the

relative electronegativity of the involved species which increases going from Ti, to Pb and O. Furthermore, Pb and Ti hold similar atomic size. The numbers of O and Ti atoms falling in a coordination shell of 2.5 Å around the adsorbed Pb in a Ti1-Ti4 site does not change after the geometry optimization (see Table A4.3). Fig. 4.5f shows the change of the Kohn-Sham total energy of all Ti1-Ti4 optimized configurations of Fig. A4.7 with respect to the Ti1 adsorption case. The Ti1 adsorption configuration, showed in Fig. 4.5d, is the energetically most favourable adsorption site at the vacuum interface. However, energy differences between various Ti1-Ti4 adsorption sites are below one eV, with such differences even below 100 meV in the case of $A_{101}$/water interface. The Ti1 adsorption configuration of a Pb atom holds adsorption energy of 11.54 eV at the $A_{101}$/vacuum interface.

When the nonstoichiometric $A_{101}$ interfaces with a water environment, Ti2 is the lowest adsorption site with a binding energy of 10.82 eV. This energetic analysis suggests a strong interaction of Pb at a defective anatase $TiO_2$ (101) surface with a titanium deficit. However, a lead atom can move more easily between various Ti adsorption sites with respect to the case of a nonstoichiometric surface with the presence of an oxygen vacancy. The preference of superficial sites for lead atoms resembles the mechanism of Fe segregation from anatase[60] the Ti interstitial diffusion in rutile to the surface[61] upon annealing in $O_2$.
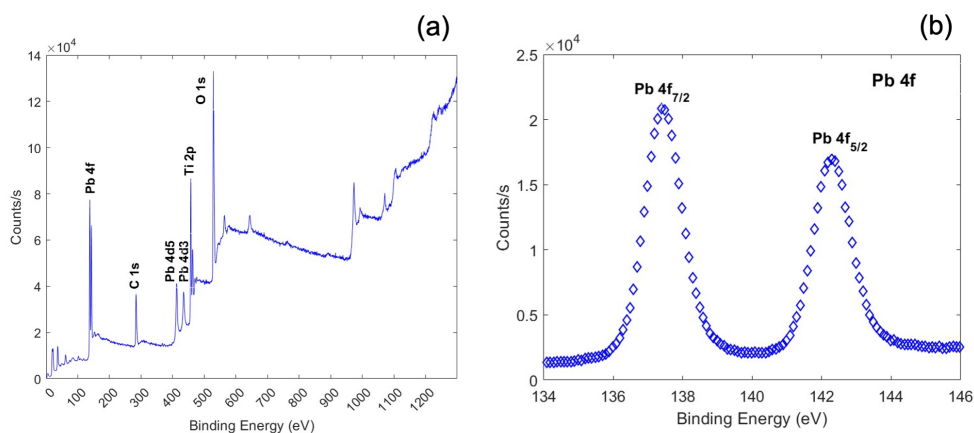


*Figure A4.8: (a) XPS survey spectrum. (b) XPS high resolution spectrum of Pb 4f contribution. X-ray photoelectron spectroscopy (XPS) analysis have been carried out to investigate the surface composition and chemical configurations. Figure A4.8 shows the survey spectrum of the sample. C (32.9%), O (49.5%), Ti (12.6%) and Pb(5.0%) atomic species have been detected. The high-resolution spectrum of Pb4f, is characterized by two peaks centred at 137.4 and 142.3 eV (the binding energy difference is 4.9 eV). These features are related to the 4f7/2 and 4f5/2 signal. The position of the two peaks are commonly attributed to $Pb^{4+}$, associated with the presence of oxidated lead.*

# References

[1] M.V. Khenkin et al. *Nat Energy* 2020, 5, 35–49

[2] S.H. Reddy et al. *Adv. En. Mat.* 2022, 12, 2103534

[3] Li, J. et al. *Nat Commun* 2020, 11, 310

[4] C. Ponti et al. *Trends in Ecology & Evolution* 2022, 37, 281-283

5 S. Gorjian et al. *Renewable and Sustainable Energy Reviews* 2022, 158, 112126

[6] T.M. Koh et al. *Adv. Mater.* 2022, 34, 2104661

[7] M. Pitaro et al. *Adv.Mater.* 2022, 34, 2105844

[8] X. Jiang et al. *J. Am. Chem. Soc.* 2021, 143, 10970–10976

[9] J. Sanchez-Diaz et al. *Joule* 2022, 6, 861-883

[10] Y. Jiang et al. *Nat. Energy* 2019, 4, 585-593

[11] V.K. Ravi et al. *ACS Omega* 2020, 5, 29631–29641

[12] X. Li et al. *Nature* 2020, 578, 555-558

[13] S. Chen et al. *Nat. Energy* 2020, 5, 1003-1011

[14] S. Chen et al. *Nat. Sustain.* 2021, 4, 636-643

[15] J. Lee et al. *Adv. Energy Mater.* 2020, 10, 1902662

[16] X. Li et al.*Nat. Sustain.* 2021, 4, 1038–1041

[17] C.J. Clarke et al. *Chem. Rev.* 218, 118, 747–800

[18] A. Albini and S. Protti. The Solvent Issue. In: Paradigms in Green Chemistry and Technology. SpringerBriefs in Molecular Science(). Springer, Cham. 2016

[19] J.D. Chea. *Ind. Eng. Chem. Res.* 2020, 59, 5931–5944

[20] D.E. Giammar et al. *Environmental Engineering Science* 2007, 24, 85-95

[21] X. Zhao et al. *J. Chem. Eng. Data* 2010, 55, 4428–4433

[22] P. Liang et al. *Anal. Chim. Acta* 2001, 440, 207– 213

[23] S. Lee et al. *J. Ind. Eng. Chem.* 2013, 19, 1761–1769

[24] T.J. Jacobsson et al. *Nat Energy* 2022, 7, 107–115

[25] M. Kim et al. *Science* 2022, 375, 302-306

[26] S. Seo et al. *ACS Energy Lett.* 2021, 6, 3332–3341

[27] A. Alberti et al. *ACS Appl. Energy Mater.* 2019, 2, 6218–6229

[28] A. Alberti et al. *Sens. Actuators B: Chem.* 2018, 259, 658-667

[29] E. Smecca et al. *Chemosensors* 2019, 7, 12

[30] S. Sanzaro et al. *J. Mater. Chem. A* 2017, 5, 25529-25538

[31] S. Sanzaro et al. *Sci Rep* 2016, 6, 39509

[32] S. Sanzaro et al. *Nanomaterials* 2019, 9, 1300

[33] F. Bisconti et al. *Nano Energy* 2021, 89, 106406)

[34] G. Giuliano et al. *Sol. RRL* 2021, 5, 2100702 (2021)

[35] U. Diebold etThe Surface Science of Titanium Dioxide. *Surf. Sci. Rep.* **48**, 53-229 (2003)

[36] A. Alberti, et al. US patent n°10871462B2, granted on 2020-12-22

[37] L.E. Ratcliff et al. *J. Chem. Phys.* 2020, 152, 194110

[38] BigDFT software package. http://www.bigdft.org, (last access: 23-02-2022)

[39] S. Goedecker et al. *Phys. Rev. B* 1996, 54, 1703-1710

[40] A. Willand et al. *J. Chem. Phys.*2013, 138, 104109

[41] M.A. Marques et al. *Comput. Phys. Comm.* 2012, 183, 2272-2281

[42] K.M. Reddy et al. *Mater. Chem. Phys.* 2003, 78, 239-245

[43] G. Fisicaro et al. *J. Phys. Chem. C* 2020, 124, 2406-2419

[44] G. Fisicaro et al. *J. Chem. Phys.* 2016, 144, 014103

[45] G. Fisicaro et al. *J. Chem. Theory Comput.* 2017, 13, 3829-3845

[46] O. Andreussi, and G. Fisicaro. *Int. J. Quantum Chem.* 2019, 119, e25725

[47] F. Buckley and A.A. Maryott. Tables of Dielectric Dispersion Data for Pure Liquids and Dilute Solutions; U.S. Dept. of Commerce, National Bureau of Standards, pp 6-8 (1958)

[48] H. Wei and J. Huang. *Nat Commun* 2019, 10, 1066

[49] M. Lazzeri et al. *Phys. Rev. B* 2001, 63, 155409

[50] U. Diebold. *Surf. Sci. Rep.* 2003, 48, 53-229

[51] M. Liu et al. *Chem. Commun.* 2010, 46, 1664-1666

[52] M. Lazzeri et al. *Phys. Rev. B* 2002, 65, 119901

[53] Y. Han et al. *J. Phys. Chem. B* 2006, 110, 7463-7472

[54] J. Zhang et al. *J. Phys. Chem. C* 2008, 112, 19506-19515

[55] S.-T. Zhang et al. *J. Phys. Chem. C* 2014, 118, 3514-3522

[56] Z. Helali et al. *Theor. Chem. Acc.* 2015, 134

[57] A. Vittadini and A. Selloni. *J. Chem. Phys.* 2002, 117, 353-361

[58] S. Na-Phattalung et al. *Phys. Rev. B* 2006, 73, 125205

[59] G. Fisicaro et al. *J. Phys. Chem. C* 2020, 124, 2406-2419

[60] M. Setvín et al. *Surf. Sci.* 2014, 626, 61-67

[61] S. Wendt et al. *Science* 2008, 320, 1755-1759

# Chapter 5: Perovskite deposition methods for clean and up-scalable manufacturing

*In this chapter, technologically affordable, reproducible and up-scalable processes for perovskite layer deposition based on in-vacuum methods will be commented in the light of their environmental and economic sustainability. Two different physical deposition methods will be described and complemented by a cost evaluation for industrial scale production: high-vacuum physical vapour deposition (HV-PVD) processes vs. a newly conceived low-vacuum proximity space effusion (LV-PSE) method. HV-PVD for MAPbI₃ deposition was employed for the first time in 2013 by Snaith et al.[1] The LV-PSE process has been recently published in the Journal of Materials Chemistry A (Smecca et al. 2021, 9, 16456-16469).*

## 5.1 Low Vacuum-Proximity Space Effusion (LV-PSE) method for MAPbI₃ deposition

Physical Vapor Deposition (PVD) methods for perovskite fabrication are suitable to boost industrial throughput and to afford up-scalability. They are less investigated than chemical methods despite some prestigious seminal works[1,2,3,4,5]. A reason could be the cost of the initial investment for the equipment and the minor versatility. Those seminal papers demonstrated how hybrid organic-inorganic perovskite films prepared by co-evaporation exhibit higher stability and performances with respect to films prepared by wet chemical approaches (e.g. spin coating) due to a better control of the PSK quality. For this reason, quite recently, many research groups have started investing on PVD equipment worldwide.

PVD deposition enables conformal coverages on rough surfaces (e.g. textured TCO) for the benefit of a tight material coupling that, at the same time, preserves the initial morphology of the substrate. Together with the conformity and the lack of solvent, another advantage of perovskite purely deposited by physical methods is a very low roughness and the possibility to scale down the thickness while maintaining uniformity and compactness. Scaling the perovskite thickness increases transparency in the visible range for application in semi-transparent solar cells (BIPV, BAPV and Agrivoltaics).

Usually, PVD chambers work by co-evaporating the precursors from inorganic (e.g. PbI₂) and organic (e.g. MAI) powders under high-vacuum (HV) conditions in the range $10^{-5}$ - $10^{-7}$ torr [6]. Due to the range of pressure used, the

method is hereinafter called HV-PVD[7]. Another feature of the method is the source-substrate distance in the range of tens of centimetres (e.g 20 cm [8] or 30 cm [23]) (left panel in figure 5.1) The parameters that can be tuned during the deposition process are: 1) the temperature of the substrate and 2) the temperature of the crucibles containing the precursor powders. In a recent paper[9] the role of the MAI vapor pressure is highlighted as pivotal in compensating for low stitching coefficients causing desorption of the species. Typical deposition rates for perovskites are in the range 3-6 nm/min [5,23].

Optimizing the deposition process is tricky, firstly due to the low-energy species landing on the substrate and secondly due to a large spread of the organic precursors (e.g. MAI) as the species leave the crucible[10]. This causes them to distribute through the chamber with impact on reducing deposition rate. As collateral effect, cross-contaminations on the quartz microbalance make difficult a fine parameter control. Lastly, frequent refilling of the sources with the organic precursors is needed.

Investment and maintenance costs of high vacuum chambers are high. Material waste over the chamber walls is detrimental for costs and demands frequent maintenance. On the other hand, if the pressure in the evaporation chambers was increased (low vacuum conditions), the deposition rate would be drastically decreased due to the augmented collisions of the sublimated species during traveling (right panel in figure 5.1). To exploit low vacuum depositions, deposition chamber design and processes must be reviewed. Smecca et al.[11] have recently proposed a method called LV-PSE (Low-Vacuum Proximity Space Effusion) to sequentially deposit both the Lead-halide and the organic moieties in the same chamber at the pressure of a low-vacuum primary pump to produce $MAPbI_3$ films. The mainstay of the method resides in the use of a relatively high working pressure $\sim 10^{-2}$ mbar coupled with a substrate-source coaxial geometry at distance of 1-3 cm (Figure 5.1, central panel).
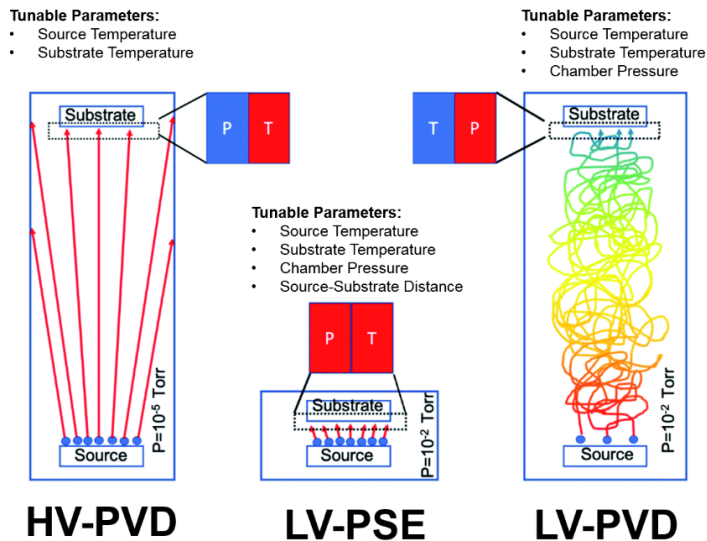
*Figure 5.1 Different physical vapour methods for perovskite deposition by varying chamber pressure and source-substrate distance. The red used to represent a deposition parameter indicates relatively high values with respect to those indicated in blue. (Ref. [11]. Creative Commons License CC BY 3.0[12])*

The combination of short distances and high pressures upsets proper kinetic properties of the species impinging on the substrate with respect to standard HV-PVD with a major impact on the material quality. As a further effect, the number of available sensible parameters is increased by 2 with respect to HV-PVD. In LV-PSE processes, in fact, the chamber pressure and source–substrate distance become additional parameters to control and boost the material quality.
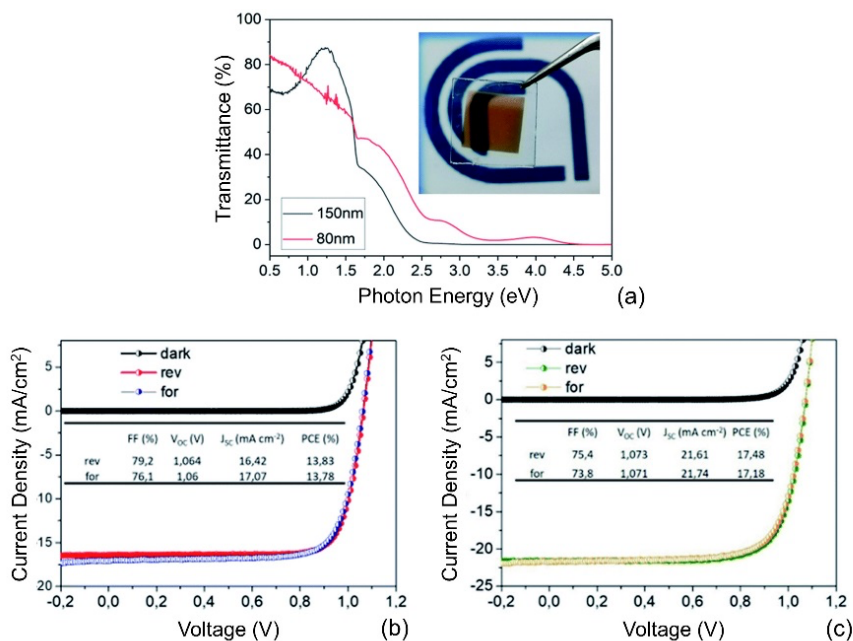
*Figure 5.2 a) Transmittance vs photon energy of 80 nm and 170 nm-thick MAPbI₃ deposited by LV-PSE method. J-V curves of PSCs with 80 nm (b) and 170 nm-thick MAPbI₃ (c).(Ref. [11]. Creative Commons License CC BY 3.0[12])*

Their tunability lastly allows downscaling the thickness of the perovskite layers while keeping the photovoltaic performances. In addition, the method is at quasi-zero loss of materials at the chamber walls to restrain investment and operation costs. The experimental and theoretical optimal values for the growth rate of $PbI_2$ films have been currently achieved at $T_{substrate}=120$ °C and a source-substrate distance of 2 cm. The temperature for $PbI_2$ sublimation is 350 °C. For the MAI deposition step, a temperature of 135 °C is applied to the crucible and the deposition time is optimized to reach the right stoichiometry and to avoid presence of residual $PbI_2$ on the sample. The $T_{substrate}$ during MAI deposition is 75 °C. In the paper by Smecca et al.[11], two different thicknesses of material have been integrated in inverted architecture made of $ITO/PTAA/MAPbI_3/PCBM/Al$, i.e. 170 nm and 80 nm obtained by varying the deposition time of $PbI_2$ and MAI. The 170 nm layer, characterized by an Average Visible Transmittance (AVT) as high as 20%, produced a record efficiency of 17.48%. To our knowledge, it is the best efficiency achieved at such a low thickness. Considering the transparency vs. efficiency trade-off, the result indeed testifies the high quality of the deposited material. In the case of 80 nm-thick MAPbI₃ layers, the devices showed an average efficiency of 12.9% withstanding an AVT of 32.8%.

The AVTs and J-V curves with the photovoltaic parameters of the two thickness of MAPbI$_3$ are shown in figure 5.2a-b-c. The downscaling of the deposited perovskite layer thickness to values <200 nm is mandatory to gain transparency. At the same time, defect mitigation in high quality layers is needed while scaling down to guarantee transparency. Transparency is featured through the absorption coefficient and the penetration depth of incident light. The combination of the two parameters measured in LV-PSE perovskites highlights that, even in relatively thin layers, the absorption capability above the bandgap is still high: 60% of incident photons with energy under 2 eV are absorbed within the first 20-100nm in the MAPbI$_3$ layer; photons with energy in the range of energy 1.5-2 eV are absorbed within 100-200 nm with indeed only a partial loss of absorption that, on the other hand, assures semitransparency as shown in figure 5.3a and 5.3b. In this scenario, deposition of perovskite by LV-PSE is ideal for BIPV, BAPV and Agrivoltaics applications.
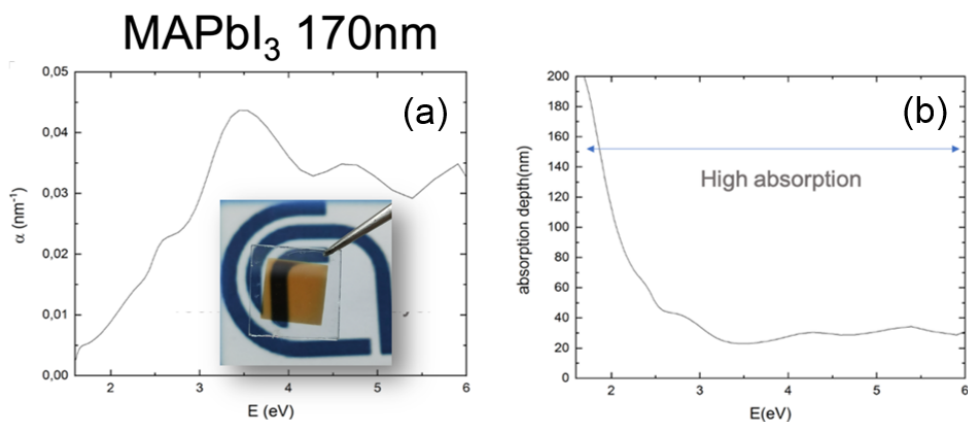


*Figure 5.3 a) Absorption coefficient and b) absorption depth vs. photon energy for 170 nm-thick MAPbI$_3$ samples deposited by LV-PSE. (Ref. [11]. Creative Commons License CC BY 3.0[12])*

## 5.2 Economic evaluation on the industrial manufacturing of perovskites: description of the analytical method

In this paragraph we introduce the approach for a comparative evaluation on the Economically Sustainable Growth of the Industrial Manufacturing of Perovskites by HV-PVD and LV-PSE. We moved from the forecast of Allied Market Research report[13] that states physical vapour deposition of perovskites on rigid modules (glass) and flexible foils to become the most lucrative segment by 2030, with expectation to grow at the highest Compounded Average Growth Rate (CAGR) of 32.9% compared to pure solution and vapour-assisted solution methods.

For the comparative evaluation, we followed the pathway signed by a paper published by Matthews et al.[14] The method focuses on the influence of economies of scale and average selling price on profitability. It consists of a bottom-up technoeconomic model which investigates the sustainable growth of perovskite manufacturing for a R2R single-junction technology, analysing the impact of factory sizes (ranging from 0.3 MW/year to 1 GW/year) and selling price (3.30$/W to 0.53$/W).

The route towards the market success of perovskite technologies has not been marked out yet. Potentially, perovskites can be integrated as active layer in any PV application but, it is undoubted that its application in large utility-scale solar plants or farms as alternative of well-consolidated silicon technology is not reasonably viable. As a matter of fact, the silicon PV manufacturers drive down prices by producing very-low-cost (0.25 €/W[15]) modules at the GW/year scale (mainly produced in low-labour costs countries like China) making hard the entrance of new solar technologies as competitors in the market. Thus, perovskite competition with silicon in this market segment is not a strategic point. Other alternative choices can, instead, find the right placement in the market. One is the alliance with silicon, by integrating PSC on top of SSC working in tandem such to increase the power conversion efficiency (actual record of 31.3% for small-area device[16]) in large utility-scale solar plants. A second opportunity is entering niche markets where the perovskite works better than silicon as for Internet of Things (IoT), building-integrated or applied photovoltaics (BIPV, BAPV), Telecommunications, Automotive, Agrivoltaics. In those market share, the selling price of energy can be higher (>1€/m$^2$) allowing higher margins of profit. This seems to be a rational solution allowing to fully exploit the enormous potential of this technology.

IoT applications, for example, take advantage from the high in indoor PCE of ~40%[17] (Silicon achieves an efficiency of ~20%)[18]. Currently, the only commercialized perovskite-based products are Electronic Shelf Labels for indoor application to be used in shops and supermarkets designed by the Polish company Saule[19].

BIPV, BAPV, Automotive and Agrivoltaics segments demands to high quality semi-transparent perovskite layers as targeted through LV-PSE processes.

## 5.3 Economic evaluation on the industrial manufacturing of perovskites: LV-PSE vs HV-PVD

The objective of this paragraph is to compare the economic feasibility of the perovskite industrial manufacturing by HV-PVD and LV-PSE for different production capacity. The factory capacity is strictly related to the targeted market and to the throughput of the deposition technique (m$^2$/hours).

We assume to produce flexible solar cells on PET/ITO substrates with the following stack PET/ITO/ZnO/MAPbI$_3$/PEDOT:PSS/Ag (figure 5.4a), as reported in ref.[14], with a photoconversion efficiency of 18%. In the set-up and related calculations, we substitute the step of perovskite deposition by chemical slot-die coating with the physical deposition by HV-PVD or LV-PSE, and this is the only change made in the whole production chain. All the other layers in the solar device architecture (ETL, HTL and electrode) are assumed to be produced in the same way and at the same costs in the two methodologies by chemical slot-die coating methods. In the flow-chart, the PSCs are lastly encapsulated by barrier plastic foils. The prices of the materials are those reported by Chang et al.[20].

The selling price is fixed to 3.3 €/W which is an acceptable value for BIPV, BAPV and Agrivoltaics applications[21] considering the semi-transparency achievable by the perovskite technology. We discriminate between fixed costs (Investment in facility & equipment and investment in building), variable costs (Electricity, maintenance, spare parts, labor, materials) and additional costs. The last ones include the cost to purchase the buildings and facilities, labor for tool operations, tool maintenance including capital and labor expenses, facility and tool electricity usage, R&D expenses and selling, and general and administrative expenses (SG&A). All the parameters used in the financial evaluation are reported in Table A5.1 in Appendix.

For both HV-PVD and LV-PSE, we initially assume that each production line can fabricate simultaneously three 21x21 cm$^2$ mini-modules. We suppose to obtain a uniform perovskite deposition on those area in terms of thickness and quality of material for both methods assuming to reach a module efficiency comparable to that of small-area devices. As a first approximation, the deposition rate of MAPbI$_3$ deposited by the two different methods is assumed to be comparable[5,11,22,23,24]. However, this is a conservative assumption since the deposition rate of LV-PSE method is expected to become notably higher than that of HV-PVD method.

In the literature on conventional HV-PVD, the usual thickness of MAPbI$_3$ applied to achieve 20% efficiency in small-area device is ~800 nm[23,24]. The smallest thickness of MAPbI$_3$ deposited by HV-PVD found in the literature is currently ~350 nm, with the device reaching an efficiency of ~16%. For our evaluation, we fixed a MAPbI$_3$ thickness of 350 nm for HV-PVD devices assuming to reach an efficiency of 18%. In contrast, depositing MAPbI$_3$ layer through LV-PSE method, 18% of efficiency can be reached with thinner layers of 170 nm, thanks to the fine control on thicknesses with high lattice quality and low defects. This is a remarkable result which influences the factory throughput and, consequently, the initial investment. As matter of fact, assuming the same number of production lines for the two methods and being the active layer thickness in LV-PSE halved with respect that in HV-PVD, the solar module production (m$^2$/h) in LV-PSE is twice compared to HV-PVD. Thus, to reach the same production capacity of LV-PSE, the number of lines in HV-PVD needs to be doubled. In addition, an equipment cost of 400 k€ for the single production line for

LV-PSE[25] is assumed while for HV-PVD a price rise by 30% is calculated that makes the investment for a single deposition station to be 520 k€ [25]. The major cost of HV-PVD is mainly due to: 1) high-vacuum pumps vs. low-vacuum pumps, 2) the chamber volume in HV-PVD (source-substrate distance ~20 cm) which is higher than in LV-PSE (source-substrate distance ~2 cm), with increasing cost for chamber materials/fabrication and specific protective coverages. Furthermore, the larger source-substrate distance in HV-PVD causes the dispersion of highly volatile organic precursors in the whole chamber including on its walls, with cross-contamination risks and high material waste. This implies: 1) additional maintenance to clean the inner surfaces of the chamber; 2) the rapid depletion of the powders in the crucibles and their periodic refilling (after each deposition in the worst case[26]). To do this, the deposition chamber needs to be opened, increasing machine downtime, and consequently decreasing the factory throughput. Moreover, the frequent recycle of lead from the various surfaces adds procedural complexity and is costly. All those issues are intrinsically avoided or drastically mitigated by LV-PSE, making it a more sustainable method.

In the model we used for the economic evaluation, as a side effect of the higher initial equipment cost in HV-PVD, maintenance and spare parts costs are raised by 20% and 30%, respectively, with respect those of LV-PSE[25]. The remaining costs related to the deposition of the other layers (ETL, HTL, electrodes and encapsulant) and to the module performances tests are, for simplicity, assumed independent of the deposition methods.

Figure 5.4b shows the step-by-step module production cost contributions along with the comparison between HV-PVD and LV-PSE for a production capacity of 10 MW/year.

As expected, the main part of the production costs is ascribable to the layer deposition and, in particular, to the initial investment on the deposition equipment and relative maintenance/spare parts. In this context, labour, materials cost and investment on building have negligible effect. The encapsulation, the purchase of ITO/PET foils and relative patterning have an important role in the final production cost.

Under all those approximations and evaluations, we have simulated different scenarios to predict output, mimicking volumes suitable for start-up (<1 MW/year) and for industry scale (up to 100 MW/year) by progressively increasing the number of lines. The economic viability is evaluated in terms of 1) equipment cost which drives the initial investment (M€) 2) production cost (€/m$^2$) which considers all the above mentioned fixed and variable costs and 3) operating margin (%) that measures how much profit a company makes as percentage of the revenue. Figure 5.5 displays those parameters depending on factory capacity.
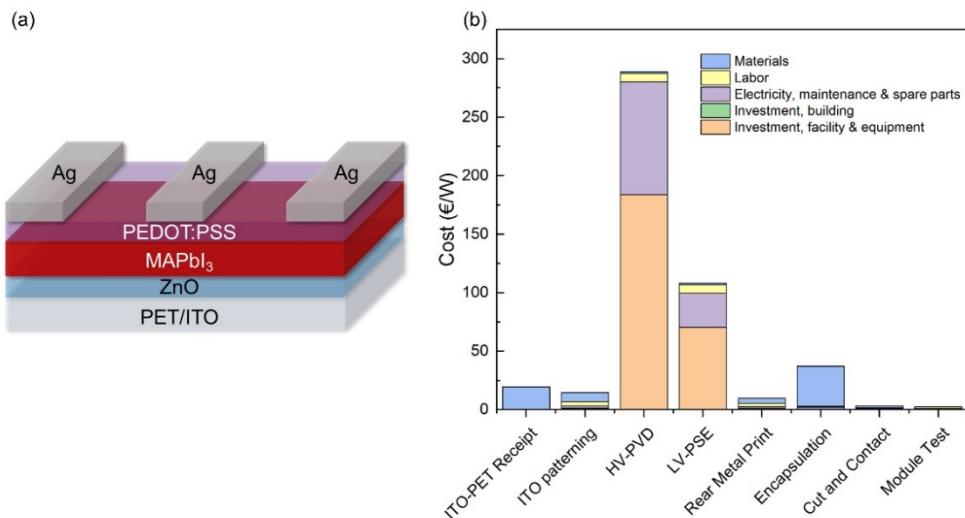
*Figure 5.4 a) Schematic of the PSC architecture used for the economic evaluation. b) Step-by-step module production cost contributions with the comparison between HV-PVD and LV-PSE for a production capacity of 10 MW/year.*

In general, as expected, LV-PSE equipment cost is estimated to be ~2.5 times lower than HV-PVD and this reflects on the production cost of the module which is systematically lower (~1.5 times than HV-PVD) and on operating margin and profits (~ 4 times higher than HV-PVD).

As additional note of merit, by using LV-PSE method, profits are generated (operating margin>0) starting from low production output (0.25 mW/year) and with a low initial investment for equipment (800 k€). In contrast, HV-PVD method begins to generate profits for higher volumes of production (1.8 MW/year), needing an initial investment of 9 M€. This finding makes LV-PSE further appetible for perovskite-based photovoltaics manufacturing in start-up with low factory output.
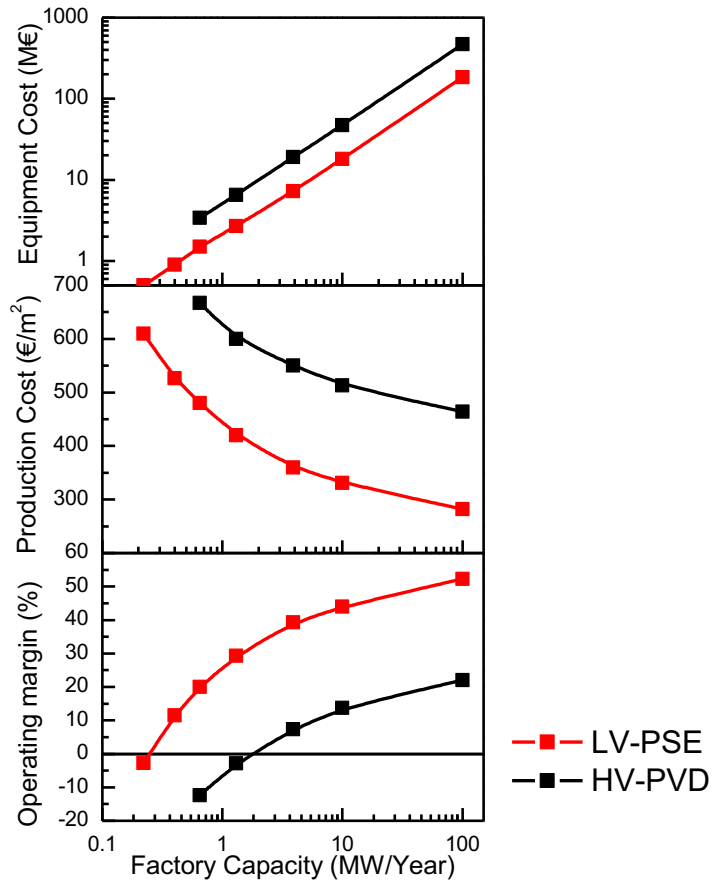
*Figure 5.5 Equipment cost, production cost and operating margin vs factory capacity*

# Appendix

The appendix of this chapter contains a table which lists all the parameters used in the financial evaluation.

| Category | Item | Units |
|---|---|---|
| *Efficiency* | Efficiency of solar panel | % |
| *Utilities* | Electricity Cost | €/kWh |
| | Electricity for services | kWh / tool kWh |
| *Building related* | Building cost per m$^2$ | €/m$^2$ |
| | Floor ratio | total / footprint |
| | Building and facility maintenance rate | % of capex per year |
| *Labor* | Operator cost | €/h |
| | Indirect labor cost ratio | |
| | Maintenance technician cost | €/h |
| *Depreciation* | Facility & equipment | years |
| | Building | years |
| *Factory Output* | Factory Capacity | MW/year |
| | Selling Price | €/W |
| | Yield per step | [%] |
| | Factory Max Possibe Output | m$^2$/year |
| | Factory Uptime | [%] |
| | Factor Annual Output | m$^2$/year |
| | Factory throughput | m$^2$/hour |
| | Tool Scaling Factor | |
| | Tool Cost Scaling Factor | |
| | Factory Production Capacity (MW/year) | MW/year |
| *Materials Purchase (Portion of 1 year)* | ITO coated PET | m$^2$ |
| | resist, etch chemicals | g |
| | ZnO Nanoparticles | g |
| | PEDOT:PSS | mL |
| | IPA | mL |
| | Nitrogen | m$^3$ |
| | PbI$_2$ | g |
| | MAI | g |
| | Ag Paste | g |
| | Screens | use |
| | Barrier foils | m$^2$ |
| | Double sided tape | g |
| | Contact Buttons | pair |

| | | |
|---|---|---|
| | Fixed costs (Capex) | €/m$^2$ |
| | Variable Costs | €/m$^2$ |
| | Selling Price | €/W |
| *Financials* | Revenue | € |
| | R&D | % |
| | SG&A | % |
| | Operating margin | % |

*Table A5.1 Parameters for economic evaluation*

# References

[1] M. Liu et al. *Nature*, 2013, 501 , 395-398

[2] W. A. Dunlap-Shohl et al. *ACS Energy Lett.*, 2018, 3 , 270-275

[3] N. J. Jeon et al. *Nature*, 2015, 517 , 476 —480

[4] B. Danekamp et al. *ACS Appl. Mater. Interfaces*, 2018, 10, 36187-36193

[5] D. Perez-del-Rey et al. *J. Phys. Chem. Lett.*, 2018, 9, 1041

[6] C. Wang et al. *Chem. Physics Letters* 2016, 649, 151-155

[7] V. Arivazhagan et al. *Sol. Energy*, 2019, 181, 339 -344

[8] C. Momblona et al*. Energy Environ. Sci*. 2016, 9, 3456-3463

[9] M. J. Bækbo et al. *RSC Adv,*. 2018, 8, 29899

[10] K.B. Lohmann et al. *ACS Energy Lett.*, 2020, 5, 3, 710–717

[11] E. Smecca et al. *J. Mater. Chem. A.* 9, 16456–16469

[12] https://creativecommons.org/licenses/by-nc/3.0/

[13] https://www. alliedmarketresearch. com/company-profiles (last access: 12/05/22)

[14] I. Mathews et al. *Joule*, 2020, 4, Pages 822-839

[15] https://about.bnef.com/blog/solar-10-predictions-for-2022/ (last access: 24/07/22)

[16] https://www.nrel.gov/pv/cell-efficiency.html (last access: 13/07/22)

[17] C. Dong et al. *Adv. Func. Mat.,* 202, 31, 2011242

[18] K.-L. Wang et al. *Chem. Sci.*, 2021, 12, 11936-11954

[19] https://sauletech.com/product/ (last access: 05/04/22)

[20] N.L. Chang et al. *Sol. Energy Mater. Sol. Cells*, 2018, 174, 314-324

[21] https://metsolar.eu/blog/how-much-does-really-bipv-cost/ (last access: 05/04/22)

[22] O. Malinkiewicz, et al. *Nature Photon.*, 2014 8, 128–132 1

[23] J. Li et al. *Joule*, 2020,4, 5, 1035-1053

[24] D. Perez-Del-Rey et al. *J. Phys. Chem. Lett.,* 2018, 9, 1041.

[25] Private Communication with Kenosistec SRL

[26] Y-H. Chiang et al. *ACS Energy Lett.* 2020, 5, 8, 2498–2504

# Ringraziamenti (Acknowledgements)

# PhD thesis defense – Reviewer's report

Please, send before **07 October 2022**, to the Coordinator: Prof. G. Compagnini
(giuseppe.compagnini@unict.it)

PhD candidate: **Salvatore Valastro**
Reviewer: **Fortunato Neri**
Please give your frank opinion on the candidate's scientific work, based on the received thesis draft

|  | Excellent | Good | Fair | Poor |
|---|---|---|---|---|
| Technical quality | X |  |  |  |
| Novelty | X |  |  |  |
| Relevance | X |  |  |  |
| Clarity of presentation | X |  |  |  |
| Length of the thesis | X |  |  |  |

DETAILED COMMENTS ON THE THESIS:

The PhD thesis work of dr Salvatore Valastro deals with the study of Perovskite Solar Cells (PSCs) device architectures, examining specific issues relevant for their large-scale production. In particular, topics like performance durability over the time, up-scaling to large area devices and environmental protection from Pb contamination due to leakage from damaged PSCs are addressed and viable routes have been explorated.

The thesis is very well written with a clear, plain and extensive description of both the overall topic (Introduction) and of the state-of-art solution approaches, reported in chapters from 1 to 4. The economic analysis of up-scalable in-vacuum physical deposition methods for affordable PSCs manufacturing (chap. 5) is also appreciable.

The results on strategies to improve the stability of $CsPbI_3$ formed at low-temperature, to preserve the carbon electrode/PSC interface, the integration of perovskite recycle in Triple-Mesoscopic Carbon-based PSCs and the use of sputtered $TiO_2$ sponge for leaked Pb sequestration are of particular scientific relevance.

On the overall the thesis is well structured and presents very interesting results. Therefore, I repute as excellent the work presented by the candidate dr. Salvatore Valastro and I recommend for him the admission to the final exam.

Based on your opinion, do you believe the candidate is ready to be admitted to the PhD defence ? YES
If not, please provide a suitable delay time (max 6 months) to review the thesis

Messina, 26/9/2022                                                        Fortunato Neri

Reviewer's letterhead paper

# **PhD thesis defense – Reviewer's report**

PhD candidate: Salvatore Valastro

Reviewer: Antonio Abate

Please give your frank opinion on the candidate's scientific work, based on the received thesis draft

|  | **Excellent** | **Good** | **Fair** | **Poor** |
|---|---|---|---|---|
| Technical quality | **X** |  |  |  |
| Novelty | **X** |  |  |  |
| Relevance | **X** |  |  |  |
| Clarity of presentation | **X** |  |  |  |
| Length of the thesis | **X** |  |  |  |

---

DETAILED COMMENTS ON THE THESIS:

In this thesis manuscript, the candidate proposes the topic of inorganic perovskite solar cells. This is undoubtedly one of the most recent and challenging topics of a broad community researching novel photovoltaic materials and, more broadly, optoelectronic material. The topic has been approached from an original angle focusing on stability as the currently considered most pressing target. The quality of the methods is excellent. The authors proposed novel methodologies while demonstrating the ability to reproduce state-of-the-art methods. The results are well described and perfectly integrated into a clear and flowing discussion that makes it enjoyable to read the text.

In short, I can recommend Salvatore Valastro for admission to the PhD defence without hesitation.

I also want to recommend the thesis for outstanding recognition.

---

Based on your opinion, do you believe the candidate is ready to be admitted to the PhD defence? **YES**

If not, please provide a suitable delay time (max 6 months) to review the thesis

Place, date

Berlin 5/10/2022

Signature

# Curriculum Vitae

## Salvatore Valastro

**Date and place of birth:** 02/08/1992,
Catania, Italy

**Nationality:** Italian

**Email address**
salvalastro@gmail.com
salvatore.valastro@imm.cnr.it

**LinkedIn**
https://www.linkedin.com/in/salvatore-valastro-ba06b4196/

## Higher Education

| | |
|---|---|
| 2019-2022 | **PhD candidate**<br>Materials Science and Nanotechnology<br>XXXV Cycle<br>*Università degli Studi di Catania*<br>https://www.unict.it/ |
| 02/02/2020 | **Authorization to practice as Civil-Environmental Engineer (Section A)**<br>*Università degli Studi di Catania*<br>https://www.unict.it/ |
| 23/10/2019 | **Master's degree in Environmental Engineering**<br>Final grade: 110/110 cum laude<br>*Università degli Studi di Catania*<br>https://www.unict.it/<br>Thesis: Realizzazione e caratterizzazione di celle solari di terza generazione costituite da perovskite con controelettrodo in carbonio |

## Professional Experience

| | |
|---|---|
| 14/01/2022 – Current | **Research Fellow**<br>*Consiglio Nazionale delle Ricerche (CNR)- Istituto per la Microelettronica e Microsistemi (IMM)* |
| 14/01/2020-13/01/2022 | **Research Scholarship**<br>*Consiglio Nazionale delle Ricerche (CNR)- Istituto per la Microelettronica e Microsistemi (IMM)* |
| 05/02/2019 – 22/10/2019 | **Internship**<br>*Consiglio Nazionale delle Ricerche (CNR)- Istituto per la Microelettronica e Microsistemi (IMM)* |

# Publications

**A gig-lox TiO$_2$ sponge to prevent lead leakage in Perovskite Solar Cells**
Authors: **Salvatore Valastro**, Emanuele Smecca, Giovanni Mannino, Corrado Bongiorno, Giuseppe Fisicaro, Stefan Goedecker, Valentina Arena, Carlo Spampinato, Ioannis Deretzis, Sandro Dattilo, Andrea Scamporrino, Sabrina Carroccio, Enza Fazio, Fortunato Neri, Francesco Bisconti, Aurora Rizzo, Corrado Spinella, Antonino La Magna, Alessandra Alberti
*Nature Sustainability 2022 (accepted for publication)*

**A low temperature growth of Cu$_2$O thin films as hole transporting material for perovskite solar cells**
Authors: Anna Lucia Pellegrino, Francesca Lo Presti, Emanuele Smecca, **Salvatore Valastro**, Giuseppe Greco, Salvatore Di Franco, Fabrizio Roccaforte, Alessandra Alberti, Graziella Malandrino
*Materials 2022, 15(21), 7790*
https://www.mdpi.com/1996-1944/15/21/7790

**Stabilizing wide band gap triple halide perovskite alloy through organic gelators**
Authors: Vitantonio Valenzano, Emanuele Smecca, **Salvatore Valastro**, Sonia Carallo, Giuseppe Gigli, Silvia Colella, Alessandra Alberti, Aurora Rizzo
*Solar RRL 2022, 202200909*
https://onlinelibrary.wiley.com/doi/10.1002/solr.202200909

**In-situ Degradation Pathway Analyses on Hybrid Perovskites with Mixed Cations and Anions**
Authors: Emanuele Smecca, Vitantonio Valenzano, Ioannis Deretzis, **Salvatore Valastro**, Sonia Corallo, Silvia Colella, Giovanni Mannino, Aurora Rizzo, Antonino La Magna, Alessandra Alberti
*The Journal of Physical Chemistry C 2022, 126, 16825*
https://pubs.acs.org/doi/abs/10.1021/acs.jpcc.2c04330

**Perovskite Solar Cells from the viewpoint of innovation and sustainability**
Authors: Alessandra Alberti[#], Emanuele Smecca[#], **Salvatore Valastro**[#], Ioannis Deretzis , Giovanni Mannino[#], Corrado Bongiorno, Giuseppe Fisicaro, Antonino La Magna
[#] Authors who contributed equally
*Physical Chemistry Chemical Physics 2022, 24, 21549*
https://pubs.rsc.org/en/Content/ArticleLanding/2022/CP/D2CP02891C

**Out-of-Glovebox Integration of Recyclable Europium-Doped CsPbI$_3$ in Triple-Mesoscopic Carbon-Based Solar Cells Exceeding 9% Efficiency**
Authors: **Salvatore Valastro**, Emanuele Smecca, Corrado Bongiorno, Carlo Spampinato, Giovanni Mannino, Simone Biagi, Ioannis Deretzis, Filippo Giannazzo, Ajay Kumar Jena, Tsutomu Miyasaka, Antonino La Magna, Alessandra Alberti
*Solar RRL 2022, 6, 2200267*
https://onlinelibrary.wiley.com/doi/10.1002/solr.202200267

**Black-Yellow Bandgap Trade-off during Thermal Stability Tests in Low-Temperature Eu-doped CsPbI$_3$**
Authors: **Salvatore Valastro**, Giovanni Mannino, Emanuele Smecca, Corrado Bongiorno, Salvatore Sanzaro, Ioannis Deretzis, Antonino La Magna Ajay Kumar Jena, Tsutomu Miyasaka, Alessandra Alberti
*Solar RRL 2022, 6, 2200008*
https://onlinelibrary.wiley.com/doi/10.1002/solr.202200008

**MAPbI$_3$ deposition by LV-PSE on TiO$_2$ for photovoltaic application**
Authors: Emanuele Smecca, Ajay Kumar Jena, Ioannis Deretzis, **Salvatore Valastro**, Salvatore Sanzaro, Giovanni Mannino, Corrado Bongiorno, Antonino La Magna, Tsutomu Miyasaka, Alessandra Alberti
*Frontiers in Electronics 2021, 2, 726171*
https://www.frontiersin.org/articles/10.3389/felec.2021.726171/full

**Two-step MAPbI$_3$ deposition by low-vacuum proximity-space-effusion for high-efficiency inverted semitransparent perovskite solar cells**
Authors: Emanuele Smecca, Vitantonio Valenzano, **Salvatore Valastro**, Ioannis Deretzis, Giovanni Mannino, Graziella Malandrino, Gianluca Accorsi, Silvia Colella, Aurora Rizzo, Antonino La Magna, Andrea Listorti, Alessandra Alberti
*Journal of Materials Chemistry A 2021, 9, 16456*
https://pubs.rsc.org/en/content/articlelanding/2021/ta/d1ta02535j

**Exploring the Structural Competition between the Black and the Yellow Phase of CsPbI$_3$**
Authors: Ioannis Deretzis, Corrado Bongiorno, Giovanni Mannino, Emanuele Smecca, Salvatore Sanzaro, **Salvatore Valastro**, Giuseppe Fisicaro, Antonino La Magna, Alessandra Alberti
*Nanomaterials 2021, 11(5), 1282*
https://www.mdpi.com/2079-4991/11/5/1282

**Optical behaviour of γ-black CsPbI$_3$ phases formed by quenching from 80 °C and 325 °C**
Authors: **Salvatore Valastro**, Giovanni Mannino, Emanuele Smecca, Salvatore Sanzaro, Ioannis Deretzis, Antonino La Magna Ajay Kumar Jena, Tsutomu Miyasaka, Alessandra Alberti
*Journal of Physics: Materials 2021, 4, 034011*
https://iopscience.iop.org/article/10.1088/2515-7639/abfa7a/meta


**CsPbBr$_3$, MAPbBr$_3$, and FAPbBr$_3$ Bromide Perovskite Single Crystals: Interband Critical Points under Dry N$_2$ and Optical Degradation under Humid Air**
Authors: Giovanni Mannino, Ioannis Deretzis, Emanuele Smecca, Filippo Giannazzo, **Salvatore Valastro**, Giuseppe Fisicaro, Antonino La Magna, Davide Ceratti, Alessandra Alberti
*The Journal of Physical Chemistry C 2021, 125, 9, 4938*
https://pubs.acs.org/doi/abs/10.1021/acs.jpcc.0c10144


**Formation of CsPbI$_3$ γ-phase at 80°C by Europium assisted snowplow Effect**
Authors: Alessandra Alberti, Emanuele Smecca, Ioannis Deretzis, Giovanni Mannino, Corrado Bongiorno, **Salvatore Valastro**, Salvatore Sanzaro, Giuseppe Fisicaro, Ajay Kumar Jena, Youhei Numata, Zhanglin Guo, Corrado Spinella, Tsutomu Miyasaka, Antonino La Magna
*Advanced Energy and Sustainability Research 2021, 2, 2100091*
https://onlinelibrary.wiley.com/doi/full/10.1002/aesr.202100091


**Improved Electrical and Structural Stability in HTL-Free Perovskite Solar Cells by Vacuum Curing Treatment**
Authors: **Salvatore Valastro**, Emanuele Smecca, Salvatore Sanzaro, Filippo Giannazzo, Ioannis Deretzis, Antonino La Magna, Youhei Numata, Ajay Kumar Jena, Tsutomu Miyasaka, Antonio Gagliano, Alessandra Alberti
*Energies 2020, 13(15), 3953*
https://www.mdpi.com/1996-1073/13/15/3953


**Full Efficiency Recovery in Hole-Transporting Layer-Free Perovskite Solar Cells With Free-Standing Dry-Carbon Top-Contacts**
Authors: **Salvatore Valastro**, Emanuele Smecca, Salvatore Sanzaro, Ioannis Deretzis, Antonino La Magna, Youhei Numata, Ajay Kumar Jena, Tsutomu Miyasaka, Antonio Gagliano, Alessandra Alberti
*Frontiers in Chemistry 2020, 8:200*
https://www.frontiersin.org/articles/10.3389/fchem.2020.00200/full

# Conferences and workshops

03/10/2022       **Metodo innovativo per il ricoprimento uniforme di superfici con materiali porosi**
(Oral presentation)
*Futura Expo 2022, Brescia, Italy*
Authors: Alessandra Alberti, Salvatore Sanzaro, Emanuele Smecca, Giovanni Mannino, **Salvatore Valastro**

18/05/2022 – 21/05/2022       **Black-Yellow Bandgap Trade-off during Thermal Stability Tests in Low-Temperature Eu-doped $CsPbI_3$** (Oral Presentation and Poster)
*International Conference on Hybrid and Organic Photovoltaics (HOPV), Valencia, Spain*
Authors: **Salvatore Valastro**, Giovanni Mannino, Emanuele Smecca, Corrado Bongiorno, Salvatore Sanzaro, Ioannis Deretzis, Antonino La Magna Ajay Kumar Jena, Tsutomu Miyasaka, Alessandra Alberti

09/05/2022 – 11/05/2022       **$CsPbI_3$ for Perovskite Solar Cells: applications and perspectives**
(Oral Presentation)
*AIV XXV Conference, Napoli, Italy*
Authors: **Salvatore Valastro**, Giovanni Mannino, Emanuele Smecca, Salvatore Sanzaro, Ioannis Deretzis, Carlo Spampinato, Antonino La Magna Ajay Kumar Jena, Tsutomu Miyasaka, Alessandra Alberti

22/11/2021 – 24/11/2021       **Optical behaviour of γ-black $CsPbI_3$ phases formed by quenching from 80 °C and 325 °C**
(Oral presentation)
*3rd Scientific School on Hybrid, Organic and Perovskite Photovoltaics (HOPE-PV 2021)*
Authors: **Salvatore Valastro**, Giovanni Mannino, Emanuele Smecca, Salvatore Sanzaro, Ioannis Deretzis, Antonino La Magna Ajay Kumar Jena, Tsutomu Miyasaka, Alessandra Alberti

| | |
|---|---|
| 10/10/2021 – 12/10/2021 | **Full efficiency recovery in HTL-free Perovskite Solar Cells with free-standing dry-carbon top-contacts** (Oral presentation) *III Moscow Autumn Perovskite Photovoltaics International Conference (MAPPIC-2021)* Authors: **Salvatore Valastro**, Emanuele Smecca, Salvatore Sanzaro, Ioannis Deretzis, Antonino La Magna, Youhei Numata, Ajay Kumar Jena, Tsutomu Miyasaka, Antonio Gagliano, Alessandra Alberti |
| 14/02/2019 | **"Soluzioni energetiche che vengono incontro allo sviluppo verticale delle città"** (Pitch) *Workshop Project "ENISIE Interreg Italia-Malta", at TIM WCAP, Catania, Italy* |